The influence of dislocations on magnetic properties in steel

Magnetisation curve and magnetic Barkhausen effect in relation to deformation and recovery in C-Mn and IF steel

Riny Volkers

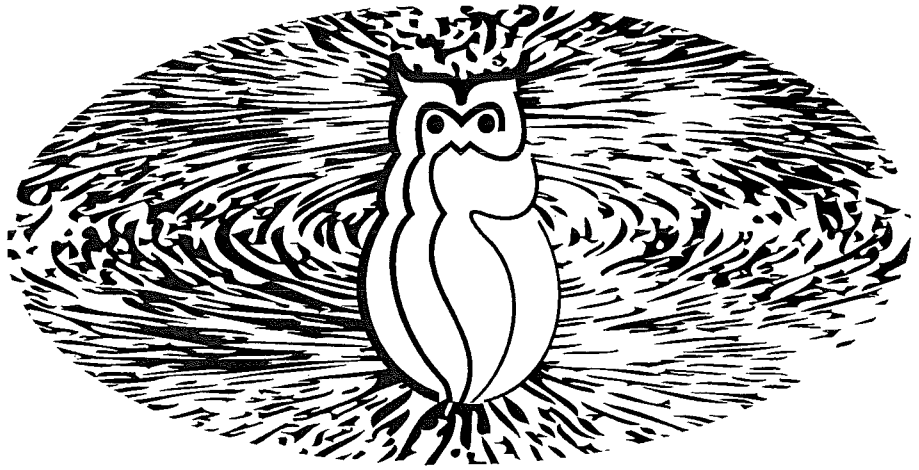

Supervisors: Dr. Ir. J. Sietsma
Dr. L. Zhao

Department: Materials Science and Engineering
January 2008

TU Delft
Delft University of Technology

. . . it must be that there stream off this stone very many seeds or an effluence, which, with its blows, parts asunder all the air which has its place between the stone and the iron. When this space is emptied . . . atoms of the iron start forward and fall into the void, all joined together . . . the ring itself follows . . . with its whole body.

Lucretius is attributed to be the first to give a scientific explanation for, as we now know, magnetic interaction between materials.
On the Nature of Things (De Rerum Natura), 1st century B.C.

Preface

This Masters Thesis is written as part of the Masters programme "Materials Science and Engineering" within the faculty of Mechanical, Maritime and Materials Engineering, Delft University of Technology. The research work leading to this thesis has been performed in the period January 2007 – January 2008, under supervision of Jilt Sietsma and Lie Zhao.

Many people have contributed to this work. In no particular order, I would like to thank:
Jilt Sietsma and Lie Zhao for their supervision and guidance – Erik Vegter of SKF for supporting the MBE experiments, discussing the results and taking place in my graduation committee – Sybrand van der Zwaag and Guido Janssen for taking place in my graduation committee – Thim Zuidwijk for getting me started with the Gleeble – Nico Geerlofs for helping out with 1001 experimental issues – Jan Greving for helping me out with experimental issues at SKF – Martin Siekman from University of Twente for showing me the potential and limitations of the MFM – Gianfranco Durin from Istituto Nazionale di Ricerca Metrologica for commenting on the MBE experimental techniques – Alexis Miroux for discussing Gleeble issues and getting me started with Ali's material – Jeroen Colijn from Corus for realising a quick delivery of IF steel – Jasper Groenewegen for getting me started with LaTeX – Andrzej Wojtas from Stresstech for discussing the MBE equipment – Jan Boomsma for discussing Gleeble issues - David Ferguson from DSI for explaining Gleeble issues – Csilla Buiting for doing everything possible to provide a good working situation – Erik Peekstok for helping out with polishing and etching issues – Michael Janssen for discussing deformation results – Arjen Kamp and Mehdi Lal Poor for providing printing service – Otto Schimmelpenninck van der Oijen for printing the report – Niels van Dijk for explaining the determination of N_d from the data – Roumen Petrov for performing EBSD experiments and analysing and explaining the results.

The image on the front cover shows the owl Simba, part of the logo of "Het Gezelschap Tubalkaïn", the former study association for Materials Science and Engineering and current association for all former students of this department. In this image, Simba acts as a bar magnet, with the surroundings representing ferromagnetic particles that are aligned in the direction of the magnetic field created by this bar magnet.

Abstract

Microstructure control is a key factor in production and use of metals. Many microstructure characterisation techniques exist. Most of them are limited to the sample surface or destructive by nature. Using magnetic properties for microstructure characterisation has the advantages that the bulk of the sample is characterised, while the technique in itself is non-destructive, although sample preparation is required.

To develop a characterisation technique based on magnetic properties, understanding is required of the magnetisation process, leading to these magnetic properties, in relation to the microstructure. Despite extensively published research work, clear relations are not yet achieved, showing the complexity of this process. Therefore, this study aimed at relating the magnetic properties to one microstructure component, being dislocations.

The main purpose of this study was to investigate the potential of two different experimental techniques: Magnetisation curve experiments, using a Vibrating Sample Magnetometer (VSM) and magnetisation process experiments based on the Magnetic Barkhausen Effect (MBE). Both were used to investigate effect of dislocations. For the VSM experiments, it is shown that a compromise is to be made between the obtained detail and the stability of the equipment. The contribution of the dislocation density to the coercivity of ferrite has been determined quantitatively.

For the purpose of microstructure evaluation, MBE experiments provide more detail than magnetisation curve experiments. However, for the purpose of understanding the magnetisation process, an improvement of the MBE experiments is required. This study has yielded a better understanding of the experimental issues, leading to recommendations to establish this improvement and use the full potential MBE has.

Contents

List of Figures

List of Tables

1. Introduction

When working with materials, the microstructure is of crucial importance. It determines most properties of the material. The microstructure can be defined as the lattice type with the total of all defects in the material, where a defect can be any deviation from the perfect lattice. Also, the microstructure can be adjusted by applying treatments such as annealing and deformation. This makes microstructure control a key factor in producing materials with a desired set of properties.

This importance of microstructure control in metals has lead to the development of a huge set of characterisation techniques, each with their own advantages and disadvantages. These techniques themselves also make use of the effect of the microstructure on material properties, which can be of different type than the type of properties that is of interest for applications. Furthermore, these techniques make use of a set of clearly defined and controllable variables. As will be explained in this thesis, magnetic properties are a set of properties that also depend on the microstructure.

As characterisation techniques, the techniques that use the magnetic properties have two significant advantages:

1. Magnetic measurements are bulk measurements. Therefore, the obtained microstructure information accounts for the whole sample used, instead of only the surface, as with some other techniques.

2. Determining magnetic properties in itself is non-destructive. This has as a consequence that the magnetic properties can be determined multiple times, while in between, treatments can be applied.

The main disadvantage of using magnetic properties is the complex relation between these properties and the microstructure. This has as a consequence that it is complicated to reconstruct the microstructure from the magnetic properties.

In this study, an attempt is made to reveal part of this relation. For this purpose, the microstructure is changed using deformation and recovery. With these processes, especially with recovery, only one microstructure parameter is changed, which is the dislocation distribution. This way, the change in

magnetic properties can be clearly related to this single change in the microstructure.

For determining the magnetic properties, two different techniques are explored. These techniques involve the magnetisation curve and the magnetic Barkhausen effect. The details of these magnetic phenomena are explained in chapter 2. Chapter 3 discusses deformation and recovery annealing as processes to change the dislocation structure. This chapter also discusses literature results on the relation between these dislocation structures and the magnetic properties.

The experimental outline for this study is described in chapter 4. This chapter contains a short overview of the experimental techniques used. As a reference for the magnetic experiments, chapter 5 discusses the material characterisation using other techniques and theoretical models.

The results from the Vibrating Sample Magnetometer (VSM) experiments, in which the magnetisation curve properties are determined, are presented and discussed in chapter 6. In relation to this, Barkhausen experiments have been conducted and are presented and discussed in chapter 7. Finally, conclusions are drawn in chapter 8 and recommendations given in chapter 9.

2. Magnetism

Magnetism is a complex phenomenon. It is caused by and affects electric currents. These electric currents can be of any scale, down to the scale of electron spin, as this can also be seen as moving electric charges and thus as an electric current. In order to understand the background of using magnetic properties to evaluate the microstructure, some aspects of magnetism are explained in this chapter, starting with the most important definitions, related to this topic.

2.1 Some definitions

- Magnetic field strength (**H**)

  The magnetic field is a way of interaction between electric charges, provided that they move relative to each other. Static electric charges only interact by electrostatic interactions. A moving electric charge, which forms an electric current, creates a magnetic field around it. The strength and direction of the field depend on the density of electric current, its direction and the shape and dimensions of the conductor through which the current flows. **H** is a vector and has the dimension of A m^{-1}.

- Magnetisation (**M**)

  As will be explained in the next subsection, each atom has a magnetic moment **m**. These atom magnetic moments can be added to get the total magnetic moment of a medium. The magnetisation **M** is then defined as the total magnetic moment per unit of volume V, which is:

$$\mathbf{M} = \sum_i \frac{\mathbf{m}_i}{V} \tag{2.1}$$

  M is a vector and has the same units as **H**, that is A m^{-1}.

- Magnetic induction (**B**)

When a magnetic field is applied to a medium, a magnetic flux $\mathbf{\Phi}$ is induced within this medium. This magnetic flux is commonly represented with lines, where each line represents an arbitrary amount of magnetic flux. This common representation originates from initial assumptions that magnetic flux was a current-like quantity. The magnetic flux density, which is the amount of magnetic flux per unit of cross-sectional area, is called magnetic induction. $\mathbf{B}$ is a vector and has the dimension of Tesla, Weber m^{-2} or kg s^{-1} A^{-1}, which are equivalent.

- Permeability (μ)

  All media respond to a magnetic field by a magnetic induction. This density of this magnetic induction depends on the magnetisation of the medium and the applied magnetic field and is given by:

$$\mathbf{B} = \mu_0 (\mathbf{H} + \mathbf{M}) \tag{2.2}$$

  where μ_0 is the permeability of vacuum and is equal to $4\pi \cdot 10^{-7}$ H m^{-1}. In general, the permeability of a medium is denoted with μ and is defined by:

$$\mathbf{B} = \mu \, \mathbf{H} \tag{2.3}$$

  These permeabilities are related by the relative permeability μ_r, which is defined such that:

$$\mu = \mu_0 \, \mu_r \tag{2.4}$$

  In vacuum, $\mathbf{M}$ is equal to zero and μ_r is therefore equal to one. The definition of the permeability originates from the observation that the magnetic flux tends to concentrate in certain media, leading to a higher flux density $\mathbf{B}$. Similar to electric currents, this concentration of flux current was considered due to these media having lower magnetic resistance, hence a higher magnetic permeability. μ and μ_0 are scalars and have the dimension of Weber A^{-1} m^{-1}, Henry m^{-1} or kg m s^{-1} A^{-2}. μ_r is also a scalar and is dimensionless.

- Susceptibility (χ)

  Combining the various definitions for $\mathbf{B}$, one finds that $\mathbf{M}$ is not independent of $\mathbf{H}$. Actually, as $\mathbf{B}$ is proportional to $\mathbf{H}$, like in equation 2.3, this means a similar proportionality is present between $\mathbf{H}$ and $\mathbf{M}$. This time, the susceptibility χ is the constant of proportionality, defined by:

Table 2.1: Classification of magnetic media by magnetic susceptibility.

Magnetic classification	χ
Diamagnetic	$\sim -10^{-5}$
Paramagnetic Anti-ferromagnetic	$\sim 10^{-5}$–10^{-3}
Ferromagnetic Ferrimagnetic Helimagnetic Superparamagnetic	~ 10–10^{4}

$$\mathbf{M} = \chi\, \mathbf{H} \tag{2.5}$$

From the definition of μ_r, one finds that $\mathbf{M}$ can also be related to $\mathbf{H}$ by:

$$\mathbf{M} = (\mu_r - 1)\ \mathbf{H} \tag{2.6}$$

This leads to the following relation between the permeability and the susceptibility:

$$\chi = \mu_r - 1 \tag{2.7}$$

χ is a scalar and is dimensionless, like μ_r.

- Magnetic materials

  Having defined χ next to μ and μ_r may appear unnecessary and cause confusion, when both are used randomly. However, the definition of χ allows a clear distinction between different media, from a magnetic point of view. χ gives the magnetisation as function of magnetic field, which is the contribution of the medium to the magnetic induction in equation 2.2. For vacuum, this contribution is clearly 0, and so is χ. For other media, χ can vary within specific ranges as shown in table 2.1. The various magnetic classifications, of which the most important are diamagnetic, paramagnetic and ferromagnetic, will be elaborated in section 2.2.

- Magnetic energy (Q_{mag})

  The energy for a magnetic moment $\mathbf{m}$ is defined as

$$Q_{mag} = -\mu_0\, \mathbf{m} \cdot \mathbf{H} \tag{2.8}$$

which is the magnetic energy of a single atom, if **m** is the atom moment. Using equation 2.1, this can be written as

$$Q_{\text{mag}} = -\mu_0 \, \mathbf{M} \, V \cdot \mathbf{H} \tag{2.9}$$

which is valid for a single atom, but also for more atoms together. Using equation 2.6, this results in

$$Q_{\text{mag}} = -\mu_0 \, (\mu_r - 1) \, V \, \mathbf{H}^2 \tag{2.10}$$

which is, with equations 2.3 and 2.7,

$$Q_{\text{mag}} = \left(-\mathbf{H} \cdot \mathbf{B} + \mu_0 \, \mathbf{H}^2\right) \, V \tag{2.11}$$

Since **H**, **B** and **M** are vectors, they have a direction as well as a length. From equations 2.3 and 2.5, **B** and **M** are in the same direction if $\chi > 0$ and in opposite direction as $\chi < 0$. If $\chi > 0$, Q_{mag} decreases when the material enters the magnetic field. Therefore, materials with $\chi > 0$ are attracted by magnetic fields. If $\chi < 0$, Q_{mag} increases when the material enters the magnetic field. Therefore, materials with $\chi < 0$ are repulsed by magnetic fields. **H** and **B** are defined to be in the same direction by $\mu > 0$. If $\mu_r \gg 1$, $\mathbf{B} \gg \mu_0 \mathbf{H}$ by equation 2.3 and equation 2.11 simplifies to

$$Q_{\text{mag},V} = -\mathbf{H} \cdot \mathbf{B} \tag{2.12}$$

where $Q_{\text{mag},V}$ is the magnetic energy per unit of volume and which is a well know equation for the magnetic energy inside ferromagnetic materials. However, the induction inside the material creates a magnetic field outside the material. This magnetic field increases the total energy of the system, such that its behaviour not only depends on the magnetic energy inside the material. The effect of this outer magnetic field will be elaborated further in subsection 2.3.3 on shape anisotropy.

The definitions as used here are from the Sommerfeld (SI) convention. This is the most commonly used convention, although two other conventions are also used in literature. For completeness, these conventions are listed in table 2.2. Note that **I** is an alternative measure for **M** and is in all circumstances equal to

$$\mathbf{I} = \mu_0 \, \mathbf{M} \tag{2.13}$$

Table 2.2: Principal unit systems currently used in magnetism and the corresponding equations for flux density **B** and energy Q_{mag}. Note that the EMU system is very sloppy with dimensions.

		SI	SI	EMU
Quantity		(Sommerfeld)	(Kennelly)	(Gaussian)
Field	**H**	A m^{-1}	A m^{-1}	Oersted ($250/\pi$ A m^{-1})
Induction	**B**	Tesla (T)	T	Gauss (10^{-4} T)
Magnetisation	**M**	A m^{-1}	-	emu/cm^3 (1000 A m^{-1})
Intensity of magnetisation	**I**	-	T	-
Flux	**Φ**	Weber (Wb)	Wb	Maxwell
Field equation		$\mathbf{B} = \mu_0\ (\mathbf{H} + \mathbf{M})$	$\mathbf{B} = \mu_0\ \mathbf{H} + \mathbf{I}$	$\mathbf{B} = \mathbf{H} + 4\pi\ \mathbf{M}$
Energy of moment	-	$Q_{mag} = -\mu_0\ \mathbf{m} \cdot \mathbf{H}$	$Q_{mag} = -\mathbf{m} \cdot \mathbf{H}$	$Q_{mag} = -\mathbf{m} \cdot \mathbf{H}$

2.2 Magnetic moment

Magnetism is caused by moving electric charges. At an atom level, these moving electric charges are either the electron spin or electron orbital motion. The magnetic moment of an atom **m** is the sum of the magnetic moments of the electrons. Most electrons appear as pairs with opposite spin, which yield a zero net spin magnetic moment. Elements with an odd number of electrons per atom however, always have an unpaired electron, causing the atom to have a net spin magnetic moment that is non-zero. Elements with an even number of electrons per atom usually have zero net spin magnetic moment.

The total magnetic moment of a medium is the vector sum of all the atom magnetic moments. An external magnetic field will influence the atomic magnetic moments and thereby the total magnetic moment. Spin magnetic moments are influenced such that they act in favour of the external field. Therefore, they have a positive contribution to χ. Orbital magnetic moments counteract the external field and have therefore a negative contribution to χ.

The magnetic field exerts a force on the electron, causing the orbital velocity of the electron to decrease and with that, the orbital magnetic moment of the electron, with respect to the direction of the magnetic field, decreases as well. Therefore, if the net spin magnetic moment is zero, the total magnetic moment, and thus the magnetisation, becomes negative. This is the

case for *diamagnetic* elements. In elements that have a non-zero net spin magnetic moment, the orbital effect is small compared to the spin effect.

Although in all non-diamagnetic media the magnetic properties are determined by the electron spin, there are large differences in the magnetic behaviour of these media. These differences originate from the coupling of the atom magnetic moments. In many elements this coupling depends on the temperature. At high temperatures, the thermal energy is such that there is no effective coupling. The atom magnetic moments are randomly ordered, in what is called *paramagnetism*. Also, some elements with an even number of electrons per atom are paramagnetic instead of diamagnetic.

Below a critical temperature, called Curie temperature, some materials have their magnetic moments positively coupled (in the same direction). Iron (BCC), nickel, cobalt and some rare earth metals show this behaviour. This coupling behaviour causes the susceptibility to be $10–10^4$. These materials are called *ferromagnetic* and are the most interesting and important class of magnetic metals.

Another magnetic class is the *anti-ferromagnetic class*, where atomic magnetic moments are negatively coupled and cancel out completely. In some materials, for instance magnetite (Fe_3O_4), not all magnetic moments are cancelled out and a net magnetisation is present, which is positive with respect to the magnetic field. These materials form the *ferrimagnetic* class. In the case of magnetite, the trivalent iron ions are negatively coupled, while the divalent iron ions are positively coupled. *Helimagnets* are like ferromagnets, but with a helical periodic deflection of the atomic magnetic moments. Also *superparamagnetic* materials exist, which combine paramagnetic properties with a high permeability.

In everyday use, ferrimagnetic, helimagnetic and superparamagnetic materials are often called ferromagnetic. For metals, ferromagnetic materials are the most interesting and important magnetic class. Within the scope of this survey, only ferromagnetism is discussed.

2.3 Anisotropy

The magnetic coupling in ferromagnetic materials is due to the interaction between atom magnetic moments causing an energy minimum if these moments have parallel alignment. The value of this energy minimum depends on the common orientation of these atomic magnetic moments, causing a directional anisotropy. The orientations for which the energy as function of this orientation is at a minimum are called 'easy directions', as the magnetic moments tend to spontaneously rotate into those orientations. This anisotropy

is an important factor in the origin of magnetic properties of ferromagnetic materials. Magnetic anisotropy is divided into three categories:

1. Crystallographic anisotropy
2. Stress anisotropy
3. Shape anisotropy

These three origins of anisotropy determine the directions of the easy axes and the energy differences between these easy directions and other directions.

2.3.1 Crystallographic anisotropy

In crystalline materials, the anisotropy energy is related to the orientation of the magnetic moments with respect to the crystal lattice. This anisotropy energy is related to the spin-orbit coupling in the electrons involved. As described above, the spins are strongly coupled by magnetic interaction. In the crystal lattice, the orbits are also strongly coupled in the forming of the lattice. Therefore, the spin-orbit coupling, which is relatively weak and can be overcome by strong magnetic fields, creates a magnetocrystalline anisotropy. In 1929, the Russian physicist Akulov showed that the magnetocrystalline anisotropy energy involved can be expressed as a series expansion of the cosines of the angles between the atom magnetic moment and the crystal axes [1]. For a cubic crystal in which the magnetic moments make angles α_1, α_2 and α_3 with the crystal axes [100], [010] and [001], the anisotropy energy per unit volume Q_{An} is:

$$\begin{aligned} Q_{An} = & K_0 + K_1 \left(\cos^2\alpha_1 \cos^2\alpha_2 + \cos^2\alpha_2 \cos^2\alpha_3 + \cos^2\alpha_3 \cos^2\alpha_1\right) \\ & + K_2 \left(\cos^2\alpha_1 \cos^2\alpha_2 \cos^2\alpha_3\right) + \ldots \end{aligned} \tag{2.14}$$

in which K_0, K_1, $K_2 \ldots$ are anisotropy constants. In the most common ferromagnetic materials, all terms involving K_2 and further have a very small contribution to Q_{An} and can be neglected. Also, the value of K_0 is not important for this topic as it does not change the differences between different crystallographic directions. Table 2.3 shows the energies for the three main crystallographic directions in a cubic lattice.

For ferromagnetic materials with cubic lattice symmetry, the $< 100 >$ directions are the easy directions if K_1 is positive, which is the case for BCC iron. If K_1 is negative, the $< 111 >$ directions are the easy directions, which

Table 2.3: Magnetocrystalline anisotropy energies for three directions in a cubic lattice [1]

$[uvw]$	[100]	[110]	[111]
Q_{An}	K_0	$K_0 + \frac{K_1}{4}$	$K_0 + \frac{K_1}{3}$

is the case for nickel. Logically, the $< 111 >$ directions are the hardest axes in BCC iron, while $< 100 >$ are the hardest axes in nickel.

For cobalt, which has a HCP structure, the anisotropy energy can be determined in a similar manner. In cobalt, the [0001] direction is the easy axis and $[10\bar{1}0]$ the hardest.

2.3.2 Stress anisotropy

The atom magnetic moment is caused by the spin of the unpaired outer electron of the atom. Within a domain, all these moments are aligned and these electron spins have the same orientation. Because this concerns the outer electrons, the interaction between the atoms in the crystal is influenced by this anisotropy in electron states. This causes the inter-atomic distance to vary between the different directions and with that it creates a length difference between the directions parallel to the magnetic moments and perpendicular to it. This relative length difference is known as magnetostriction, which can be either negative or positive and its absolute value is usually of the order of 10^{-5} in saturation [2, 3]. Magnetostriction consists of two parts. At decreasing temperature, the atomic magnetic moments will order at passing the Curie temperature (see section 2.2 and subsection 2.5.3). This causes a spontaneous magnetostriction, which is shown in figure 2.1 as the change from state a) to state b). When the material is magnetised, the magnetic moments in the different domains become aligned, causing a forced magnetostriction, shown as the change from state b) to state c) in figure 2.1.

Due to this magnetostriction, an extra anisotropy term arises when stresses are present. With a positive magnetostriction, a positive strain (tensile) occurs in the direction of the magnetisation. This elongation will be easier if a tensile stress in that direction is present and harder in case of a compressive stress in that direction. As a consequence, the easy axis will then be in the direction of tensile stress.

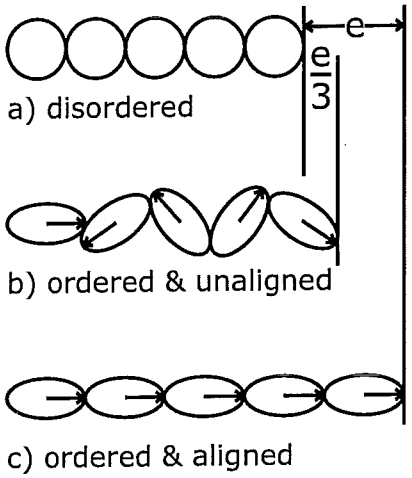

Figure 2.1: The length difference between magnetically aligned (whole material), ordered (within domains) and disordered systems, known as magnetostriction. Figure after [2].

2.3.3 Shape anisotropy

When a material is magnetically induced and not magnetically closed, it creates a magnetic field both inside and outside the material. The magnetic field outside the material is the one that can be measured and used to determine the magnetisation. With ferromagnetic materials, this field can be strong, involving a high magnetic energy, which influences the magnetisation of the material. The amount of energy involved, and thus the demagnetising effect created, depend on the shape of the material with respect to the direction of magnetisation. Furthermore, in heterogeneous materials, there can be a shape anisotropy effect due to the shape and direction of the phases, in particular when elongated particles are present. Because of this magnetic energy, the magnetic moments tend to be in the longest direction.

The demagnetising effect can be described as a demagnetising field $\mathbf{H}_d$ which changes the true field $\mathbf{H}$ according to:

$$\mathbf{H} = \mathbf{H}_a - \mathbf{H}_d = \mathbf{H}_a - N_d\,\mathbf{M} \tag{2.15}$$

where $\mathbf{H}_a$ is the applied field, N_d the demagnetising factor and $\mathbf{M}$ the magnetisation. The demagnetising factor depends on the shape and permeability of the sample, as shown in figure 2.2 for cylinders and ellipsoids.

In a cylindrical, magnetised material, the magnetic field lines are not parallel within the material. They diverge towards the ends, see figure 2.3.

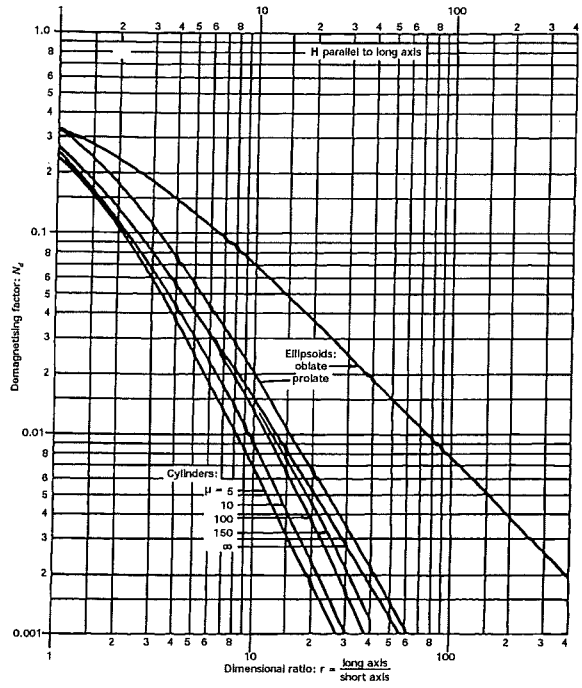

Figure 2.2: Demagnetising factors for cylinders and ellipsoids as function of aspect ratio for various permeabilities. Figure taken from [1].

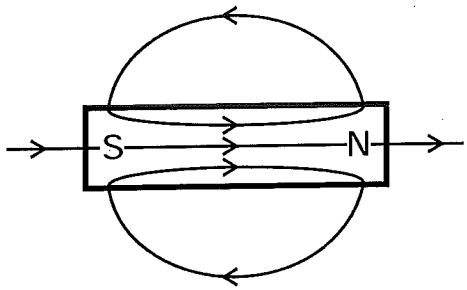

Figure 2.3: Magnetic flux lines through a cylindrical sample. Note the diverging lines near the ends. This diverging effect is stronger for higher permeabilities, leading to a relatively higher free pole density in the centre, when compared to the ends. Figure after [1].

Therefore, the material will not be uniformly magnetised, unless it is fully saturated. However, the density of field lines leaving the material is much higher at the two ends of the cylinder than at the sides and is lowest halfway the cylinder axis. This means that the density of 'free poles' (poles that are not compensated by other poles of opposite sign in the immediate neighbourhood [1]) is higher at the ends than at the sides as well. However, there are still free poles present at the sides. These free poles cause the demagnetising effect. Note that a closed magnet has no free poles and therefore no demagnetising effect. Kobayashi and Ishikawa [4] have numerically calculated that for cylinders the free pole density at the sides is higher for lower aspect ratios and higher permeabilities, when compared to the free pole density at the ends. Therefore, the demagnetising factor is higher as well. For an infinitely long cylinder, the free pole density at the sides is 0, giving $N_d = 0$. Ellipsoids have a higher free pole density at the sides, due to their shape, and have a higher demagnetisation factor than cylinders. In ellipsoids, the permeability has no effect as the shape enables uniform magnetisation, see figure 2.4.

2.4 Domains

Due to the positive coupling of atom magnetic moments in ferromagnets, one would expect ferromagnetic materials to spontaneously magnetise. However, macroscopically, this is not the case. The magnetic energy involved is such that it is more favourable to lower the magnetisation by forming a poly-domain structure, in which the (spontaneous) magnetisation is in different directions in different domains, see figure 2.5. By this, the net magnetisation of the

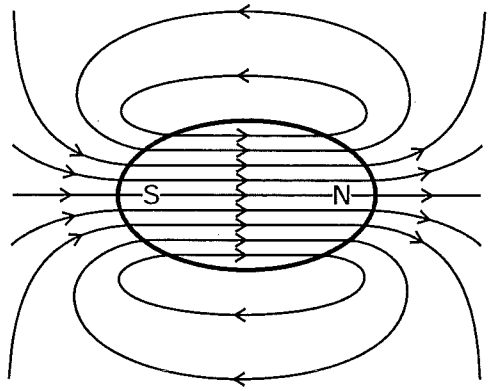

Figure 2.4: Magnetic flux lines through a ellipsoid sample. Note that there are no diverging lines within the material. However, the elliptic shape leads to a relatively higher free pole density in the centre, when compared to the ends (near effective north and south poles). Figure after [1].

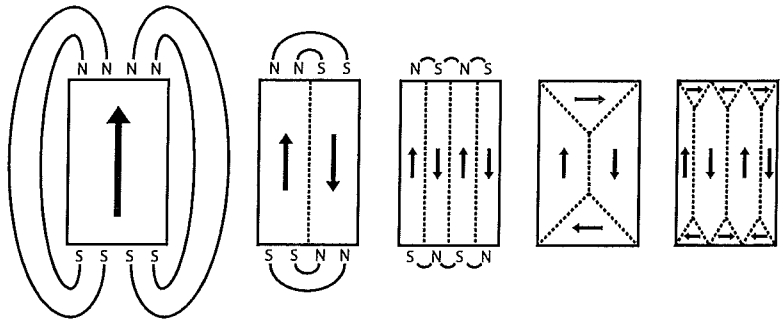

Figure 2.5: The presence of domains to reduce the external magnetic field caused by the magnetic moments in the material. Figure after [5].

whole material is reduced and so is the corresponding magnetic energy. Also closure domains can arise. These are, usually small, domains in which the magnetisation is not necessarily in the easy direction, but that reduce the magnetic field outside the material.

2.4.1 Domain walls

On the border between two domains a conflict arises. On the one hand, the anisotropy causes the magnetic moment for all atoms to be energetically favourable in an easy direction. This anisotropy energy per unit of domain

wall area is given by

$$Q_{A,\text{an}} = \frac{|K_1|\ \delta}{C_\alpha\ a} \tag{2.16}$$

where K_1 is the same anisotropy constant as in equation 2.14, δ the domain wall thickness, C_α a positive constant based on equation 2.14 and a the lattice parameter. Therefore, one would expect the domain wall to be as thin as possible.

On the other hand, the energy involved in the coupling of atom magnetic moments prevents large angles between neighbouring atom magnetic moments, while the total angle between the magnetisations in two domains typically is 90° or 180°. This coupling energy per unit of domain wall area is given by

$$Q_{A,\text{co}} = \frac{\mu_0\ \xi\ \mathbf{m}^2\ \phi^2}{\delta\ a} \tag{2.17}$$

with ϕ the total angle between the magnetisations of the neighbouring domains and ξ a magnetic coupling exchange parameter. For this, one would expect an infinitely large region between two domains, where the directions of the magnetic moments of the neighbouring atoms change with infinitely small steps $\frac{\phi}{\delta}$.

The actual wall thickness is a compromise between these two considerations, minimising the total energy obtained by summing equations 2.16 and 2.17, resulting in:

$$\delta = \sqrt{\frac{\mu_0\ \xi\ \mathbf{m}^2\ \phi^2\ C_\alpha}{|K_1|}} \tag{2.18}$$

Therefore, the wall thickness depends on the material, the type of wall and the angle between the two domains. Typically, the wall thickness is several tens to hundreds of nanometres.

Two different types of domain walls exist. The main type is a Bloch wall, see figure 2.6. In a Bloch wall the atom magnetic moments in the wall point outside the plane that is formed by the magnetic moments in the two domains. Also Néel walls exist, see figure 2.7. In a Néel wall the atom magnetic moments in the wall are within the plane, formed by the magnetic moments in the two domains. Generally, in Néel walls, the demagnetising field caused by the wall is larger than in Bloch walls, causing the latter to be more common. However, in thin films, the Bloch wall causes a magnetic field outside the film, which costs additional energy, causing Néel walls to be present in thin films.

When magnetising a ferromagnetic material in a certain direction, the component of the magnetisation vector in this direction increases. Princi-

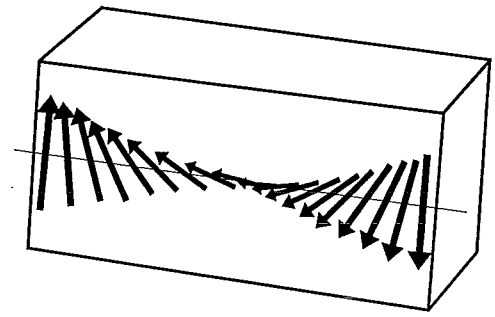

Figure 2.6: Schematic view of the Bloch wall. Note that in a three dimensional view, the arrows in the wall point outside the plane formed by the magnetic moments of the domains (outer arrows). Figure after [5]

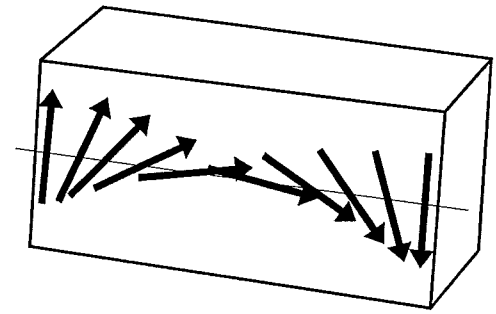

Figure 2.7: Schematic view of the Néel wall. Note that in a three dimensional view, the arrows in the wall are within the plane formed by the magnetic moments of the domains (outer arrows).

pally, this can happen in various ways. Previously, it was thought that atom magnetic moments within a domain rotated to increase this component of the magnetisation. Since approximately 1930 domain wall motion is regarded as the main mechanism. Domain rotation may occur in four particular situations:

- Forced saturation, when atom magnetic moments are forced from their easy axes to the field direction.
- Domain nucleation and annihilation.
- Nanocrystalline materials, in which the domains cannot become significantly larger than the domain wall thickness. In such materials, the crystallite magnetic moments may be free to rotate. In that case, the material behaves superparamagnetic instead of ferromagnetic.
- Very strong pinning of domain walls, such that the energy required to pass the pinning site is larger than the energy required to rotate the magnetic moments within the domain. Domain wall pinning will be elaborated in the next subsection.

2.4.2 Domain wall pinning

Domain wall motion can be seen just as it is named. Domain walls move in such a way that domains with a magnetisation in a favourable direction grow at the cost of domains with a less favourable direction of their magnetisation. No actual translation of atoms takes place, but atom magnetic moments in the wall change their direction, such that the wall is moving.

As discussed in subsection 2.4.1, the existence of domain walls means an increased energy level, due to its imperfections in atom magnetic moments relative to each other and to the easy directions. This defect energy can be compared with energy involved in structural defects, like impurity atoms, dislocations, and grain boundaries. Impurities are often found at dislocations, due to the lower total energy of combined defects, compared with the energy of the two defects independently added together. Similarly, the combined energy for a structural defect and a domain wall is lower when the defect is inside the wall.

This can be explained by looking back to equations 2.16 and 2.17. The total energy of the domain wall is the sum of the anisotropy energy and coupling energy involved. The anisotropy energy is strongly related to the crystal lattice. The presence of a structural defect means that the crystal lattice is locally distorted. This distortion causes the anisotropy energy as a function of magnetic moment orientation to change. This change could

involve only energy differences, but might also locally involve a new easy axis. Due to this change, the presence of a structural defect will cause an energy minimum in the anisotropy term, equation 2.16, when the domain wall passes the defect. Also, the coupling of the atom magnetic moments will be affected by the structural defect, causing a minimum in the coupling term, equation 2.17, as well.

When a domain wall is moving through the material, it will pass many defects. On passing a defect, the total energy obtains a minimum when the defect is in the wall. Moving the wall further requires an increase of internal energy, which means a force, which can be accomplished by increasing the applied magnetic field. This extra applied magnetic field is needed to prevent the domain wall from being stuck at defects, which is known as domain wall pinning.

On applying a magnetic field, the magnetic energy per 180° domain wall area involved in domain wall motion over a distance s is

$$Q_{A,\mathrm{mag}} = -2\ \mu_0\ \mathbf{M}_\mathrm{s} \cdot \mathbf{H}\ s \tag{2.19}$$

with $\mathbf{M}_\mathrm{s}$ being the saturation magnetisation. This equation can be derived from equation 2.9 by noticing that the magnetisation within a domain is equal to $\mathbf{M}_\mathrm{s}$, that the change of magnetisation is twice this value (from negative to positive) and the volume is given by the domain wall area and the displacement s. This means that the stress $\boldsymbol{\sigma}$ on the domain wall caused by magnetic field $\mathbf{H}$ in direction $\mathbf{i}$ is

$$\boldsymbol{\sigma} = 2\ \mu_0\ (\mathbf{M}_\mathrm{s} \cdot \mathbf{H})\ \mathbf{i} \tag{2.20}$$

To calculate the pinning stress in relation to this magnetic stress, two models are used. One model assumes a rigid wall that remains planar and to which the pinning sites act as potential wells. The second model assumes a flexible wall that bows around pinning sites.

According to the rigid wall model, the displacement will be such that $\frac{\partial Q}{\partial s}$ is zero, where Q is obtained by adding equation 2.19 to the potential energy due to pinning sites, which is a function of position and thus of displacement. In this model the density of pinning sites and the energy gained by combining specific pinning sites and domain walls are the main parameters determining $Q(s)$ and thus χ. From this a force results that is required to move the domain wall past the pinning point, which is defined as the pinning strength.

The pinning nature of lattice defects is caused by two effects. Firstly, the defect locally causes the easy axis to be different than in the lattice, or to be fully absent, depending on the type of lattice defect. This effect lowers

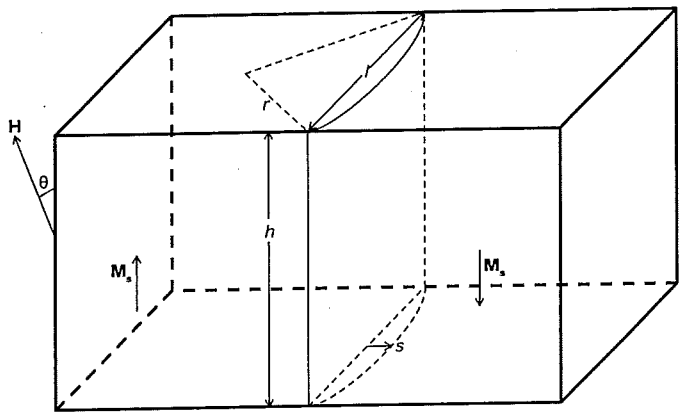

Figure 2.8: A schematic drawing of the flexible domain wall model. Figure after [2].

the wall energy in equation 2.14 and thus in equation 2.16, when the wall interacts with the defect, due to locally smaller angles α.

Secondly, the defect causes lattice strains. Because of the magnetostriction, these strains cause the anisotropy constants K_i in the same wall energy equations to be affected. For 180° walls, these strains only interact with domain wall movement if they are present within the domain wall. For 90° walls however, these strains also interact with domain wall movement if they are present in the two domains that are divided by this domain wall. This difference causes 180° walls to have higher mobility than 90° walls in the presence of lattice strains [6].

According to the flexible wall model, the wall passes a pinning site if the stress in equation 2.20 is larger than the maximum stress due to surface tension, which is for simple cylindrical bending:

$$\sigma = \frac{Q_{DW}}{A\, r}\,\mathbf{i} \tag{2.21}$$

where Q_{DW} is the domain wall energy and r the minimum radius of curvature, as in figure 2.8. In this model the density of potential pinning sites is important in determining r. The type of pinning site is less important in this model, as long as it is strong enough to pin the domain wall. In both models μ depends linearly on the total area of domain wall. Domain walls generally have both a rigid and a flexible character, as shown in figure 2.9. For each particular pinning event, the pinning strength and domain wall energy will determine whether the domain wall moves in a rigid or flexible manner.

In principle, domain wall pinning is caused by any defect in the material. Therefore, studying domain wall pinning can give information on the

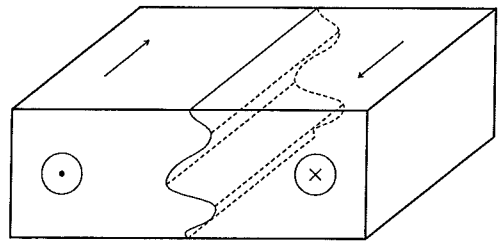

Figure 2.9: A schematic drawing of a domain wall having both a flexible and a rigid character, depending from where it is viewed. Figure after [2].

microstructure of the material, like the presence of:

- Impurities
- Dislocations
- Grain boundaries
- Second phase grains or particles and voids

2.5 Magnetic properties

2.5.1 Magnetisation curve

Above, permeability, or its equivalent susceptibility, is defined such that it seems that the magnetic induction is proportional to the applied magnetic field. However, especially for ferromagnetic materials, this is not the case. The extra force required to magnetise the material, caused by the demagnetising field, domain wall pinning and magnetic anisotropy, causes the material to magnetise in a non-linear way. When going through a magnetisation cycle, the magnetisation shows a hysteresis loop, see figure 2.10.

The magnetisation curve of a ferromagnetic material is characterised by a number of parameters:

- Saturation magnetisation ($\mathbf{M}_s$)

  The saturation magnetisation is the maximum magnetisation that can be achieved by applying a magnetic field that is in principle infinitely large. When this situation occurs, the material has only one domain in which all the magnetic moments direct to the applied field, which is not necessarily in the easy direction of the material. This parameter is taken to be structure independent, and can be computed directly

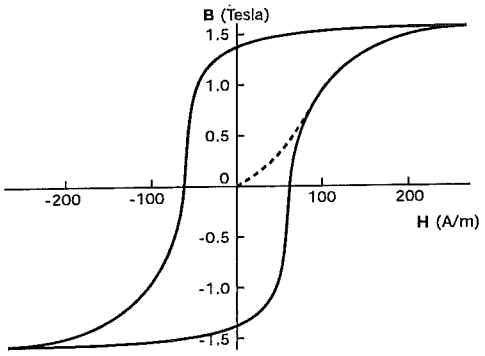

Figure 2.10: A typical magnetisation curve of a ferromagnetic material, showing a hysteresis loop. The dashed line is the initial magnetisation. Figure after [2]

from the saturation magnetisations $\mathbf{M}_{s,i}$ of the ferromagnetic phases and their volume fractions f_i in the material:

$$\mathbf{M}_s = \sum_i \mathbf{M}_{s,i}\, f_i \tag{2.22}$$

At infinitely large applied field, $\mathbf{M}_s$ is constant below the Curie temperature, although at finite applied field, $\mathbf{M}_s$ decreases with increasing temperature due to thermally activated precession of the atom magnetic moments.

- Coercivity ($\mathbf{H}_c$)

  The coercivity, or coercive force, is the applied field needed to reduce the magnetic induction to zero after it has been forced up to saturation. This is the half-width of the magnetisation curve at the line $\mathbf{B} = 0$. Because of the large value for χ in ferromagnetic materials, this half-width can also be described by $\mathbf{M} = 0$, which gives a better description of the actual magnetic state of the material. $\mathbf{H}_c$ is an effect of the interaction between domain wall motion and structural defects and therefore depends on the presence of these structural defects. Also, anisotropy and temperature affect this interaction and $\mathbf{H}_c$.

- Permeability: initial (μ_{in}) and maximum (μ_{max})

  As shown in figure 2.10, ferromagnetic materials do not magnetise in a linear way, that is, they do not show a constant value for their permeability during magnetisation. Permeability is therefore hard to use

as a single parameter value to characterise a ferromagnetic material. However, permeability values can give information on the structure of materials and therefore, values at specific points during magnetisation have been defined. These are the initial permeability (μ_{in}), which is the permeability value at the start of the magnetisation curve of a demagnetised material, and the maximum permeability (μ_{max}), which is the maximum value of the permeability during the hysteresis curve. μ_{in} is experimentally found to be approximately inversely proportional to $\mathbf{H}_c$ [5]. Instead of μ, also χ can be used as characterising parameter.

- Remanence ($\mathbf{B}_r$)

  The remanence is the remaining magnetic induction of the material when the applied field is reduced to zero after the material has been induced to saturation magnetisation. It is a structure sensitive parameter as it depends on the resistance of the material to spontaneous demagnetisation. Instead of $\mathbf{B}_r$, also $\mathbf{M}_r$ can be used.

- Hysteresis loss (W_{hys})

  The interaction between domain walls and structural defects can be considered an internal friction, resisting changes in the magnetisation. This internal friction causes an energy loss when the magnetisation is changed. When repeatedly changing the magnetisation, a magnetic hysteresis loop is performed. In this hysteresis loop, the energy loss is proportional to the area within the magnetisation curve, which relates to the magnetic energy being proportional to $\mathbf{B} \cdot \mathbf{H}$. With this friction and thus the shape of the magnetisation curve being dependent on structure and stresses in the material, the hysteresis loss depends on these as well.

These magnetisation curve parameters, especially the coercivity, are among the most commonly used parameters to characterise the magnetic properties of materials in relation to the microstructure.

2.5.2 Barkhausen effect

In 1919, Barkhausen discovered the effect that is now known as the magnetic Barkhausen effect (MBE) [7]. MBE is the effect of discontinuous changes in the magnetic induction, which cause the magnetisation curve to consist of a number of discrete jumps instead of a smooth curve, see figure 2.11.

The main cause of MBE is the discontinuous domain-wall motion, caused by domain wall pinning. As soon as a domain wall passes a pinning site it is free to move towards the next pinning site, where it will be pinned again.

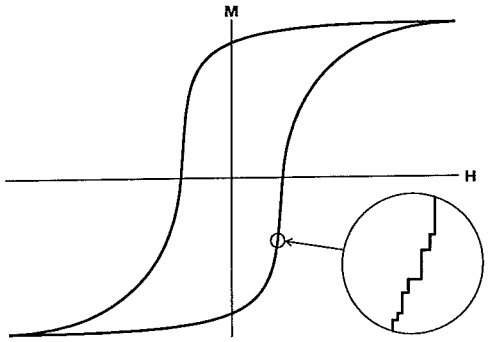

Figure 2.11: The enlarged part of the magnetisation curve shows the distinct magnetisation steps, known as the Barkhausen effect. Figure after [2].

From this, it is clear that MBE is very sensitive to the density and type of pinning sites and therefore to the structure and stresses in the material. MBE is also caused by domain nucleation, which occurs at strong pinning points, like grain boundaries and non-magnetic inclusions, as the presence of these defects lowers the initial domain wall energy [2, 8].

To determine MBE, voltage pulses that arise in a coil pressed on the material surface are measured. Each voltage pulse represents a step-wise change in magnetisation $\Delta\mathbf{M}$ and the height of the pulse S depends on the nature of this change:

$$S \propto \frac{|\Delta\mathbf{M}|}{t} \tag{2.23}$$

with t the duration of the step. With respect to domain wall motion, this pulse size can be written as:

$$S \propto |\mathbf{M}_s|\ |\mathbf{v}_{DW}|\ A \tag{2.24}$$

where A is the domain wall area and $\mathbf{v}_{DW}$ the domain wall velocity. The distance covered by this domain wall motion determines the length of the pulse.

In the literature, this method is referred to with different names and abbreviations, like Barkhausen Effect (BE), Electromagnetic Barkhausen Effect (EBE) and Barkhausen Jumps (BJ). Within this text, only the most common name will be used, which is Magnetic Barkhausen Effect (MBE).

In subsection 2.3.2, magnetostriction was introduced. This magnetostriction combines with MBE to give another phenomenon: the acoustic Barkhausen effect (ABE). When the local magnetisation changes over an angle other than 180°, strain changes occur. Because of the sudden local magnetisation changes involved in MBE, these strain changes are also sudden and cause

acoustic waves within the material. These acoustic waves can be detected at the surface and are known as ABE. Therefore, ABE has the same origins as MBE, but due to its need for magnetostriction, it only occurs with non-180° domain walls. The two names that are used in the literature to refer to this technique are Magneto-Acoustic Emission (MAE) and Acoustic Barkhausen Effect (ABE). Within this text, only ABE will be used.

There are important differences in using MBE or ABE. The two main differences are:

- MBE measurements only investigate magnetisation changes in the surface layer of the material. The changes in magnetisation cause eddy currents, which screen the changes in the bulk from the surface. The thickness of this layer depends on the material and the pulse frequency. Different numbers that are given for the thickness of this layer in steel are 20 μm [3], 100 μm [9], 300 μm [10] and 500 μm [11]. ABE is not influenced by eddy currents.

- Domain walls are divided into 180° walls and non-180° walls (often 90° walls.) As mentioned above, nucleation of domains with only 180° walls or movements of these walls therefore give no ABE signal. The change in magnetisation is larger for 180° wall nucleation and motion than for non-180° walls. Also, as noted in subsection 2.4.2 on domain wall pinning, 180° walls have higher mobility than 90° walls. This causes nucleation of domains with 180° walls or movements of these walls to be dominant in MBE.

2.5.3 Curie temperature

In contrast to the magnetic properties described previously, the Curie temperature (T_C) is almost independent of structural defects and stresses. The Curie temperature has been defined as the temperature below which the material is ferromagnetic and above which the material is paramagnetic. In the ferromagnetic range, the atom magnetic moments are positively coupled, while in the paramagnetic range, they are not coupled. Below T_C the coupling is stronger than the thermal precession, although the thermal precession still affects the net coupling. This causes the technical saturation magnetisation, the state where only thermal precession causes the atom magnetic moments to deflect from the direction of the magnetic field, to be temperature dependent, see figure 2.12.

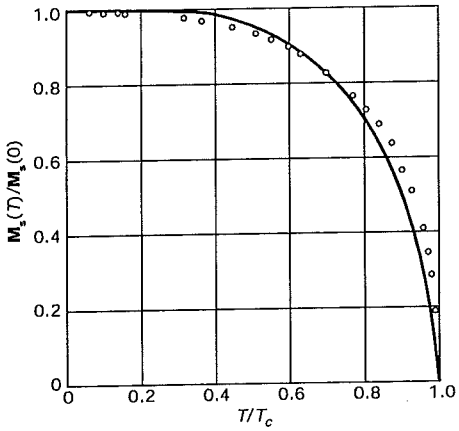

Figure 2.12: The temperature dependence of the technical saturation magnetisation, both by model (solid line) as experimental (open circles) [2].

3. Dislocations

Magnetic properties are influenced by the presence of defects in the material. Anything that makes the material different from a perfect single crystal is a defect. These defects range from 0D defects like substitutional atoms to 3D defects like precipitates. Dislocations are the most common form of 1D defects. In other words, dislocations are present as line defects. A dislocation is characterised by its Burgers vector, which is the direction and the size of the lattice distortion, see figure 3.1. Two distinct dislocation types can be distinguished, known as edge and screw dislocations. In an edge dislocation, the Burgers vector is normal to the line of the dislocation, see figure 3.2. In a screw dislocation the Burgers vector is parallel to the line of the dislocation, see figure 3.3. Mixed dislocations exist as well, consisting of edge and screw parts.

Similar to many phenomena, dislocation presence is commonly given as a density, which describes the 'length of dislocation line' per unit volume. As the dimension of this 'length of dislocation line' is length, the dimension of dislocation density is length/volume or 1/area. Typical dislocation densities in metals are 10^{10}–10^{16} m^{-2}.

3.1 Plastic deformation

Changes in dislocation density can be caused by several processes. The most important process to increase dislocation density is plastic deformation, also known as yielding. To facilitate the permanent character of plastic deformation, the atom structure is rearranged. Within grains, dislocation creation and motion are the most important contributors to this rearrangement. As different grains have different orientations, this leads to different deformations in different grains. Therefore, grain boundary structures will change as well.

Based on these processes, plastic deformation can be split in several regions:

1. Before macroscopic yielding takes place, some plastic deformation occurs locally. As a material is never completely uniform, stresses concen-

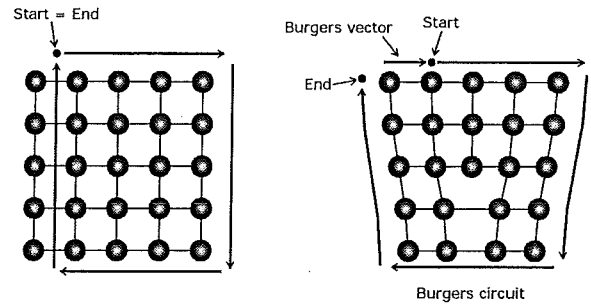

Figure 3.1: Determination of the Burgers vector by a Burgers circuit. The left lattice contains no dislocation, so there is no Burgers vector. The right lattice contains a dislocation with a Burgers vector as shown in the image.

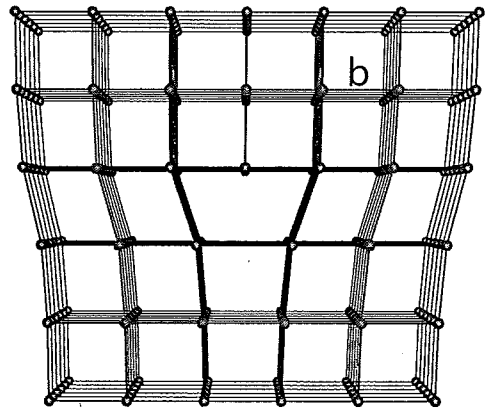

Figure 3.2: 3D visualisation of an edge dislocation. The line of the dislocation is perpendicular to the Burgers vector **b**.

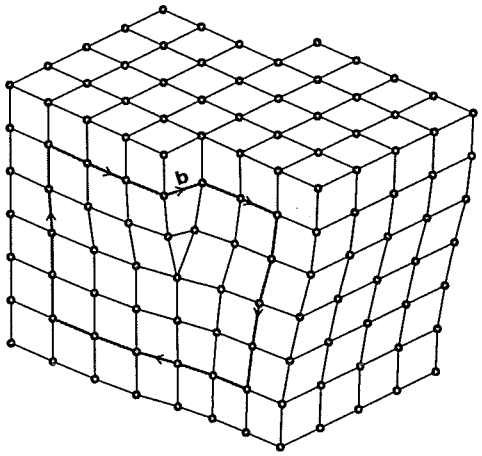

Figure 3.3: 3D visualisation of a screw dislocation. The line of the dislocation is parallel with the Burgers vector **b**. Figure after [12]

trate at locations like scratches or grain boundaries. Due to these stress concentrations, locally, the stress intensity can pass the yield strength, even though the macroscopic stress is still below this point. This way, local plastic deformation can occur in the macroscopic elastic region.

2. In ferritic steel, initial macroscopic plastic deformation takes place as Lüders yielding. This phenomenon can be observed as a yielding band moving through the material and is thus a clearly non-uniform deformation process.

3. When strain is increased further, uniform plastic deformation starts to occur. Initially, this uniform deformation is mainly facilitated by an increase of the dislocation density. Dislocation density can increase by several orders of magnitude within the range mentioned previously. As yield stress increases with dislocation density, this region of plastic deformation is characterised by the work hardening effect.

4. When strain and dislocation density keep increasing, the dislocation distribution starts to become non-uniform. A cell structure is created, with high dislocation density in the cell boundaries and relatively low dislocation density within the cells. Sometimes a stage in between uniform dislocation distribution and cell structure, having regions with dense dislocation tangles surrounding areas with relatively low dislocation density, is distinguished as well.

3.2 Recovery

For decreasing the dislocation density, two different processes most commonly take place in the material, being recrystallisation and recovery. For both processes, the temperature is raised, which increases atomic mobility. Dislocations are thermodynamically unstable, such that a driving force exists to annihilate them. In deformed material, with the dislocation density in the upper part of the given range, this driving force is strong, causing the dislocation density to decrease, depending on the diffusion rate. When the dislocation density is lower, this driving force becomes weaker and the process of decreasing the dislocation density becomes slower. Also, for dislocations to annihilate during recovery, it is required that two dislocations of opposite sign meet. The probability of this happening increases with increasing dislocation density.

Despite the similarity of decreasing ρ_D, recrystallisation and recovery are two distinct processes. During recrystallisation, new grains are formed to replace the existing grains. This will significantly decrease the dislocation density, but also change the grain structure. During recovery, redistribution of dislocations and a decreasing density are the only processes that occur significantly.

Deformation, recovery and recrystallisation are all of great importance in metals processing and monitoring changes using magnetic properties can be very useful for each of them. Of these, the recovery process is the best one to start with as in this case no changes other than the dislocation structure occur, which means that it will give the most clear relation between the dislocation structure and magnetic properties. Therefore, this report will focus on recovery as the main process for changing the dislocation structure.

For the material used, recovery kinetics have been determined by Ali Smith [13], by fitting stress relaxation results to a model by Verdier, Brechet and Guyot [14]. From this model, the relaxation of the internal stress due to dislocations can be written as:

$$\frac{d\sigma_D}{dt} = -\frac{64\sigma_D^2}{9F_T^3\, C_D^2\, E}\, \nu_D\, \exp\left(-\frac{Q_0}{k_B\, T}\right)\, \sinh\left(\frac{\sigma_D\, V_a}{k_B\, T}\right) \qquad (3.1)$$

where the right-hand term consists of three parts. The first factor consists of the stress due to the dislocations σ_D, the Taylor factor F_T (which is 2 for BCC metals [15]), the constant C_D, which is of the order of 0.3 [16], Young's modulus E and the Debye frequency ν_D. This factor takes the driving force and meeting probability into account. The exponential factor describes the relaxation as a classic activation energy situation, where Q_0 is the activation energy for recovery, k_B Boltzmann's constant and T temperature. This factor

takes the atom mobility into account. The sinh factor takes the mean-free-path of the dislocation motion into account. This depends on the dislocation stress σ_D and the activation volume for recovery, which can be written as:

$$V_a = b^2 \, l_a \tag{3.2}$$

where b is the length of the Burgers vector and l_a is an activation length, approximately equal to the spacing of the rate-controlling obstacles to dislocation glide, such as the spacing of jogs or the spacing between solute atoms [17].

The dislocation stress σ_D is a measure of the dislocation density ρ_D. It relates to ρ_D by:

$$\sigma_D = F_T \, C_D \, G \, b \, \sqrt{\rho_D} \tag{3.3}$$

where G is the shear modulus.

3.3 Literature results on dislocations and magnetic properties

Like any other defect, dislocations will interact with domain walls and therefore influence magnetisation processes and magnetic properties. However, the lattice distortion caused by the dislocation, the Burgers vector, is very small compared to the domain wall thickness. The size of the Burgers vector is typically of the order of one atom diameter, while domain walls are commonly hundreds to thousands of atoms wide. Therefore, the effect of a single dislocation on the magnetisation processes will be small.

On the other hand, the dislocation density is high creating large stress fields, and the dislocation density can vary by several orders of magnitude. As mentioned previously, the dislocation density in metals typically varies in the range 10^{10}–10^{16} m^{-2}. Furthermore, dislocations interact with each other forming dense dislocation tangles and cell structures, where the domain walls face much stronger barriers than at single dislocations. As a result of this, magnetic properties are affected by both dislocation density and structure.

3.3.1 Magnetisation curve

The description of magnetic properties is usually done in two ways: the magnetisation curve and Barkhausen effects, where the latter are more directly related to the magnetisation process. For both information sources, usually one or a few parameters are selected to relate to changes in microstructure, in this case specifically on dislocations.

From the magnetisation curve, the coercivity is the most popular parameter as it is easy to determine experimentally and the theoretical estimation is relatively straightforward, as the total magnetisation is zero. This means that the local demagnetisation fields are small compared to the applied field, which is equal to the coercivity $\mathbf{H}_c$.

The magnetic parameters arise from interaction between domain wall movement and lattice defects. These interactions can be described as forces caused by these defects acting on the domain walls. Using Träuble's analysis [18], a relation between the dislocation density and the coercivity can be derived.

The total force $\mathbf{F}$ by lattice defects, acting on a domain wall can be described as:

$$\mathbf{F} = \sum_j m_j \, \mathbf{f}_j \, (z - z_0) \tag{3.4}$$

where m_j is the number of defects of type j, causing a force $\mathbf{f}_j$ on the domain wall, which depends on the position of the defect z relative to the centre of the domain wall z_0. For the analysis, m_j and $\mathbf{f}_j$ are taken as randomly distributed variables.

For a rigid domain wall to overcome this force, a magnetic force must be present that is larger than this force caused by lattice defects. At the onset of domain wall motion, these forces will be equal in magnitude and in opposite direction. The magnetic force on a domain wall is similar to equation 2.20:

$$\mathbf{F} = 2A \, \mu_0 \, (\mathbf{H} \cdot \mathbf{M}_s) \, \mathbf{i} \tag{3.5}$$

where A is the area of the domain wall, $\mathbf{H}$ the magnetic field with direction $\mathbf{i}$ and $\mathbf{M}_s$ the spontaneous magnetisation, which is the saturation magnetisation in an easy axis. To determine the coercivity from equations 3.4 and 3.5, the assumption is made that at the coercive field, the force due to this field:

$$\langle |\mathbf{F}_{max}| \rangle = 2A \, \mu_0 \, (\mathbf{H}_c \cdot \mathbf{M}_s) \, \mathbf{i} \tag{3.6}$$

is equal to the maximum force acting on a domain wall, averaged over all the domain walls. For simplicity, a single crystal is assumed, such that $\mathbf{M}_s$ is constant. Statistically, the expected average maximum value for $\mathbf{F}$ based on equation 3.5 is:

$$\langle |\mathbf{F}_{max}| \rangle = \sqrt{2 \ln \nu} \left\{ \sqrt{\left[\sum_j \langle m_j \rangle M^2 (\mathbf{f}_j) \right]} + \sqrt{\left[\sum_j \langle m_j \rangle \sigma_d (\mathbf{f}_j) \right]} \right\} \tag{3.7}$$

which consists of the following elements:

ν The number of statistically independent events of interaction between the domain wall and the defects. If the minimum distance for two defects to cause two statistically independent events is equal to the domain wall width, then ν is equal to the total distance of the domain wall movement, divided by the domain wall width.

$\langle m \rangle$ The mean number of interactions between the domain wall and lattice defects.

$M(\mathbf{f}_j)$ The mean value of the interaction functions $\mathbf{f}_j$, determined by:

$$M(\mathbf{f}_j) = \frac{\int \mathbf{f}_j(z)\ \mathrm{d}z}{\delta_\mathrm{f}} \tag{3.8}$$

where δ_f is the range of $\mathbf{f}_j$ in the direction perpendicular to the domain wall, which is typically close to the domain wall thickness.

$\sigma_\mathrm{d}(\mathbf{f}_j)$ The standard deviation of the interaction functions $\mathbf{f}_j$, determined by:

$$\sigma_\mathrm{d}(\mathbf{f}_j) = M\left(\mathbf{f}_j^2\right) - M^2(\mathbf{f}_j) \tag{3.9}$$

Because $\mathbf{f}_j$ is taken as a randomly distributed value, $M(\mathbf{f})$ vanishes for large numbers of interactions. In this case, equation 3.7 simplifies to:

$$\langle |\mathbf{F}_\mathrm{max}| \rangle = \sqrt{2 \ln \nu \left[\sum_j \langle m_j \rangle M\left(\mathbf{f}_j^2\right)\right]} \tag{3.10}$$

Combining equations 3.6 and 3.10, one obtains:

$$\mathbf{H}_\mathrm{c} = \frac{\sqrt{\ln \nu \left[\sum_j \langle m_j \rangle M\left(\mathbf{f}_j^2\right)\right]}}{\sqrt{2}\, A\, \mu_0\, \mathbf{M}_\mathrm{s}\, \cos\theta} \tag{3.11}$$

where θ is the angle between the applied magnetic field and the spontaneous magnetisation.

In equation 3.11, the only term that is related to the density of lattice defects is $\langle m_j \rangle$, which was defined as the number of defects of type j, causing a force $\mathbf{f}_j$ on the domain wall. Assuming this interaction is only between the domain wall and defects that are located within the volume V of this wall, then $\langle m_j \rangle$ can be written as:

$$\langle m_j \rangle = V\ \rho_j \tag{3.12}$$

where ρ_j is the volume density of the lattice defects of type j.

For j being dislocations, ρ_j is not equal to the dislocation density, because only dislocations that run parallel to the domain wall affect its motion. Furthermore, dislocations do not generally form straight lines. However, these considerations do not change the relation:

$$\rho_j \propto \rho_D \tag{3.13}$$

where ρ_D is the dislocation density, and thus:

$$\mathbf{H}_c = \gamma_0 + \gamma_D \sqrt{\rho_D} \tag{3.14}$$

with γ_0 depending on other lattice defects and both γ_0 and γ_D depending on effects that were not taken into account, such as temperature and magnetostriction. Within this analysis, some assumptions and approximations are used, such that the relation between dislocation density and coercivity is not exact. However, the determination of 3.14 appears reasonably valid for randomly distributed dislocations. As randomly distributed dislocations are relatively weak pinning points, it seems reasonable to assume rigid domain wall motion.

Equation 3.14 shows that theoretically, the coercivity is proportional to the square root of the dislocation density. Experimental work has shown that the dislocation distribution influences $\mathbf{H}_c$ as well [19–21]. When forming a cell structure, the dislocations appear to make $\mathbf{H}_c$ increase more than if they are present in a homogeneous distribution.

Initial permeability is typically reversely proportional to the coercivity and thus decreases with increasing dislocation density. Also maximum permeability and the more complete permeability as function of applied field decrease with increasing dislocation density [22, 23].

If remanence mainly depends on domain nucleation, it may decrease with increasing dislocation density as the dislocations, or at least regions with entangled dislocations, act as domain nucleation sites [23].

3.3.2 Barkhausen effects

From the above, it is expected that the Barkhausen effects are affected by changes in dislocation structures as well and this has indeed been observed. Referring to the four regions of deformation mentioned previously, most research on the relation between Barkhausen effects and changes in dislocation structures has been performed by applying deformation into the 3rd and 4th region (uniform deformation and cell structure forming).

In region 1, the macroscopically elastic region, micro yielding does occur, especially at larger elastic strains. MBE signals may change due to this micro yielding, but this has only been observed when measuring during applying tensile stress [23]. In region 2, with Lüders yielding, deformation is not homogeneous and therefore, using this region for this purpose is avoided.

In the 3rd and 4th region, the dislocation structure changes significantly and homogeneously in a macroscopic view. MBE results are clearly affected by these changes in the dislocation density, but the details of this are less clear. There seems to be a subtle relation between small defects like dislocations and MBE activity. In general, it is assumed that a larger number of defects will increase MBE activity as there will be more sudden domain wall movements [24–26]. However, if these defects act as strong pinning points, they will prevent the domain walls from moving at all and thus decrease MBE activity. On the other hand, if the defects are too weak, they will not act as pinning points or domain nucleation points, but dampen the domain wall motion and thus slow down the sudden changes, resulting in lower MBE voltage signals and thus a lower MBE activity [24, 25].

For the relatively isolated dislocations, it is yet unclear whether they are large enough defects to act as pinning points and thus whether an increasing density will increase or decrease MBE activity. It is to be noted that this is also affected by the various MBE analysis methods used.

In the initial stage of the 3rd deformation region, both increasing and decreasing MBE activities have been observed. This can well be caused by differences in the original state of the material used. However, the way in which this initial state corresponds to the observed MBE results depends on the detailed relation between dislocations in various configurations and moving domain walls. The same inconsistency is observed in the initial part of fatigue testing.

Relating to these inconsistent results, different explanations regarding the pinning strength of isolated dislocations and tangled dislocations are possible. Isolated dislocations could have sufficient pinning strength to act as pinning points, which means their presence would increase MBE activity [25]. Alternatively, isolated dislocations could have insufficient pinning strength to act as pinning points, but act as domain wall speed dampeners, which means their presence would decrease MBE activity [24].

If the initial dislocation density is low and increases with initial plastic deformation or fatigue testing, this would lead to increasing MBE activity in the first case, due to the higher density of pinning points. However, it would cause decreasing MBE activity in the second case, due to the higher density of dampening points.

If the initial dislocation density is high and decreases with initial plastic

deformation or fatigue testing, the situation would be the opposite. If the initial dislocation is high and would form dislocation tangles or cell structures with initial plastic deformation or fatigue testing, this would lead to decreasing MBE activity in the first case. This is caused by multiple dislocations acting as single pinning points by means of these tangles or cells, leading to a decreased pinning point density, while these pinning points would also become stronger. However, in the second case, the damping point density would decrease and the pinning point density increase, leading to increased MBE activity.

A third situation could be that the change from dampener to pinning point is very subtle, such that isolated dislocations act as dampeners, but will act as pinning points as soon as there is some interaction between dislocations, before the dense dislocation tangles or cell structures are created.

An extra complication is that after plastic deformation, residual micro stresses are present. For tensile deformation, these stresses are in tension for the hard (dislocation-rich) parts and in compression for the soft (dislocation-lean) parts [27]. Due to magnetostriction, which is positive in low alloy steels, the anisotropy changes. The crystallographic easy direction that is close to the direction of tensile stress will become easier than the one perpendicular to that. On changing the applied field, this favours the formation of 90° domain walls in areas that have tensile stresses perpendicular to the applied field or compressive stresses parallel to the applied field. This affects magnetic properties and should therefore be taken into account [25, 27, 28].

Since sudden domain wall movements are larger through dislocation-lean parts than in dislocation-rich parts, due to the low density of pinning points, the residual stresses in these areas have the largest effect on the Barkhausen results. If these residual stresses are such that they favour the formation of 90° domain walls on changing the applied field, this will decrease the MBE intensity, while it will increase ABE intensity. MBE intensity is decreased, because the movement of a 90° domain wall will yield less change in magnetisation as the movement of a 180° domain wall would, up to a factor two. The ABE intensity increases, because movement of a 90° wall creates acoustic noise, where movement of a 180° wall does not.

4. Experimental overview

From the literature results on dislocations and magnetic properties, some relations appear to be present. These form a good start to develop magnetic experiments in which these relations will be confirmed or rejected. This chapter discusses the experimental part of this study. Data analysis and results will be discussed in the next chapters.

Two steel types have been used for this study, being a low-alloy carbon-manganese (C-Mn) steel and an interstitial-free (IF) steel. The C-Mn steel was the same as used by Ali Smith for his Ph.D. work [13]. The IF steel was obtained from Corus. Both were received as hot rolled plate and cylindrical samples were machined with the axis parallel to the rolling direction. For the C-Mn steel, the samples had 12 mm length and 10 mm diameter and for the IF steel, the samples had 10 mm length and 12 mm diameter.

4.1 Gleeble experiments

Thermo-mechanical treatments have been applied using a Gleeble 1500 thermo-mechanical simulator. These treatments consist of a maximum of three stages:

1. Annealing
2. Deformation
3. Stress relaxation

The annealing stage was different for the two materials. The C-Mn steel was first heated with 20°C s^{-1} to 1100°C and kept there for 3 min to fully austenitise. It was then cooled down by thermal radiation to 679°C and kept there for 10 min to gain a ferrite-pearlite structure. Next, it was cooled down to 400°C and stabilised for 5 min. This annealing stage is shown in figure 4.1.

The IF steel was first heated with 20°C s^{-1} to 1000°C and kept there for 3 min to fully austenitise. At this temperature the niobium based precipitates are expected to dissolve, while the titanium based precipitates are not. It was

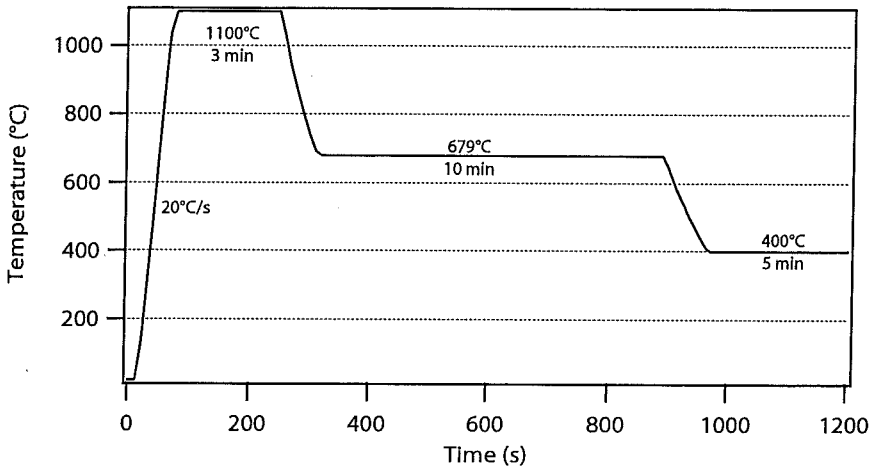

Figure 4.1: Annealing stage for C-Mn steel.

then cooled down to 400°C and stabilised for 10 min. This annealing stage is shown in figure 4.2.

The deformation stage was the same for both materials. The total programmed deformation was 0.20, unless specified otherwise. The deformation speed was 0.10 s^{-1}. The deformation was performed directly after the annealing stage at a stabilised temperature of 400°C. The stress-relaxation stage is only used for the IF steel samples. At the stress relaxation stage, the temperature was kept at a constant level of 400°C. The C-Mn samples were annealed in a box furnace, also at 400°C, unless specified otherwise.

At the end of the experiment, the sample was quenched with water.

The plastic deformation in the sample is not necessarily the same as the programmed deformation. The average strain in the centre of the sample is determined by measuring the diameter before (d_0) and after (d_1) deformation. The strain ϵ is computed by:

$$\epsilon = 2 \ln \left(\frac{d_1}{d_0} \right) \tag{4.1}$$

4.2 Optical microscopy and hardness

Using optical microscopy, micrographs have been made from both materials. The C-Mn steel samples were prepared by polishing down to a 1 μm diamond finish and etching with 2% nital. The IF steel samples were prepared similarly, but etched with 4% picral, with a bit of nital added.

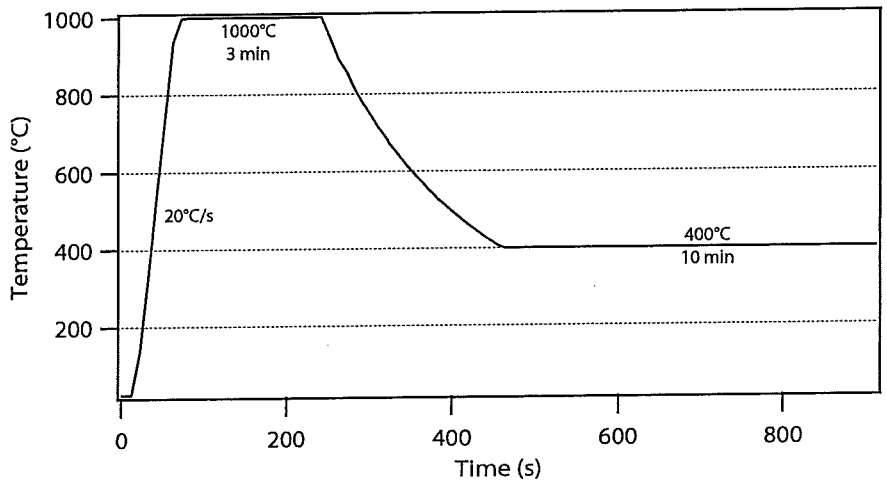

Figure 4.2: Annealing stage for IF steel.

Hardness tests have been performed using a Buehler Omnimet Vickers hardness tester. For macrohardness tests, a load of 500 g was used and for microhardness tests, a load of 25 g was used.

4.3 Electron backscatter diffraction

On two samples, electron backscatter diffraction (EBSD) experiments have been conducted at Ghent University, Ghent, Belgium. For this purpose, the samples have been polished similarly as described in section 4.2, followed by electrolytic polishing. The electrolytic polishing step was conducted on a sample surface of 1 cm^2 with A2 Struers electrolyte, a tension of 40 V and a flow rate of 12 for 10 s.

The EBSD data was acquired on a NOVA 600 Dual beam FEG-SEM with a Nordlis EBSD detector. The data was acquired with the Oxford HKL Channel 5 software package, service pack 9. The FEG-SEM was operating with an accelerating voltage of 20 kV, a beam current of 2.4 mA and a working distance of 7 mm. The sample surface was scanned with a step size of 1.5 μm in a square grid. 8x8 binning was used to reduce the noise. The data was analysed with TSL Orientation Imaging Microscopy version 4.6.

4.4 Magnetic Force Microscope

To visualise the magnetic domain structure, a Digital Instruments D3100 magnetic force microscope (MFM) has been used at the University of Twente, Enschede. In an MFM, a magnetic tip is held close to the surface of the sample, such that the magnetic field caused by the local material magnetisation acts a force on the tip. The tip is placed on a cantilever, such that this force leads to a deflection, which can be recorded. With this tip, the surface can be scanned. Changes in deflection mark changes in local magnetisation, which define the domain structure. However, this method is only one-dimensional, while the actual magnetisation is three-dimensional. This means information about the local magnetisation is lost and the domain structure can not be completely reconstructed from the MFM results.

The resolution of the MFM image depends on the tip size and the distance from the tip to the surface. The minimum distance is mainly determined by:

- Surface finish and cleanliness. Variations in the distance between the tip and the surface influence the deflection, as the magnetic field caused by the local material magnetisation is stronger when closer to the surface. These variations must be small compared to the average distance between the tip and the surface.
- Magnetic softness of the sample material. As the MFM tip is magnetised, it produces a magnetic field, which acts on the sample surface. The magnetic field that acts on the sample surface is larger if the distance between the tip and the surface is smaller. If this field is too large, it can change the domain structure while scanning, by moving domain walls past the pinning points they were pinned at before scanning.

4.5 Vibrating Sample Magnetometer

The magnetisation curves have been determined using a Lake Shore 7307 Vibrating Sample Magnetometer (VSM). The VSM data was collected and exported by the IDEAS-VSM 3.4.0 software package. For the VSM experiments, cylindrical samples with length 3 mm and diameter 1 mm were used. These were made by wire cutting to avoid surface deformation. Unless specified otherwise, all samples have been made with the sample axis in the rolling direction of the material. The magnetic properties were determined along the axis of the samples. Figure 4.3 shows a schematic view of the VSM set-up. The sample is placed on a flat sample holder using double-sided tape to enable a correct orientation with respect to the applied magnetic field and

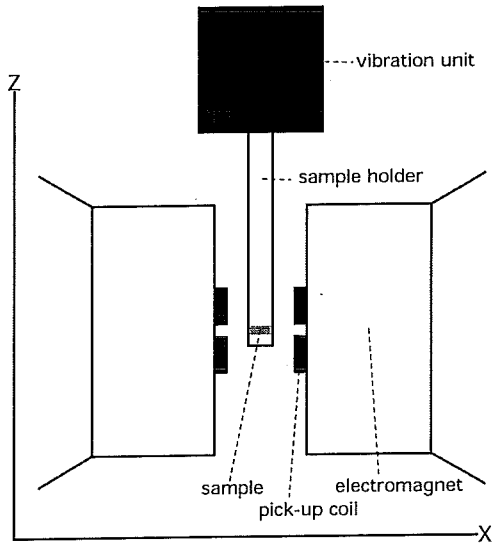

Figure 4.3: Schematic draw of the Lakeshore VSM equipment. The sample is magnetised in the X-direction and vibrated in the Z-direction. The sample is positioned in the centre of the four pick-up coils.

the pick-up coils, which are in the X-direction. The sample vibrates in the Z-direction, with amplitude 0.7 mm and frequency 82 Hz. This vibration causes a changing magnetic field outside the sample, which induces an electric current in the pick-up coils that is recorded by the computer. The electric signal is proportional to the speed of the sample and the magnetic flux within the sample.

The output data can be generated in both SI and EMU unit systems. For the SI option, the applied field is given in Tesla. This value is converted to the field in A m^{-1} by equation 2.2. The magnetic moment is given in A m^2, which is converted to the magnetisation in A m^{-1} by dividing it by the volume of the sample.

As will be shown in chapter 6, the obtained data suffers from significant scatter. This scatter consists of two contributions:

1. Consistency and accuracy of the equipment.

2. Consistency and reproducibility in sample preparation and experimental set-up.

Experimentally, it is found that the second contribution does not increase the scatter caused by the first contribution.

Table 4.1: Step size used for VSM programme 1, shown for the increasing field. For the decreasing field, the ranges and step sizes are the same.

Field range (mT)	Step size (mT)
-1000 – -100	30
-100 – -20	4
-20 – -2	1
-2 – 4	0.1
4 – 20	1
20 – 100	4
100 – 1000	30

The magnetisation curves were created using a stepwise magnetisation. Two different magnetisation programmes were used. In VSM programme 1, around the coercive region, the steps were taken small to obtain detailed information on the coercivity and the remanence. Near saturation, large steps were taken to save time. Table 4.1 shows the step size as function of applied field for VSM programme 1. At the maximum field used of 1 T, saturation was achieved. Performing one full magnetisation cycle takes approximately 75 min.

As table 4.1 shows, the applied field programme is not symmetrical. This relates to a shift in the magnetisation curves, which causes them to be not perfectly centred around the **M**-axis. On average, the centre of the magnetisation curves is at +1 mT. The small-step range is chosen to be 3 mT around this average centre. Afterwards, the hysteresis loops are centred around the **M**-axis by shifting them along the **H**-axis.

In VSM programme 2, around the coercive region, the steps were taken larger than in programme 1, to decrease scatter caused by instability of the VSM equipment. Again, near saturation, large steps were taken to save time. Table 4.2 shows the step size as function of applied field for VSM programme 2. At the maximum field used of 1 T, saturation was achieved. Performing one full magnetisation cycle takes approximately 40 min.

4.6 Magnetic Barkhausen Effect

The Magnetic Barkhausen Effect (MBE) has been determined using a Stresstech Rollscan 300 unit, see figure 4.4. The data was collected and exported by the MicroScan 600 V.4.3 software package. The experiments were performed at SKF, Nieuwegein. For the MBE experiments, the magnetising frequency used was 20 Hz. The sampling frequency was 2.5 MHz, which is the maximum

Table 4.2: Step size used for VSM programme 2, shown for the increasing field. For the decreasing field, the ranges and step sizes are the same.

Field range (mT)	Step size (mT)
-1000 – -200	40
-200 – -100	10
-100 – 100	5
100 – 200	10
200 – 1000	40

sampling frequency supported by the equipment. The maximum voltage on the magnetising coils was 10 V.

Figure 4.5 shows a schematic drawing of the MBE sensor used. Three important spots on the sensor are marked. At the sides of the sensor, the two magnetising elements, forming the two poles of the electromagnet, are present. These elements are approximately 8 mm apart. In the centre, a ferrite part is present that leads to the pick-up coil. When applying an experiment, all three parts are placed on the sample surface.

The magnetic field created by the electromagnet is not only related to the electric current through the magnetising coil. It also depends on the material to which the field is applied. There is no sensor present to measure the applied field. Therefore, the applied field is unknown. Due to the positioning of the electromagnet poles, the applied field is not uniform through the sample. Also, a sensor to measure the magnetisation is not present, so the magnetisation is also unknown.

The pick-up sensor is placed on top of the sample surface. It is therefore sensitive to changes in the magnetic field perpendicular to the sample surface. These changes are caused by the magnetisation in this perpendicular direction. Therefore, the observed MBE relates to a component of the magnetisation that is perpendicular to the applied field.

The obtained data was analysed using the Matlab 2007b software package. With data analysis, characterising parameters were extracted from the data. Also, a digital filter has been applied. The details of this analysis are discussed in chapter 7.

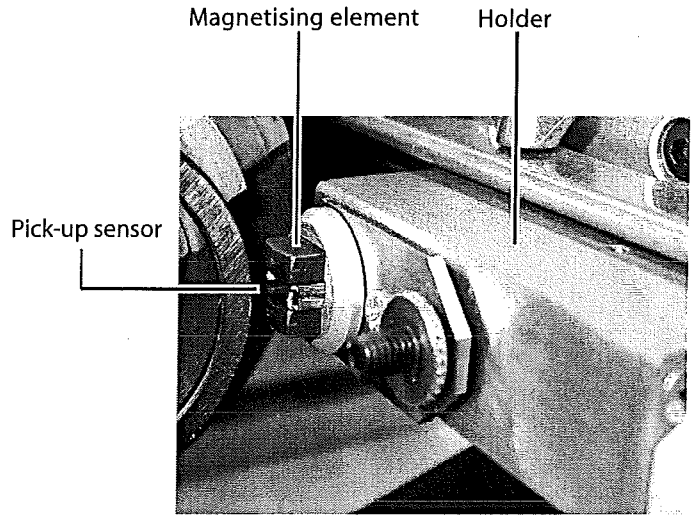

Figure 4.4: The MBE sensor from the Stresstech Rollscan 300 unit. The electromagnet creating the changing magnetic field is incorporated in the holder. The magnetic field is applied to the sample by the magnetising elements at both sides of the pick-up sensor. Photograph from SKF.

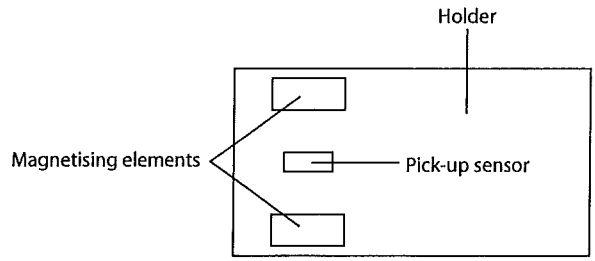

Figure 4.5: Schematic drawing of the MBE sensor used, showing the positioning of the magnetising elements and the pick-up sensor.

5. Material

Chapters 6 and 7 discuss the results from the magnetic experiments. This chapter discusses experimental results that serve as reference. This chapter mainly focusses on the processes used to change the dislocation structure. Also, the microstructure and magnetic domain structure are briefly discussed.

Table 5.1 lists the compositions of the two steel types used for this study. The experimental results are discussed separately for these two steel types.

5.1 C-Mn steel

5.1.1 Microstructure

Figure 5.1 shows the microstructure of the C-Mn steel after annealing (step one in section 4.1). It can be seen that a banded structure of ferrite and pearlite is present. This banded structure has its origin in manganese segregation during hot rolling. This segregation is still present after the annealing step.

The average pearlite colony size is approximately 12 μm. The average ferrite grain size is approximately 35 μm. Deformation is applied in the rolling direction, which is in the length direction of the bands. The magnetisation curves are also applied in this direction.

Table 5.1: Chemical composition of the two steel types used for this study. Contents are given in weight percent.

Type	C (%)	Mn (%)	P (%)	S (%)	Si (%)
C-Mn	0.19	1.46			0.445
IF	0.0019	0.127	0.031	0.008	0.007
	Nb (%)	Ti (%)	Al (%)	N (ppm)	
C-Mn			0.033		
IF	0.024	0.021	0.025	27	

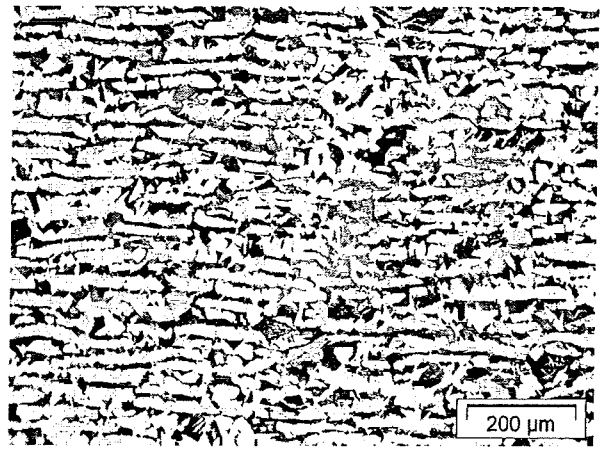

Figure 5.1: Micrograph of C-Mn steel after annealing. Surface was etched with nital.

5.1.2 Deformation and relaxation

Figure 5.2 shows a typical stress-strain curve for the application of a strain of 0.20 at 400°C in the C-Mn steel. This curve does not appear to be a regular stress-strain curve for the deformation of ferritic steel. This is caused by limited stiffness of the Gleeble interior. For the C-Mn steel samples, a programmed strain of 0.20 resulted in an average plastic strain of 0.15 in the centre of the sample.

Figure 5.3 shows a stress-relaxation curve for the C-Mn steel. Using these stress-relaxation curves obtained by Ali Smith [13], the dislocation density as function of annealing time has been modelled with equations 3.1 and 3.3, making:

$$\frac{d\sqrt{\rho_D}}{dt} = -\frac{64Gb\rho_D}{9F_T^2C_DE}\,\nu_D \exp\left(-\frac{Q_0}{k_BT}\right)\sinh\left(\frac{\sqrt{\rho_D}V_aF_TC_DGb}{k_BT}\right) \qquad (5.1)$$

Since equation 5.1 is a differential equation, an initial dislocation density is required as starting point. A way of obtaining an initial dislocation density is assuming a dislocation density of 0 m^{-2} at the onset of yielding and using equation 3.3 for the work hardening stress [13], where the work hardening stress is the difference between the yield stress and the deformation stress. However, from figure 5.2, the yield stress can not be clearly identified. Based on hardness measurements, two other approaches have been used to estimate the dislocation density after deformation.

1. Samples have been deformed to several strains and hardness profiles

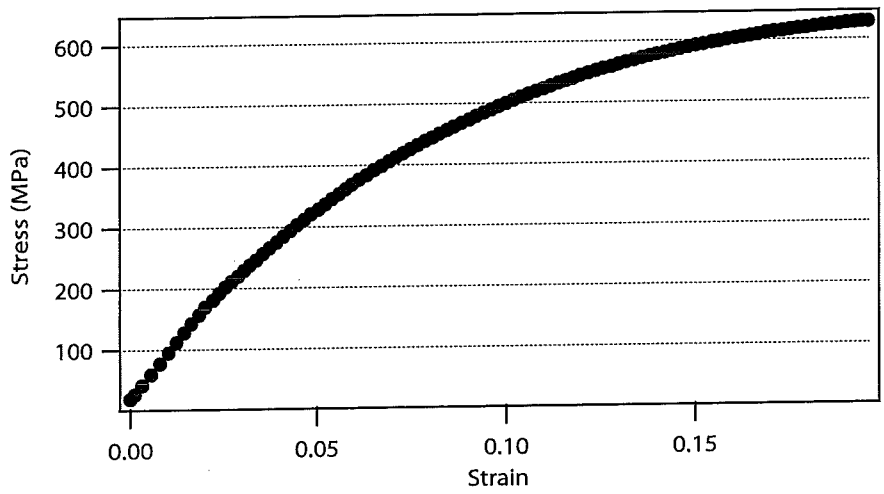

Figure 5.2: Stress-strain curve of deformation of C-Mn steel at 400°C. Data obtained from Gleeble deformation experiment.

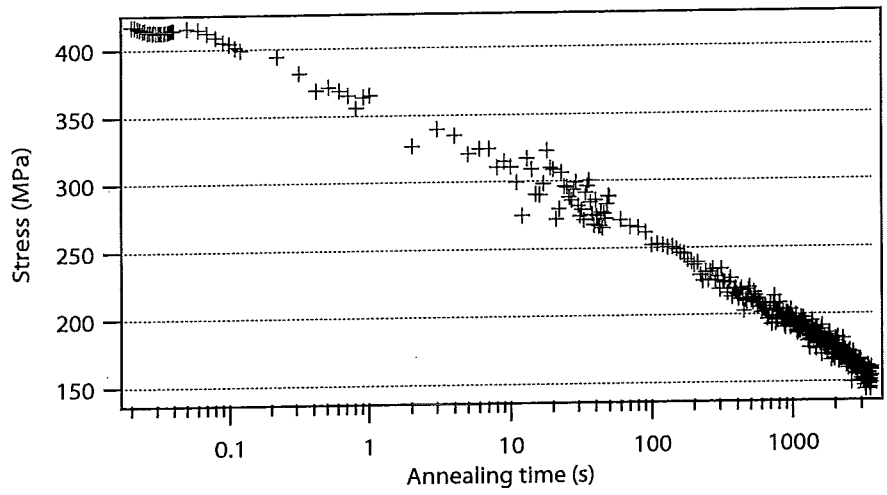

Figure 5.3: Stress-relaxation curve obtained from C-Mn steel at 600°C. Data from [13].

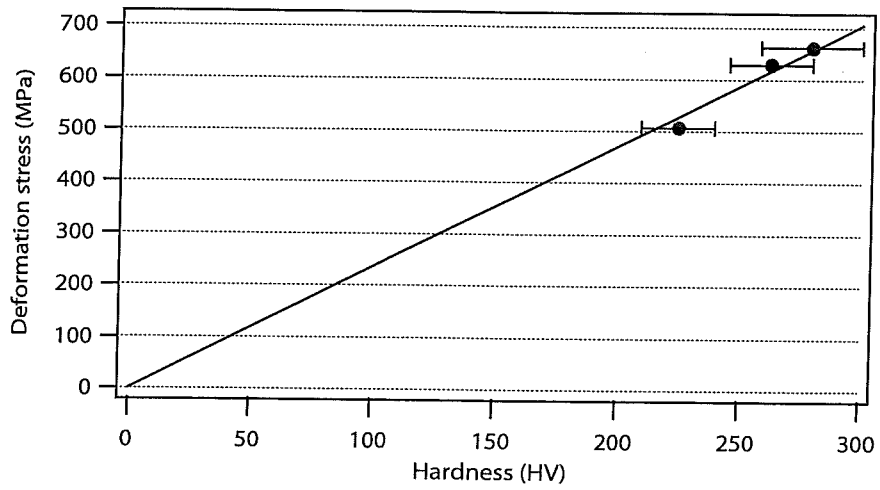

Figure 5.4: Maximum stress during deformation versus average hardness after deformation. The solid line is the fitted curve $\sigma_{def} = C_{C-Mn}\ H_V$ with $C_{C-Mn} = 2.35$ MPa HV^{-1}

have been determined. The average hardness for each sample has been plotted with the stress at the deformation end point, see figure 5.4. A proportional relation has been assumed, giving the following relation between the hardness H_V and the deformation stress σ_{def}:

$$\sigma_{def} = 2.35\ H_V\ [\text{MPa}] \tag{5.2}$$

From equation 5.2 and the average hardness of the undeformed C-Mn steel (175 HV), the corresponding yield stress is determined to be 412 MPa. The average hardness of the sample with strain 0.15 is 262 HV. This gives a hardness increase due to deformation of 87 HV, which corresponds to $\sigma_D = 224$ MPa, using equation 5.2. However, the applied deformation is not uniform over the thickness of the sample, leading to a hardness profile as shown in figure 5.5. Within a circle with radius 3 mm around the centre of the sample, the deformation is uniform. All magnetic experiments have been conducted on samples taken from this part.

The average hardness in this centre area of the sample with strain 0.15 is 270 HV. This gives a hardness increase due to deformation of 95 HV, which corresponds to $\sigma_D = 298$ MPa, using equation 5.2. With equation 3.3, this gives a dislocation density after deformation of $7.6\text{x}10^{14}$ m^{-2}.

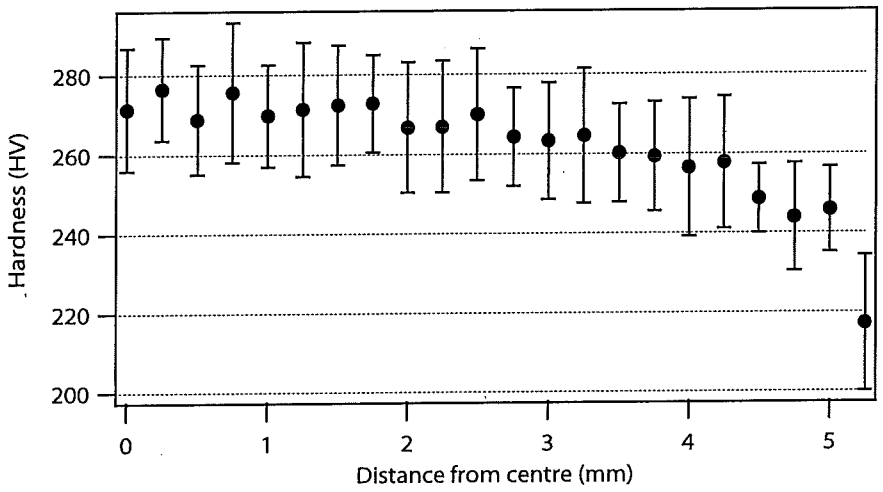

Figure 5.5: Through-thickness hardness profile at half-length of the C-Mn steel after an applied strain of 0.15. Each data point shown is an average of 12 hardness measurements.

2. Bailey and Hirsch [30] have derived the following relation between the hardness increase due to dislocations $H_{V,D}$ and the dislocation density:

$$H_{V,D} \propto \sqrt{\rho_D} \tag{5.3}$$

Nakashima *et al.* [31] have experimentally conducted the following relation between the hardness and dislocation density in low alloyed steels:

$$H_V = 70 + 3\text{x}10^{-6}\sqrt{\rho_D} \tag{5.4}$$

With H_V as shown in the figures and ρ_D in m^{-2}. Using equation 5.4, an initial dislocation density of $1.0\text{x}10^{15}$ m^{-2} is obtained.

Both estimations for the dislocation density after deformation are based on the change in hardness due to deformation. However, the measured hardness is an average of the various phases present in the material. For the C-Mn steel, with 0.19% carbon content, the microstructure consists of 75 vol% ferrite and 25 vol% pearlite. For multi-phase materials a simple rule of mixture can be used to determine the hardness, if the volume fractions of the phases are not too small and the hardness values are not too distinct [32–35]:

$$H_V = \sum_i f_i \, H_{V,i} \tag{5.5}$$

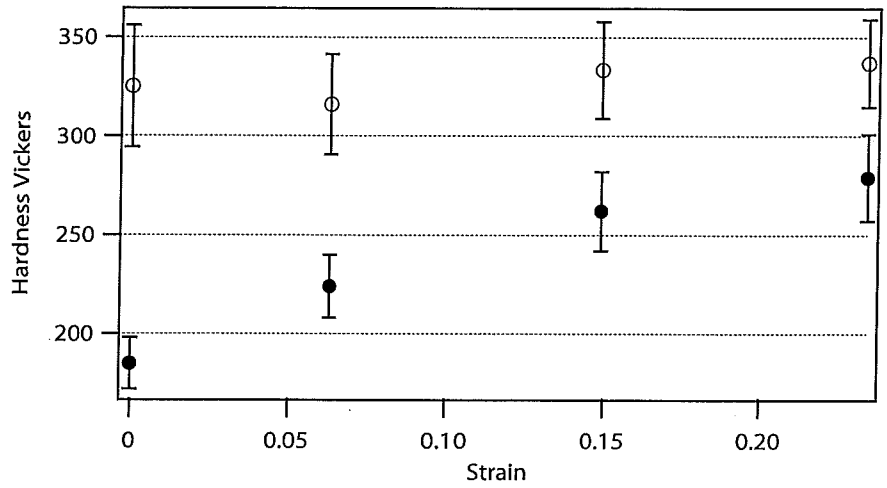

Figure 5.6: Vickers hardness as function of applied strain. The solid circles represent the average macrohardness (HV500) of the sample cross-section. The open circles represent the average microhardness (HV25) of the pearlite in the centre region of the cross-section.

Filling in the fractions ferrite (f_f) and pearlite (f_p) of the C-Mn steel:

$$H_V = f_f \, H_{V,f} + f_p \, H_{V,p} \tag{5.6}$$

Figure 5.6 shows that the hardness of the pearlite does not change significantly with increasing strain, while the average hardness does increase. Therefore, also ρ_D is approximately constant in the pearlite. This has as a consequence that the increase in hardness is purely caused by an increasing hardness of the ferrite phase. Using equation 5.6, the increase in measured hardness can be related to the increase in hardness of the ferrite:

$$\Delta H_V = f_f \, \Delta H_{V,f} \tag{5.7}$$

And thus, equation 5.7 can be used to determine the hardness increase of the ferrite phase from the measured hardness:

$$\Delta H_{V,f} = f_f^{-1} \Delta H_V \tag{5.8}$$

Equations 3.3 and 5.4 both relate the increase in yield stress / hardness to the square root of the dislocation density. Thus, from equation 5.8, it follows that the dislocation density in the ferrite $\rho_{D,f}$ can be determined from the dislocation density that was determined assuming homogeneous deformation $\rho_{D,hom}$:

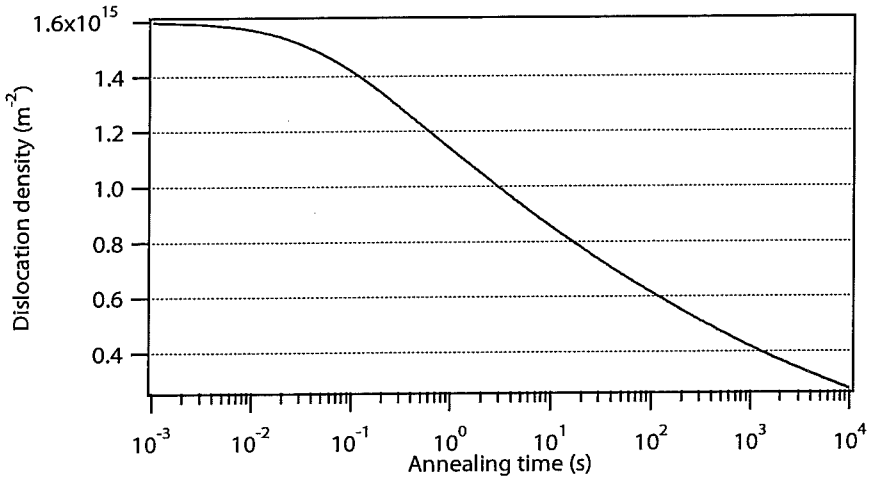

Figure 5.7: Modelled dislocation density as function of annealing time, using equation 5.1, an initial dislocation density of $1.6\text{x}10^{15}$ m^{-2} and other parameters as listed in table 5.2.

$$\rho_{D,f} = f_f^{-2}\rho_{D,hom} \tag{5.9}$$

For the C-Mn steel, $f_f = 0.75$. According to the first approach, the dislocation density would now become $1.4\text{x}10^{15}$ m^{-2} and from the second approach, the dislocation density would become $1.8\text{x}10^{15}$ m^{-2}. Both methods lead to reasonable dislocation densities, comparable to the values reported by Smith [13]. Figure 5.7 shows the dislocation density as a function of annealing time, based on equation 5.1 and the values as listed in table 5.2. For the initial dislocation density, the average value of $1.6\text{x}10^{15}$ m^{-2} is used. The values for the activation energy and activation volume are taken from [13].

5.2 IF steel

5.2.1 Microstructure

Figure 5.8 shows the microstructure of the IF steel after annealing (step one in section 4.1). The micrograph shows a purely ferritic microstructure with an average grain size of 100 μm. The hot rolling direction does not show in the microstructure.

Figure 5.9 shows the microstructure of the IF steel after deformation and several stages of stress-relaxation. Figure 5.9D indicates a finer grain struc-

Table 5.2: Values as used for the variables in the dislocation recovery model.

Variable	Value
ν_D	5.08×10^{13} s^{-1}
E	149 GPa
G	$\frac{3E}{8}$
b	0.249 mm
F_T	2
C_D	0.3
Q_0	251 kJ mol^{-1}
k_B	1.38×10^{-23} m^2 kg s^{-2} K^{-1}
T	673 K
V_a	5×10^{-28} m^3

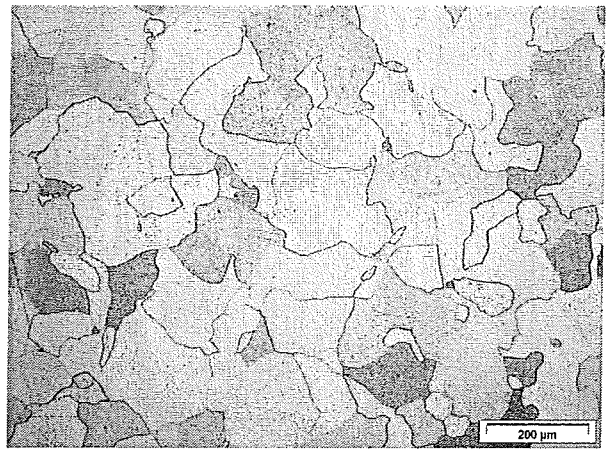

Figure 5.8: Micrograph of IF steel after annealing. Surface was etched with a mixture of picral and nital.

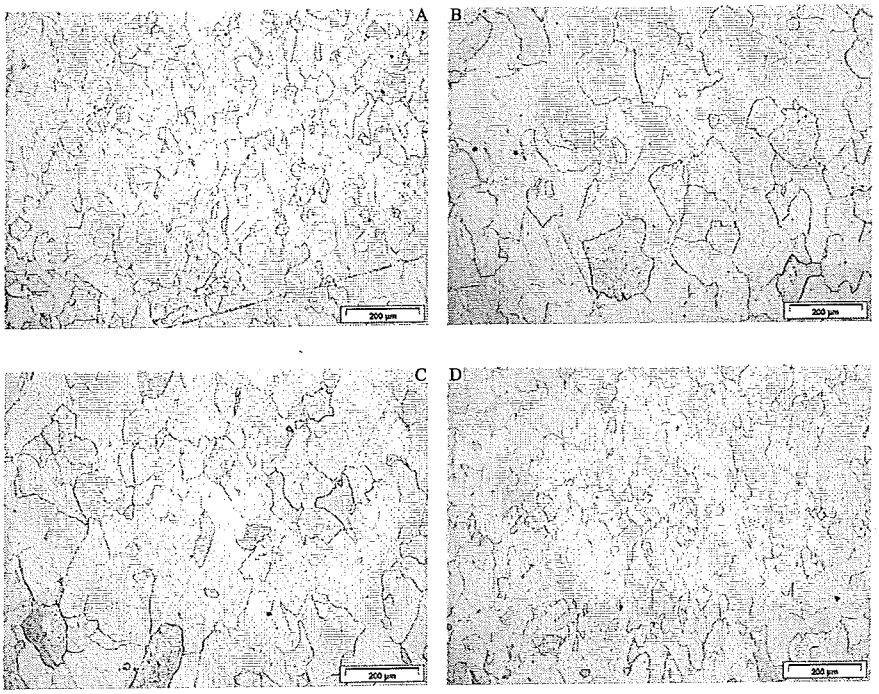

Figure 5.9: Figure A shows the microstructure of the IF steel after deformation. Figures B–D show the microstructure of the IF steel after stress-relaxation. The stress-relaxation times were: B: 16 min; C: 32 min; D: 64 min. Surface was etched with a mixture of picral and nital.

ture for the sample that has been annealed for 64 min. It is likely that this difference in grain structure will affect the magnetic properties. To obtain more detailed information on these changes and to see if (partial) recrystallisation can be the cause of this finer grain structure, EBSD experiments have been conducted on the IF steel samples that have been annealed for 32 and 64 min.

Figure 5.10 shows the grain size charts for both samples. The grains are determined from the crystallographic orientation of the EBSD pixels. If the angle between the crystallographic orientation of neighbouring pixels is larger than 15°, then this is considered a grain boundary. Figure 5.10 confirms the finer grain structure for the 64 min annealed sample.

Figure 5.11 shows the image quality map for the two samples. The image quality is derived from the contrast in the observed Kikuchi patterns by summing the detected peaks in the Hough transform. When this contrast is higher, the Kikuchi patterns can be recognised more clearly, leading to higher peaks in the Hough transform. The image quality is affected by several things,

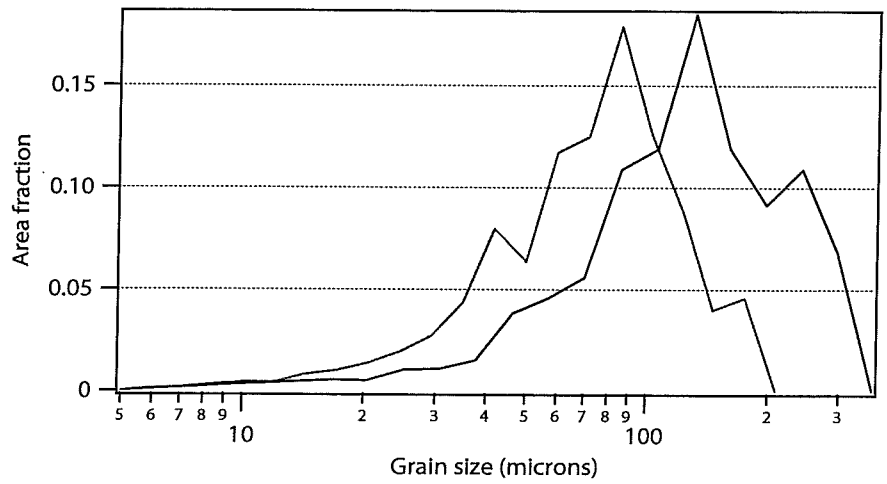

Figure 5.10: Grain size charts for samples that have been annealed for 32 min (black) and 64 min (red). The grain boundaries are defined by neighbouring EBSD pixels having a minimum misorientation angle of 15°. The area average grain sizes are 142 μm (32 min annealed) and 79 μm (64 min annealed)

such as the surface quality of the sample, the settings of the experimental set-up and distortions in the lattice. The latter is related to the local dislocation density. Within one scan, variations in the image quality reveal differences in local dislocation density in the material. Since lattice distortion is not the only parameter affecting the image quality, one needs to be careful when comparing image quality maps for different samples.

In figure 5.11, grain boundaries are plotted. These grain boundaries are determined from the crystallographic orientation of the EBSD pixels. The blue lines represent the high-angle grain boundaries, which are defined by having a minimum angle of 15°. These are the same grain boundaries as have been used for the grain size chart. In figure 5.11A, some regions are present with seemingly many small grains. These grains are no true grains, but are a consequence of pseudosymmetry, which causes an artefact in the determination of the crystallographic orientation. Since in figure 5.10 the area fraction is plotted instead of the number fraction, this figure is not significantly affected by this artefact.

The green lines in figure 5.11 represent the grain boundaries with a crystallographic misorientation angle of $5 - 15°$. The red lines in figure 5.11 represent the grain boundaries with a crystallographic misorientation angle of $2 - 5°$. These grain boundaries are the low-angle grain boundaries. The density of low-angle grain boundaries is related to the local strain. Regions

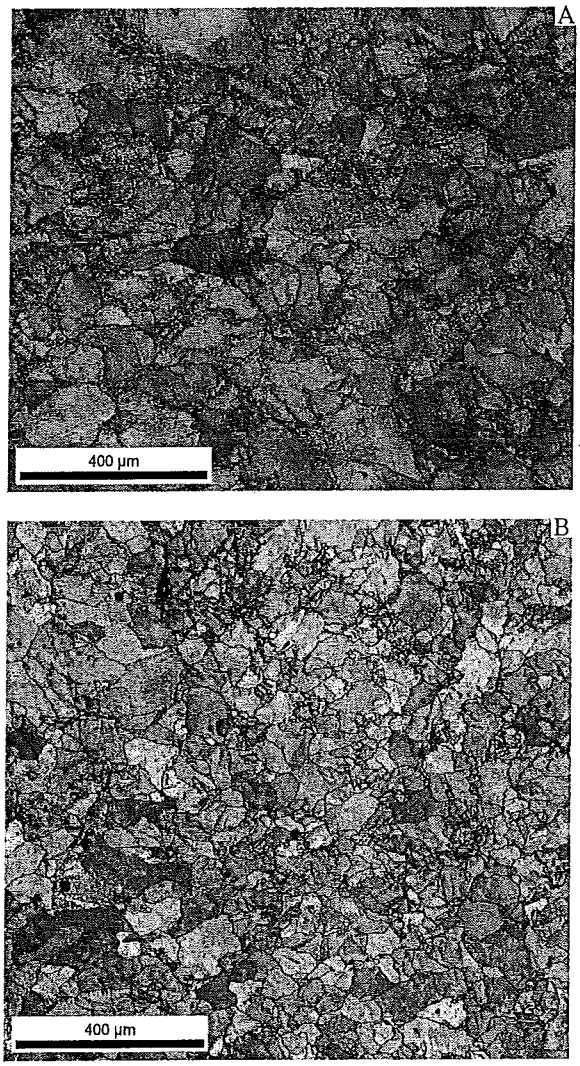

Figure 5.11: Image quality maps for samples that have been annealed for 32 min (A) and 64 min (B). The blue lines represent the grain boundaries with a crystallographic misorientation angle of more than 15°. The green lines represent the grain boundaries with a crystallographic misorientation angle of $5 - 15°$. The red lines in represent the grain boundaries with a crystallographic misorientation angle of $2 - 5°$. The brightness of each pixel represents the image quality of this pixel. The compression axis is vertical.

Table 5.3: Total length of grain boundaries in IF steel samples that have been annealed for 32 and 64 min after deformation. Three grain boundary types are distinguished, based on the misorientation angle. The lengths are given in mm, for a total scan surface of 1.21x1.02 mm.

Misorientation angle range	32 min annealed	64 min annealed
$2-5°$	133.9	50.6
$5-15°$	20.6	6.9
$>15°$	53.8	69.5

with a high low-angle grain boundary density have a high dislocation density.

Figure 5.11 confirms the finer grain structure of the 64 min annealed sample, when compared to the 32 min annealed sample. It also shows that the 64 min annealed sample has significantly less regions with a high low-angle grain boundary density than the 32 min annealed sample. Table 5.3 lists the total length for the three types of grain boundaries for both samples to quantify this difference. The image quality map and grain boundary structure show that the 64 min annealed sample has a finer grain structure and less regions with high dislocation density than the 32 min annealed sample.

Figure 5.12 shows the Kernel average misorientation (KAM) maps for both samples. For each pixel, the crystallographic orientation angle with each of its neighbouring pixels is determined. Then, the average is calculated, which is the Kernel average misorientation. For this calculation, a threshold value is set. If the angle between pixels is larger than this threshold value, it is not taken into account. For these KAM maps, the threshold angle is 5°. Second neighbours are also taken into account.

From figure 5.12, it appears that in the 32 min annealed sample, significantly more regions are present with a high KAM than in the 64 min annealed sample. A high KAM relates to a large local lattice distortion and thus a high local dislocation density. Since the KAM analysis only uses neighbouring pixels and no grain statistics, it is not affected by the effect of pseudosymmetry. Figure 5.13 shows the KAM distributions for both samples. The average KAM for the 64 min annealed sample is 1.24°. The average KAM for the 32 min annealed sample is 1.52°.

The EBSD results show that the grain structure in the 64 min annealed sample is significantly finer than in the 32 min annealed sample. These results also show that the 32 min annealed sample has a higher dislocation density than the 64 min annealed sample. Also, the 32 min annealed sample has more dislocation rich regions than the 64 min annealed sample. These results would indicate that recrystallisation has occurred in between 32 and 64 min

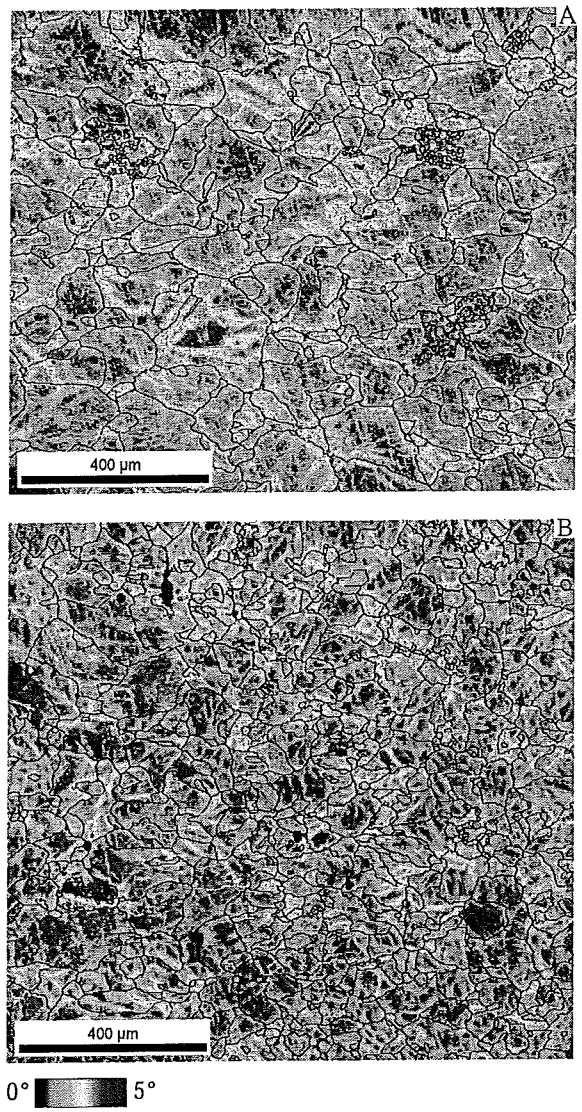

Figure 5.12: Kernel average misorientation maps for samples that have been annealed for 32 min (A) and 64 min (B). The black lines represent the grain boundaries with a crystallographic misorientation angle of more than 15°. The white lines represent the grain boundaries with a crystallographic misorientation angle of $5 - 15°$. The threshold angle is 5° and second neighbours are taken into account. The key for these colour coded maps is shown at the bottom of the figure. The compression axis is vertical.

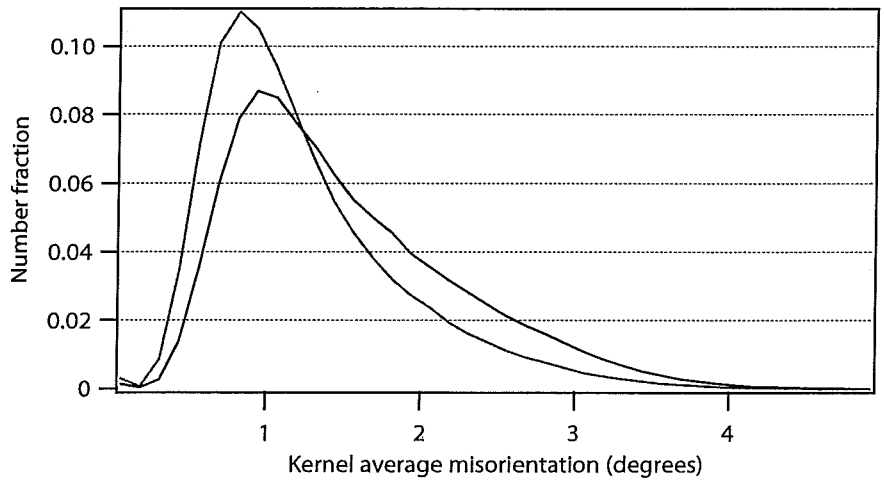

Figure 5.13: Kernel average misorientation distributions for samples that have been annealed for 32 min (black) and 64 min (red). The threshold angle is 5° and second neighbours are taken into account. The average KAM for the 64 min annealed sample is 1.24°. The average KAM for the 32 min annealed sample is 1.52°.

annealing at 400°C.

However, the EBSD results have also shown that the deformation has mainly lead to forming strain bands within the grains. The grains themselves have not been significantly deformed. This grain deformation is regarded as essential to accommodate for recrystallisation leading to grain refinement. Also, if grain refinement due to partial recrystallisation would have occurred in the 64 min annealed sample, the recrystallised grains should be clearly distinguishable from the non-recrystallised grains. This is not the case.

Summarising, the conclusions of the EBSD experiments are:

- The grain structure of the 64 min annealed sample is significantly finer than of the 32 min annealed sample.
- The dislocation density in the 64 min annealed sample is significantly lower than in the 32 min annealed sample.
- It is very unlikely that these differences are a consequence of recrystallisation.

These difference cause the 64 min annealed sample to be significantly different from the other samples. The time frame of this study did not allow for a further analysis of the possible causes for this observed difference.

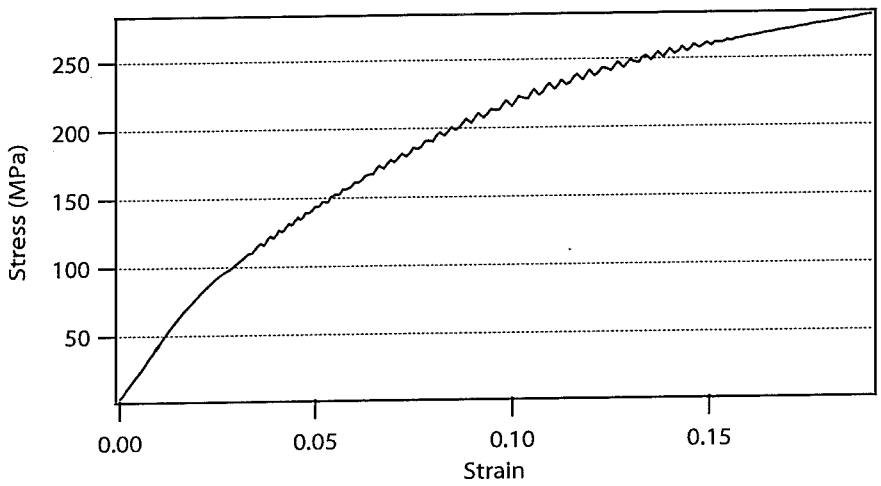

Figure 5.14: Stress-strain curve of deformation of IF steel at 400°C. Data obtained from Gleeble deformation experiment.

5.2.2 Deformation and relaxation

Figure 5.14 shows a typical stress-strain curve for the application of a strain of 0.20 at 400°C in the IF steel. Similarly to the C-Mn steel, this curve does not appear to be a regular stress-strain curve for the deformation of ferritic steel. This is caused by limited stiffness of the Gleeble interior. For the IF steel samples, a programmed strain of 0.20 resulted in an average plastic strain of 0.12 in the centre of the sample.

Figure 5.15 shows a stress-relaxation curve for the IF steel. From this curve, the values for Q_0 and V_a as used in the dislocation recovery model can not be obtained. This is caused by instability of the Gleeble set-up, leading to small variation in the elastic strain, and possibly by NbC precipitation. Due to sample dimensions and relaxation temperature, the small elastic strains cause significant inaccuracies in the stress relaxation determination. NbC precipitation causes an extra term in $\sigma(t)$ that is not covered by the stress-relaxation model. Therefore, the same values for the variables in this model will be used as for the C-Mn steel. In both cases, ferrite recovery is modelled.

Similarly as for the C-Mn steel, the initial dislocation density has been determined using the hardness values. The same two approaches have been used. As only ferrite was present, no correction for the presence of hard phases was required.

1. Samples have been deformed to several strains and hardness profiles have been determined. The average hardness for each sample has been

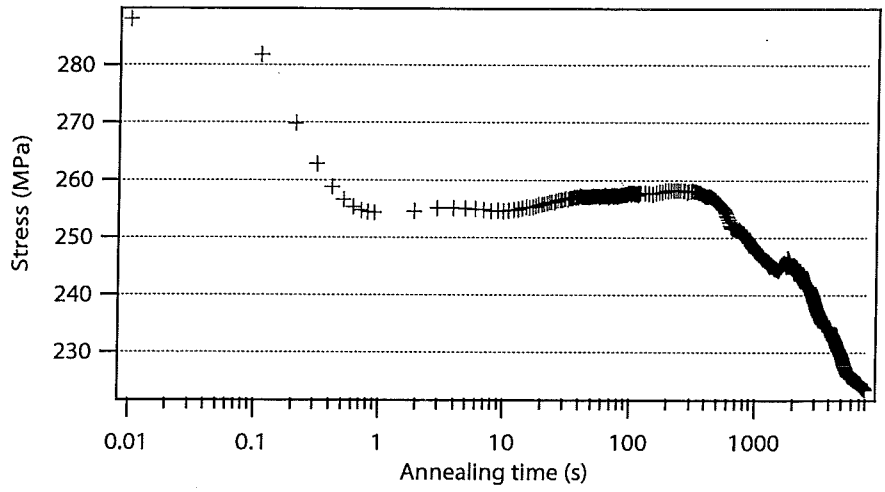

Figure 5.15: Stress-relaxation curve obtained from IF steel at 400°C.

plotted with the stress at the deformation end point, see figure 5.16. A proportional relation has been assumed, giving the following relation between the hardness H_V and the deformation stress σ_{def}:

$$\sigma_{def} = 2.05\ H_V \text{ MPa} \tag{5.10}$$

From equation 5.10 and the average hardness of the undeformed IF steel (84 HV), the corresponding yield stress is determined to be 172 MPa. The average hardness of the sample with strain 0.12 is 139 HV. This gives a hardness increase due to deformation of 55 HV, which corresponds to $\sigma_D = 114$ MPa, using equation 5.10. However, the applied deformation is not uniform, leading to a hardness profile as shown in figure 5.17. Within a circle with radius 3 mm around the centre of the sample, the deformation is more uniform. All magnetic experiments have been conducted on samples taken from this part of the samples.

The average hardness in this centre area of the sample with strain 0.12 is 145 HV. This gives a hardness increase due to deformation of 61 HV, which corresponds to $\sigma_D = 125$ MPa, using equation 5.10. With equation 3.3, this gives an initial dislocation density of $2.4\text{x}10^{14}$ m^{-2}

2. Using equation 5.4, an initial dislocation density of $4.1\text{x}10^{14}$ m^{-2} is obtained. It is to be noted that the hardness value for the undeformed IF steel is within the range given by Nakashima *et al.* [31] for a dislocation density of 0 m^{-2}.

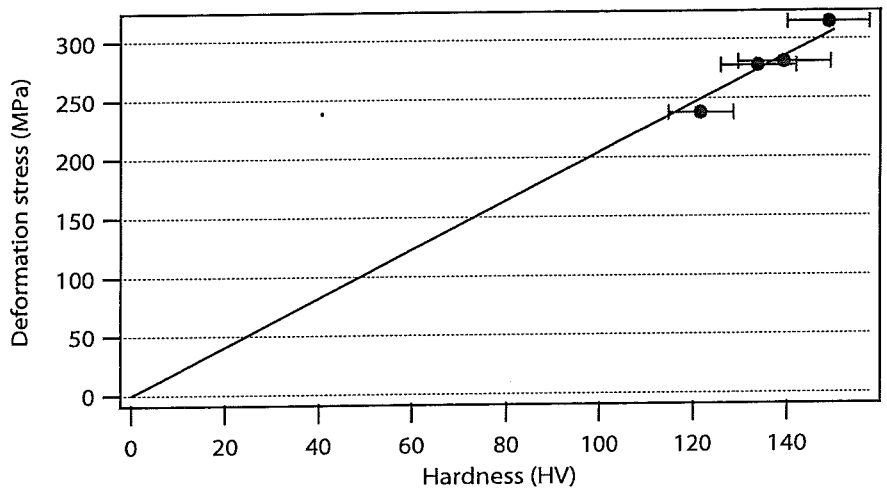

Figure 5.16: Maximum stress during deformation versus average hardness after deformation. The solid line is the fitted curve $\sigma_{def} = C_{IF}\ H_V$ with $C_{IF} = 2.05$ MPa HV^{-1}

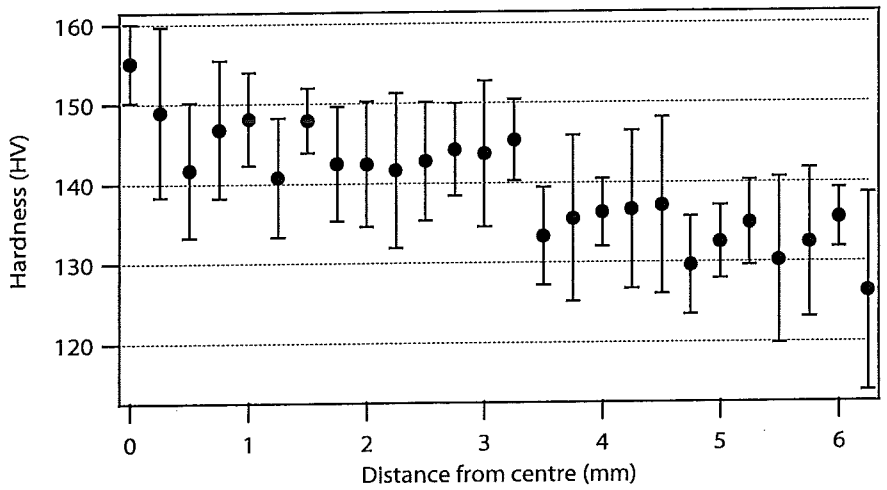

Figure 5.17: Through-thickness hardness profile at half-length of the IF steel after an applied strain of 0.12. Each data point shown is an average of 6 hardness measurements.

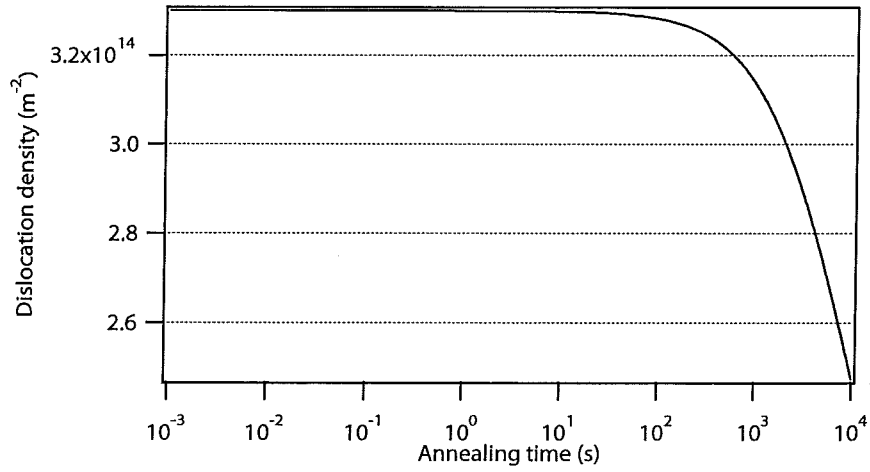

Figure 5.18: Modelled dislocation density as function of annealing time, using equation 5.1, an initial dislocation density of $3.3x10^{14}$ m^{-2} and other parameters as listed in table 5.2.

The dislocation density in the IF steel is significantly lower than in the C-Mn steel. This is caused by:

1. The strain in the IF steel (0.12) is lower than in the C-Mn steel (0.15).
2. The IF steel consists of only ferrite, while the C-Mn steel consists of both ferrite and pearlite. The ferrite phase will therefore deform more in the C-Mn steel than in the IF steel with similar total strain.

Figure 5.18 shows the dislocation density as function of annealing time, based on equation 5.1 and the values as listed in table 5.2. For the initial dislocation density, the average value of $3.3x10^{14}$ m^{-2} is used. For the other parameters, the same values as for the C-Mn steel have been used, as both deal with ferrite recovery.

5.2.3 Domain structure

Figure 5.19 shows an MFM image of an undeformed IF steel sample and figure 5.20 shows the corresponding AFM image, showing the grain boundaries. Figure 5.21 combines these images by plotting the grain boundaries in the MFM image. As explained in section 4.4, it is not possible to determine the exact magnetic structure from the MFM image. However, intensity differences are caused by differences in the local magnetisation. Therefore, these

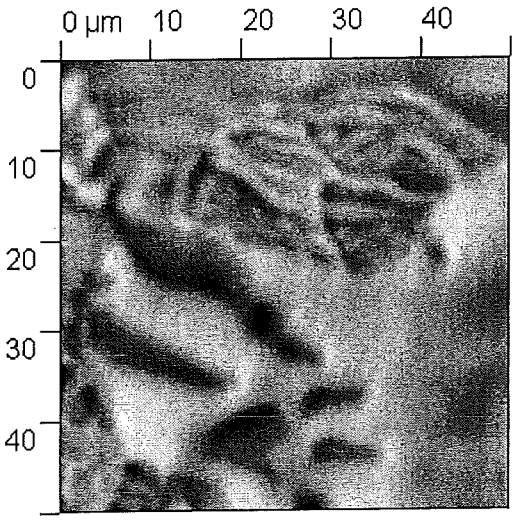

Figure 5.19: MFM image of IF steel after annealing.

images give an impression of the domain structure. From figure 5.21, three provisional conclusions can be drawn:

1. Magnetic domains are significantly smaller than the ferrite grains.
2. Grain boundaries cause sharp transitions in the domain structure.
3. The projection of the domain structure on the surface can be very different in adjacent grains.

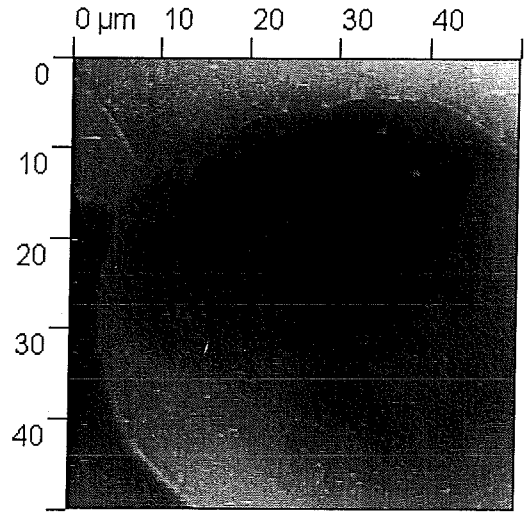

Figure 5.20: AFM image of IF steel after annealing, taken from the same location as figure 5.19.

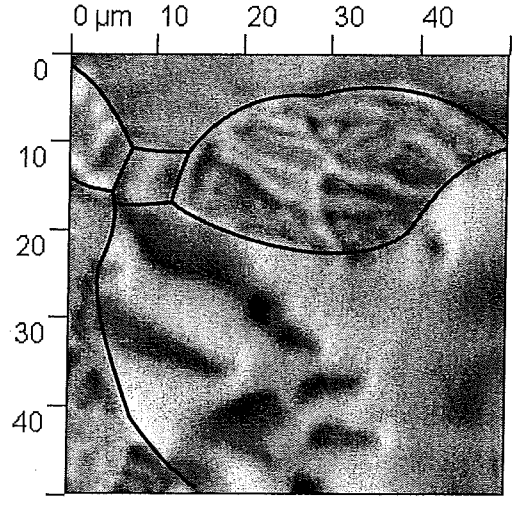

Figure 5.21: MFM image of IF steel after annealing (figure 5.19). Using the AFM image (figure 5.20), the grain structure is drawn in the MFM image.

6. Magnetisation curves

Using a Vibrating Sample Magnetometer (VSM), the magnetisation curves properties of the materials have been determined. For this purpose, samples have been used with finite dimensions, see section 4.5. Therefore, a demagnetising field is present, affecting the measured magnetisation curve. To determine the real magnetisation curves, the measured curves need to be corrected for this demagnetising field. The first section describes this correction. Then, the results for the different materials are presented and discussed.

6.1 Demagnetisation

6.1.1 Determination of demagnetising factor

As described in subsection 2.3.3, for any sample that is not magnetically closed, a demagnetising field is present. This field affects the true field in the sample by equation 2.15. Using the measured applied field and sample magnetisation and the demagnetising factor, the true field can be calculated. This procedure has been performed on IF steel samples with different aspect ratios, for which demagnetising factors have been determined using figure 2.2. Table 6.1 gives the sizes and corresponding values for N_d from figure 2.2 for these samples. Figure 6.1 shows the magnetising curves before demagnetisation correction and 6.2 shows the same curves after demagnetisation correction.

These magnetisation curves have been obtained using a step size of 0.1 mT (80 A m^{-1}) in the low applied field range. Table 4.1 (VSM programme 1) shows the step size as a function of applied field.

At first sight, this demagnetisation correction seems to be an improvement. However, zooming in on the low-field part of the curves, it becomes clear that this demagnetisation correction does not remove the differences between the measured magnetic curves. As figure 6.3 shows, performing this demagnetisation correction may even lead to curves that clearly can not represent true material properties.

However, this poor result is obtained by using demagnetising factors read from figure 2.2. This figure is a graph with logarithmic axes, which likely

Table 6.1: Diameters and N_d of cylindrical steel samples used for determining demagnetisation correction. The length of the samples is 3.0 mm. For IF steel, a sample with diameter 2.5 mm was not used. For C-Mn steel, a sample with diameter 0.5 mm was not used.

Diameter (mm)	N_d
0.5	0.032
1.0	0.083
1.5	0.13
2.0	0.18
2.5	0.25

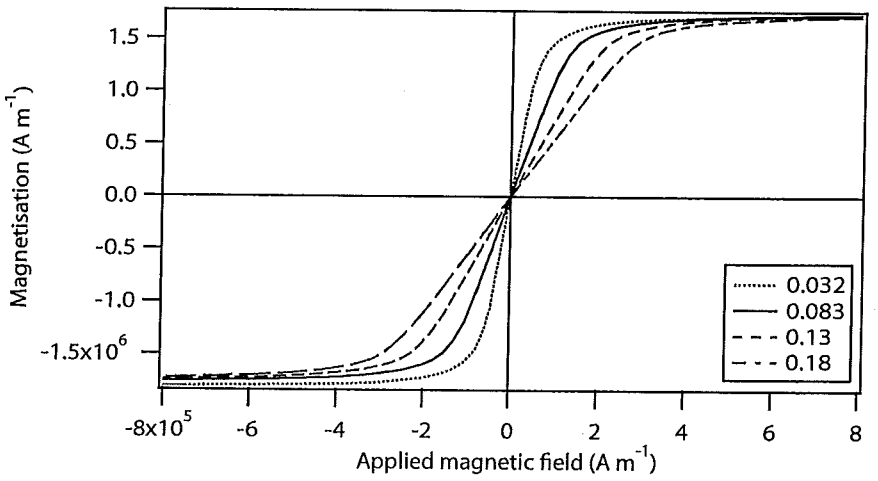

Figure 6.1: Magnetisation curves for undeformed IF steel. The curves were taken from cylindrical samples of 3 mm length and different diameters. The corresponding values for N_d are listed in the legend. These curves are determined using a minimum step size of 0.1 mT.

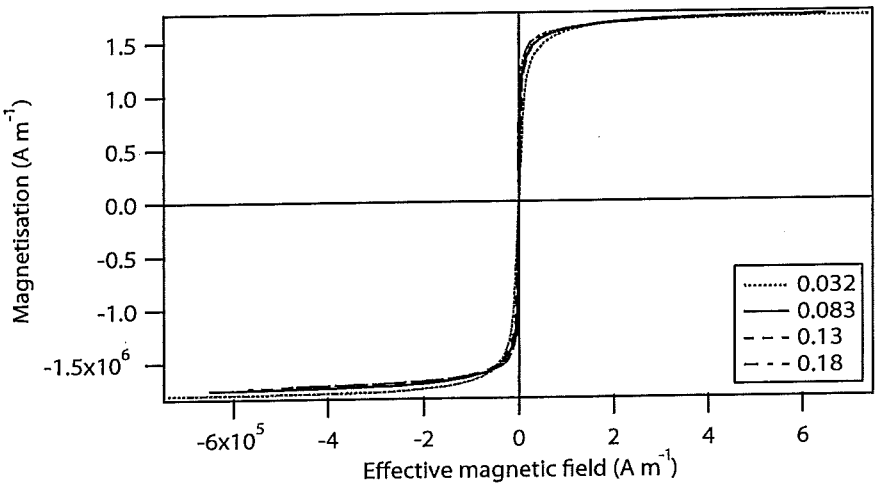

Figure 6.2: The same magnetisation curves as in figure 6.1, corrected for demagnetisation by equation 2.15 and the listed values for N_d.

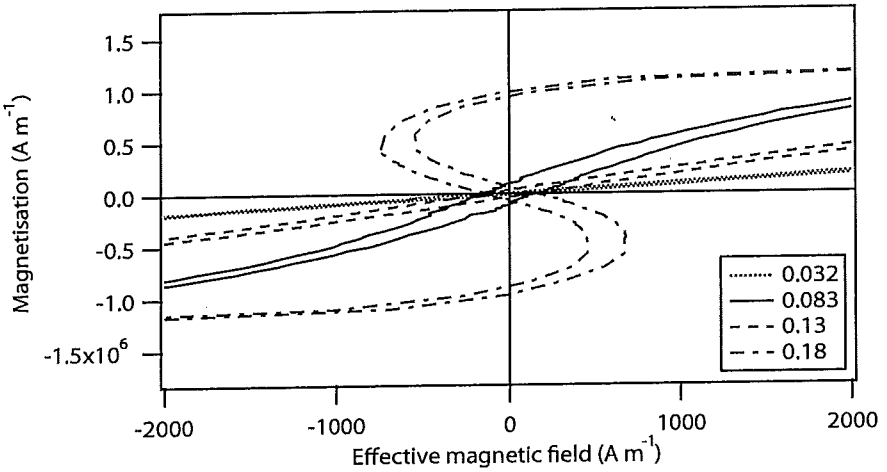

Figure 6.3: The low field part of same curves as in figure 6.2.

Table 6.2: N_d for the same IF steel samples as in table 6.1, determined in two different ways: using figure 2.2 and using equation 6.1.

Diameter (mm)	N_d from figure 2.2	N_d from equation 6.1
0.5	0.032	0.043
1.0	0.083	0.084
1.5	0.13	0.134
2.0	0.18	0.178

causes reading errors to occur. The demagnetisation correction is sensitive to the chosen value for N_d. Therefore, a different approach is required to find the correct value for N_d.

For low applied fields, $\mathbf{H}$ in equation 2.15 is approximately zero. This means that for low applied fields, this equation can be rewritten as:

$$N_d = \left(\frac{d\mathbf{H}_a}{d\mathbf{M}}\right)_{H_a \to 0} \tag{6.1}$$

from which the value for N_d can be determined, using the VSM data in the low field range. Using this approximation, slightly different values for N_d have been determined. Table 6.2 lists the N_d values obtained in the two different ways. Figure 6.4 shows that these values give a better approach to the true magnetisation curves. However, it is still not perfect. Figure 6.5 shows that the experimental scatter in the low-field region causes the demagnetisation correction to be inconsistent. This inconsistency appears to be significant with respect to the sensitivity of the correction for the exact value of N_d, such that this demagnetisation correction is still not successful.

N_d needs to be known accurately to correct the data for demagnetisation. Using equation 6.1 appears to give a more accurate value for N_d than using figure 2.2. However, the accuracy of the determined N_d depends on the quality of the obtained magnetisation data in the low-field region. From figures 6.4 and 6.5, it appears that using a minimum step size of 0.1 mT (VSM programme 1) does not give data that is sufficiently accurate. This seems to be caused by instability in the VSM equipment, causing scatter and some drift when in this low-field region for too long. A solution would be to shorten the experiment time by lowering the data point density, as is done by applying VSM programme 2. The step size in the low applied field range for this programme is 5 mT, see also table 4.2. The time in the low field region ($|\mathbf{H}_a| < 8$ kA m^{-1}) is then reduced from 20 min to 1 min.

Figures 6.6 and 6.7 show the results for the same samples as figures 6.4 and 6.5, obtained using VSM programme 2. It appears that the consistency

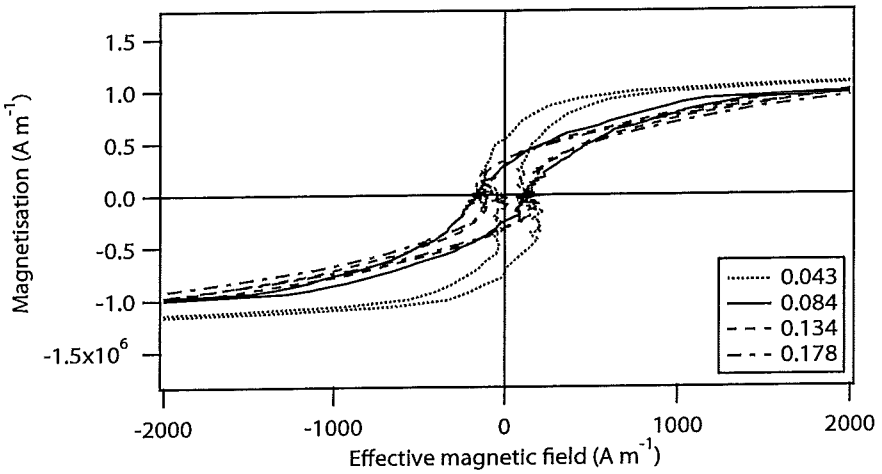

Figure 6.4: The low field part of the same curves as in figure 6.1, using the values for N_d as indicated. These values have been determined by applying equation 6.1 to the data obtained for an applied field of -8 kA m^{-1} – $+8$ kA m^{-1}.

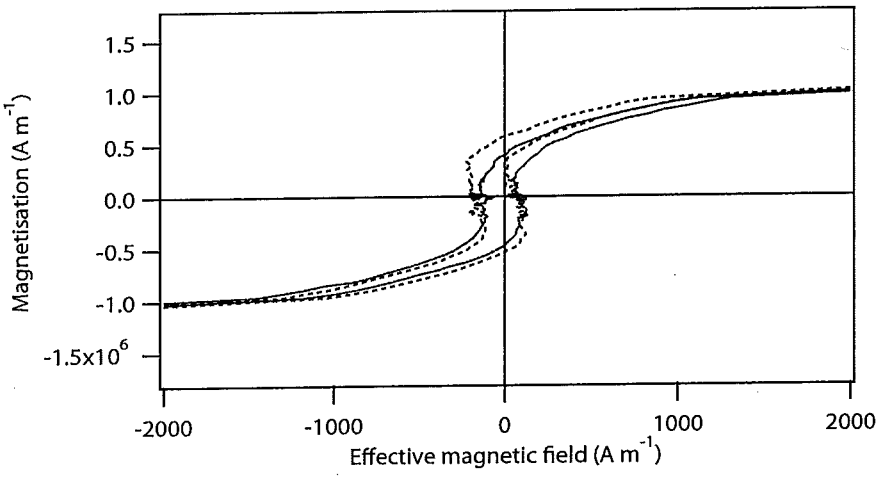

Figure 6.5: The low field part of two curves obtained from the same sample, with $N_d \approx 0.084$. The N_d values have been determined by applying equation 6.1 to the data obtained for an applied field of -8 kA m^{-1} – $+8$ kA m^{-1}. These curves are determined using a minimum step size of 0.1 mT.

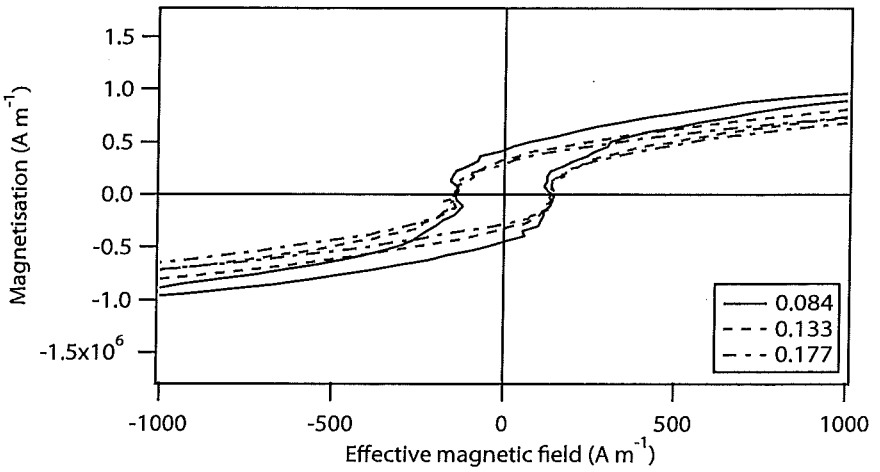

Figure 6.6: The low field part of the same samples as in figure 6.1, with the exception of one sample, using the values for N_d as indicated. These values have been determined by applying equation 6.1 to the data obtained for an applied field of -8 kA m^{-1} – $+8$ kA m^{-1}. These curves are determined using a minimum step size of 5 mT.

has improved and the demagnetisation correction appears to give reasonable corrected magnetisation curves. However, as figure 6.6 shows, the correction does not give the same magnetisation curves for samples of different shape.

Figure 6.8 shows $\mathbf{M}_r$ for samples of different diameters, as listed in table 6.1. This shows that demagnetisation still affects the determination of $\mathbf{M}_r$, even although a correction had been applied. This effect is significant when comparing it to the sensitivity of $\mathbf{M}_r$ to the correct value of N_d and when compared to the scatter of identical measurements.

A trend appears with decreasing $\mathbf{M}_r$ with increasing N_d, even after correction. A possible explanation for this effect can be the non-uniformity of the demagnetising field. As explained in subsection 2.3.3, the magnetisation is not uniform and the demagnetising field depends on the diverging field lines at the ends of the cylindrical samples. The details of these diverging field lines depend on the shape of the sample. Therefore, the non-uniformity of the demagnetising field will also depend on the sample shape.

The details of the diverging field lines will also depend on the magnetic state of the material. It is shown in subsection 2.3.3 that they depend on the susceptibility. As the susceptibility is not constant, this will cause the demagnetisation to change during magnetisation. Also, a material that is fully saturated has a uniform magnetisation. Therefore, the non-uniformity of the magnetisation, and with that the non-uniformity of the demagnetisation, will

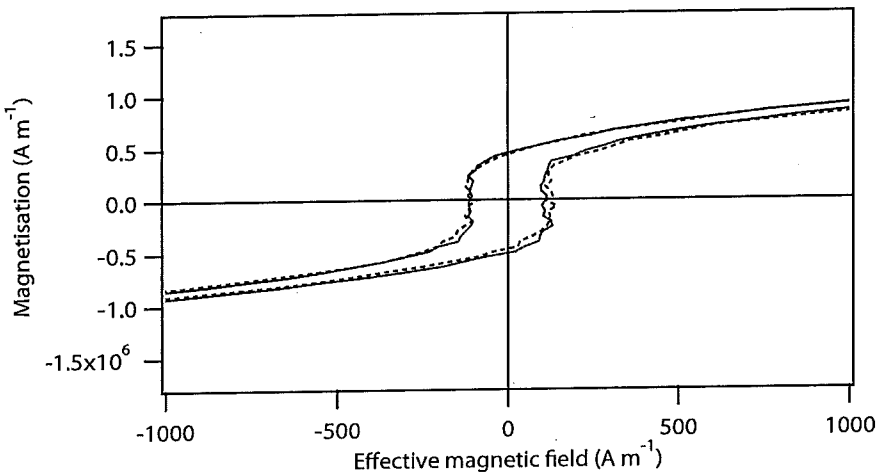

Figure 6.7: The low field part of two curves obtained from the same sample, with $N_d \approx 0.084$. The N_d values have been determined by applying equation 6.1 to the data obtained for an applied field of -8 kA m^{-1} – $+8$ kA m^{-1}. These curves are determined using a minimum step size of 5 mT.

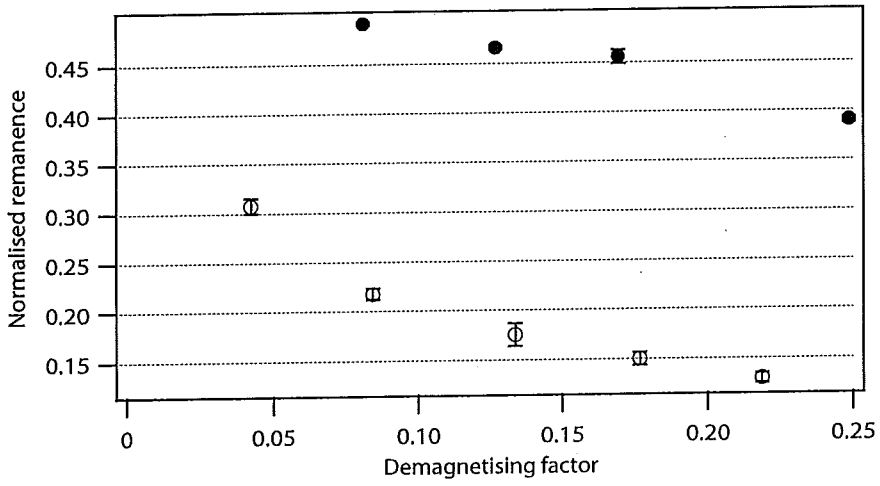

Figure 6.8: $\mathbf{M}_r$ after demagnetisation correction as determined for samples of different diameter and thus N_d. The open circles represent samples obtained from one undeformed IF steel sample. The closed circles represent samples obtained from one undeformed C-Mn steel sample. $\mathbf{M}_r$ is normalised to $\mathbf{M}_s$ and therefore dimensionless.

depend on the magnetisation. A consequence would be that the demagnetising factor depends on the magnetic state as well. The magnetisation at the remanence is higher than the magnetisation at the part of the curve that is used for determining N_d. Therefore, N_d at the remanence might be slightly different than N_d at low applied fields. Considering the sensitivity of $\mathbf{M}_r$ to N_d, it is imaginable that this will affect the obtained values for $\mathbf{M}_r$ significantly. This effect will be different for different sample shapes, possibly leading to the results as shown figure 6.8. For a cylindrical sample with infinite length, and thus $N_d = 0$, these effects would not be present.

Based on figure 6.8, a trend could be fitted to $\mathbf{M}_r(N_d)$. Extrapolation of this trend to $N_d = 0$ would give the value for $\mathbf{M}_r$ that is fully corrected for N_d. The physical background of this trend is unknown. Also, the details of the trend will depend on $\mathbf{M}_r$, as the demagnetising effects causing these trends depend on $\mathbf{M}_r$. A higher $\mathbf{M}_r$ can increase these demagnetising effects, as χ will be have changed more with respect to $\mathbf{H} = 0$. On the other hand, if the magnetisation is more uniform at a higher $\mathbf{M}_r$, these demagnetising effects may decrease. To avoid adding a large extra uncertainty, an extrapolation is not used.

It has been noted that $\mathbf{H}_c$ is independent of demagnetisation. However, it is determined by data points obtained at low fields. It appeared that these data points suffer from significant scatter. Also, the nature of this scatter appeared to depend on the VSM programme used. Therefore, $\mathbf{H}_c$ might be affected by the experimental details. Figure 6.9 shows the $\mathbf{H}_c$ of various samples, obtained by both VSM programmes. $\mathbf{H}_c$ does not appear to be significantly affected by the VSM programme used.

6.1.2 Sensitivity to the demagnetising factor

Several parameters can be used to characterise the magnetisation curve, among which the most used are:

1. Saturation magnetisation $\mathbf{M}_s$
2. Coercivity $\mathbf{H}_c$
3. Remanence $\mathbf{M}_r$
4. Maximum susceptibility χ_{max}

During deformation and recovery, no phase transformations take place, which causes the fraction of ferromagnetic phase, and thus $\mathbf{M}_s$, to be constant. A variation in $\mathbf{M}_s$ will likely be a consequence of experimental scatter

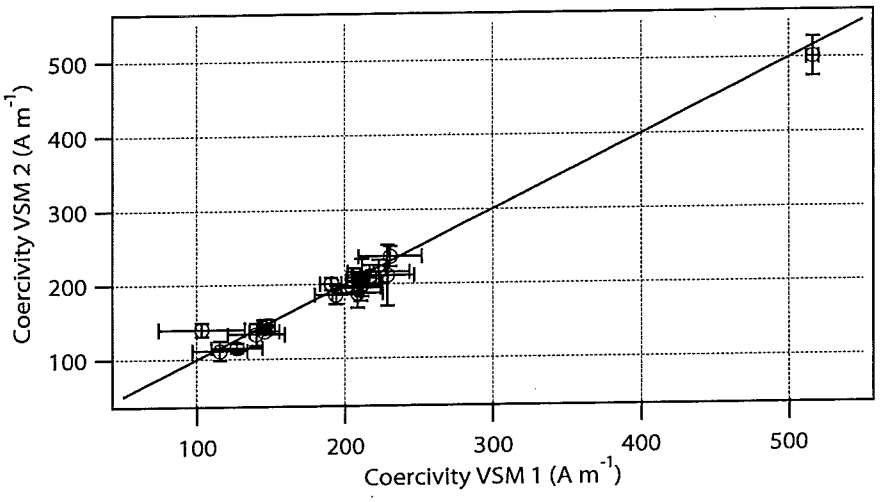

Figure 6.9: $\mathbf{H}_c$ as determined using a minimum step size of 0.1 mT (VSM 1) versus $\mathbf{H}_c$ as determined using a minimum step size of 5 mT (VSM 2) for various IF steel samples and one C-Mn steel sample (top right). The solid line is the function $y = x$.

rather than anything else. $\mathbf{H}_c$ is expected to change due to the change in dislocation density and therefore more interesting. $\mathbf{H}_c$ is not affected by demagnetisation, so the uncertainty in N_d does not affect the obtained value.

Unlike $\mathbf{H}_c$, $\mathbf{M}_r$ and χ_{max} are affected by demagnetisation. To obtain true values for these quantities, a demagnetisation correction needs to be applied. Therefore, these values depend on N_d used for this correction. Figure 6.10 shows $\mathbf{M}_r$ as a function of N_d for one particular undeformed IF steel sample. Using VSM programme 2, the consistency in N_d is of the order of 0.1%. Probably, the accuracy is of the same order. The range for N_d shown is based on the magnetisation data and equation 6.1, which is highlighted.

It is clear that determining N_d very accurately is of high importance in determining $\mathbf{M}_r$. Not only $\mathbf{M}_r$, but also χ_{max} depends on N_d. Figure 6.11 shows χ_{max} as function of N_d for the same sample. From this figure, it appears that at two values for N_d, the two parts of the magnetisation curve are parallel. One of those two values can not be correct, as it gives a negative χ_{max}, which is not realistic. The other value is more realistic, especially as it is close to the maximum value for $\chi_{max}(N_d)$. It is tempting to assume that this value for N_d will be a better value than the one obtained initially. However, as figure 6.12 shows, $\chi_{max}(N_d)$ does not give consistent relations for each sample. This makes it less likely that determining N_d this way is an improvement to using the slope of the magnetisation curve.

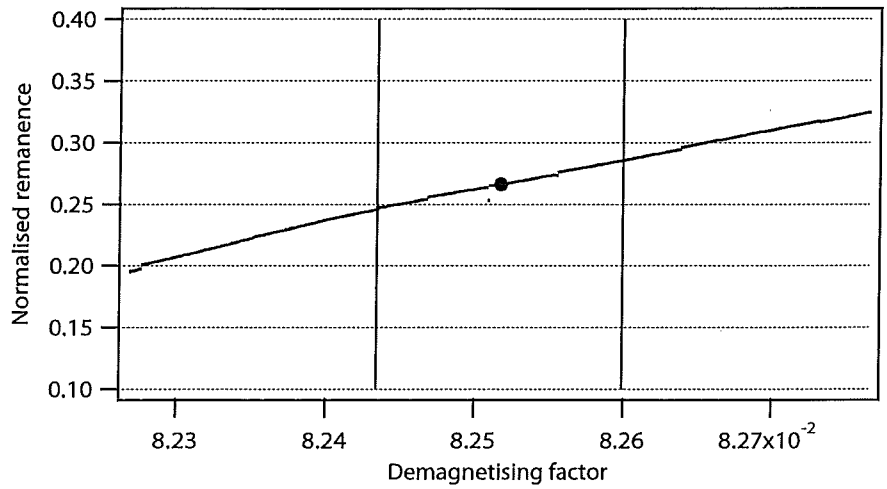

Figure 6.10: $\mathbf{M}_r$ as a function of N_d for one undeformed IF steel sample. For this sample, N_d has been determined to be 0.082517, as pointed by the solid red circle. The vertical lines show the effect of a deviation of 0.1% from this value. $\mathbf{M}_r$ has been normalised to $\mathbf{M}_s$.

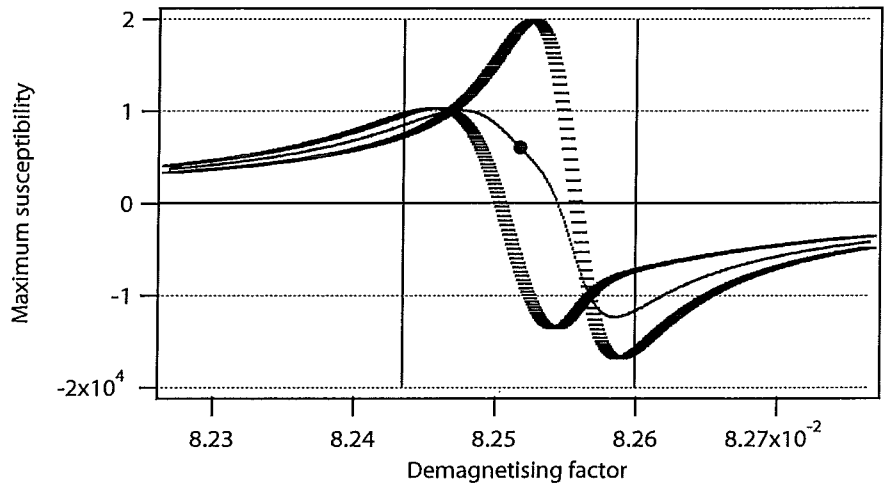

Figure 6.11: χ_{max} as a function of N_d for one undeformed IF steel sample. For this sample, N_d has been determined to be 0.082517, as pointed by the solid red circle. The vertical lines show the effect of a deviation of 0.1% from this value. The error caps indicate the slopes of the two parts of the magnetic hysteresis loop.

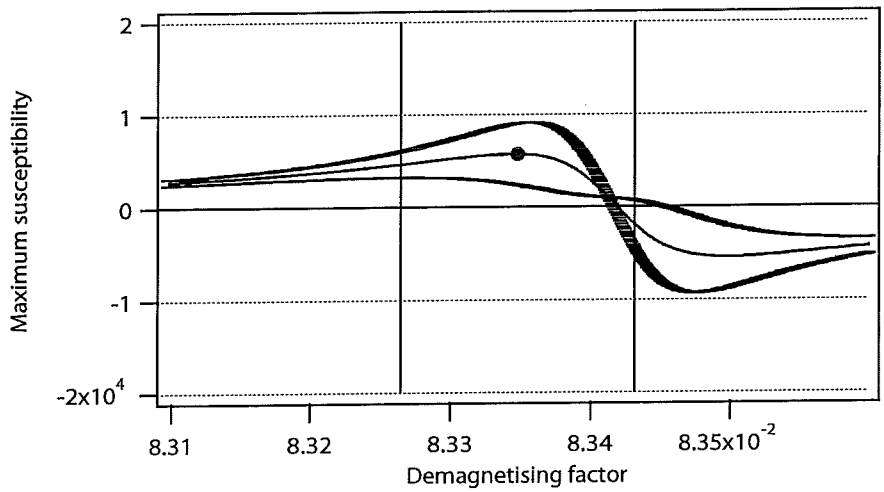

Figure 6.12: χ_{max} as a function of N_d for one annealed IF steel sample. For this sample, N_d has been determined to be 0.083348, as pointed by the solid red circle. The vertical lines show the effect of a deviation of 0.1% from this value. The error caps indicate the slopes of the two parts of the magnetic hysteresis loop.

Using χ_{max} to estimate N_d is not valid, since the value of χ_{max} can vary a lot, even in one sample. Also, the magnetisation curve is not symmetrical, leading to different values for χ_{max} for the two parts of the magnetisation curve. This shows that experimental scatter is present in the magnetisation data at low applied fields, which will cause an error in the determination of N_d.

Data points with $|\mathbf{H}_a| > 0$ A m^{-1} have to be used to determine N_d. Also, scatter is present in the magnetisation data. Therefore, the determination of N_d using equation 6.1 will have a limited accuracy. An attempt has been made to use $\chi_{max}(N_d)$ to find a value for N_d that is closer to the real value. However, $\chi_{max}(N_d)$ does not give a consistent image and the values for χ_{max} are subject to significant variation. Therefore, this method has been rejected.

It was stated that using equation 6.1 to determine N_d yields a small error in N_d, since the assumption $\mathbf{H} = 0$ is not exact for the data points used. In principle, this assumption is valid at the remanence point, since the remanent magnetisation is defined as the magnetisation at $\mathbf{H} = 0$. Using this principle creates a circular reasoning. $\mathbf{M}_r$ would be used to determine N_d. However, $\mathbf{M}_r$ can only be determined if N_d is known. Still, an attempt has been made to determine N_d this way. However, this method resulted in physically impossible magnetisation curves and has therefore been rejected.

Using equation 6.1 to determine N_d gave significantly better results than using figure 2.2. However, this determination of N_d still has a limited accuracy, while the sensitivity of the obtained magnetisation curve to the correct value of N_d is very high. Therefore, attempts have been made to improve the determination of N_d. However, these attempts have not been successful. Therefore, the value obtained using equation 6.1 will be used as best approximation for N_d.

6.2 IF steel

For the IF steel, all annealing steps were performed in the Gleeble, directly after deformation. This means that for each annealing step, a different sample was used. From each sample, three VSM samples were made. The annealing times varied from 1 s to 4 h, in approximately equidistant steps on logarithmic scale. Also samples were prepared without deformation and with deformation, but without subsequent annealing. The results presented are obtained using a minimum step size of 5 mT.

6.2.1 Magnetisation curve

Figures 6.13 and 6.14 shows a typical magnetisation curve for undeformed IF steel. Figure 6.15 shows the spread of the various magnetisation curves obtained from the same sample. Clearly, this spread will cause significant scatter in the obtained coercivity. For the remanence, this scatter is partly caused by inaccuracies in the determination of N_d. As a variation in $\mathbf{M}_s$ will likely be a consequence of experimental scatter, the contribution of this to the scatter in the remanence can be reduced by normalising with respect to the measured $\mathbf{M}_s$.

6.2.2 Coercivity

Figure 6.16 shows the coercivity of the IF steel as a function of annealing time at 400°C. Two extra data points are shown:

0.11 s	Undeformed state
0.2 s	Deformed state

Equations 3.14 and 5.1 are combined to model the coercivity as a function of annealing time:

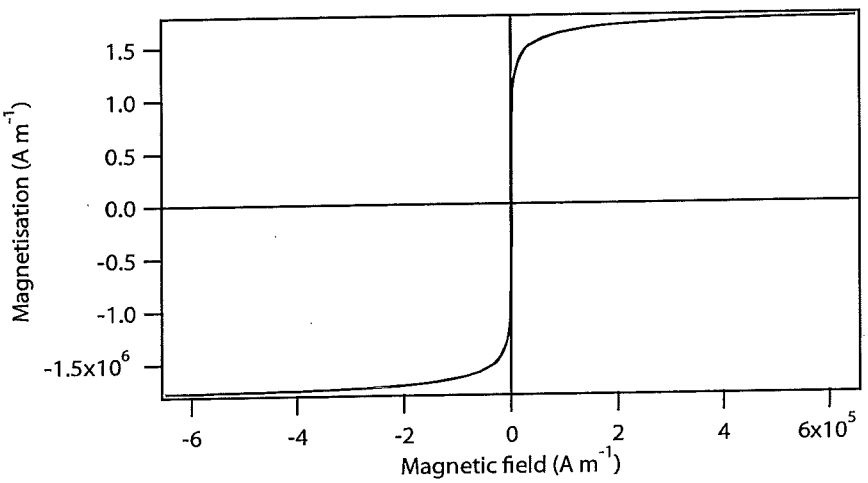

Figure 6.13: Typical magnetisation curve for undeformed IF steel after demagnetisation correction. To obtain a symmetrical magnetisation curve, the whole curve has been shifted along the **H**-axis for 946 A m^{-1}.

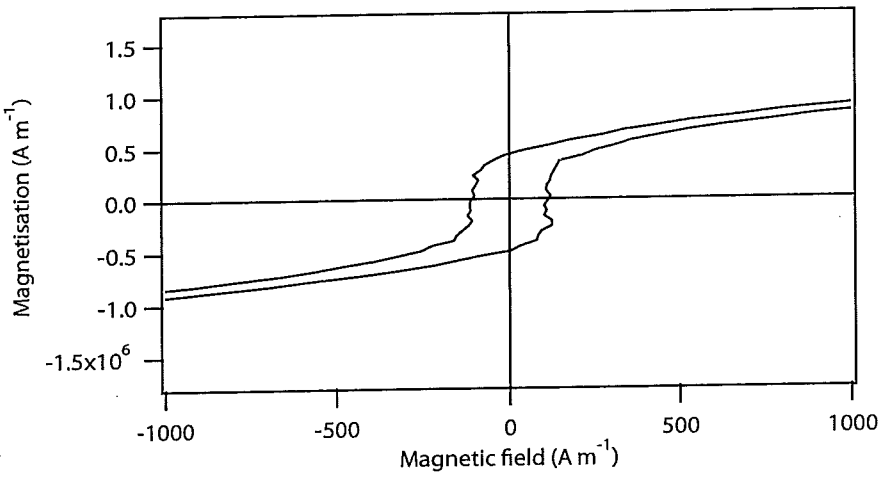

Figure 6.14: Close-up of a typical magnetisation curve for undeformed IF steel after demagnetisation correction. To obtain a symmetrical magnetisation curve, the whole curve has been shifted along the **H**-axis for 946 A m^{-1}.

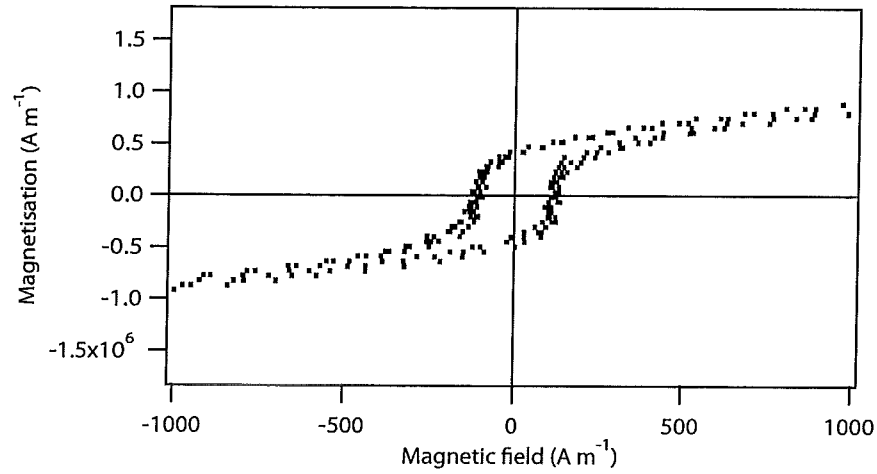

Figure 6.15: The low field part of three magnetisation curves for the same sample of undeformed C-Mn steel. The spread in the data points shows the scatter in the magnetisation curves.

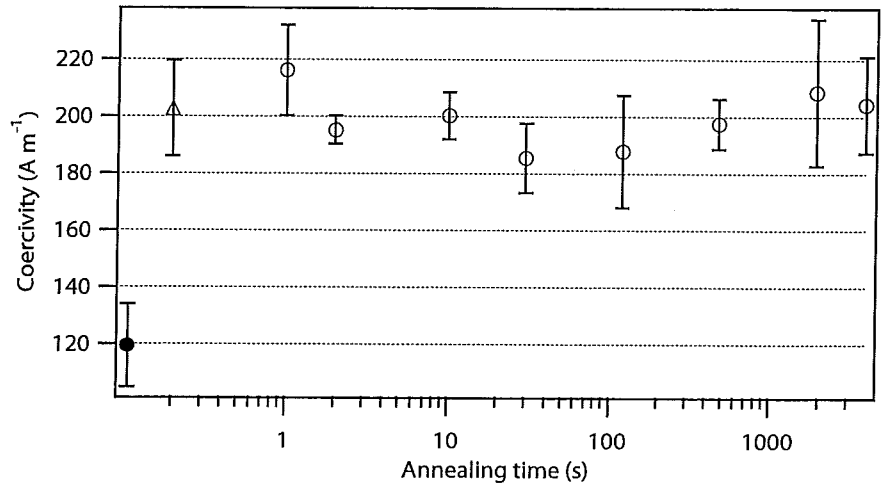

Figure 6.16: The coercivity of IF steel as a function of the annealing time. The closed circle at 0.11 s represents the undeformed state. The open triangle at 0.2 s represents the deformed state. The open circles show the coercivity after annealing at 400°C for the time indicated.

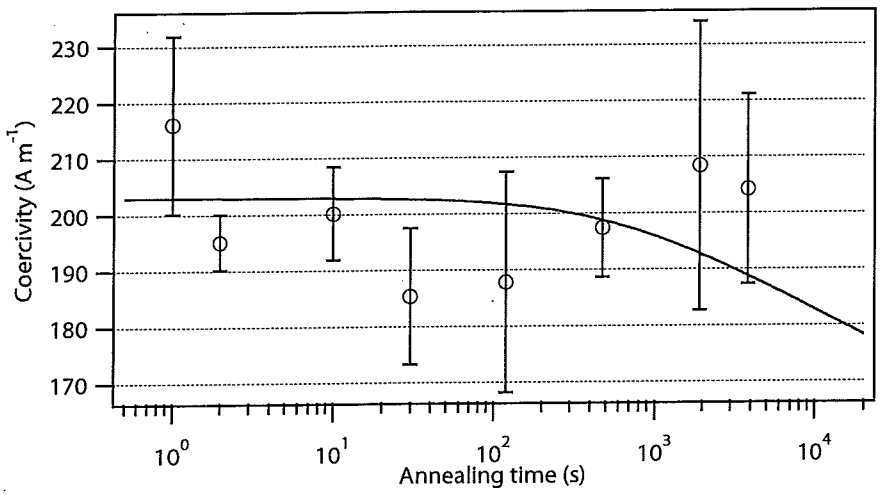

Figure 6.17: The coercivity of IF steel as a function of the annealing time. The solid line shows the modelled coercivity from equation 6.2.

$$\frac{d\mathbf{H}_c}{dt} = -\frac{64Gb\mathbf{H}_c^2}{9F_T^2C_DE\gamma_D}\nu_D \exp\left(-\frac{Q_0}{k_BT}\right)\sinh\left(\frac{\mathbf{H}_cV_aF_TC_DGb}{k_BT\gamma_D}\right) \qquad (6.2)$$

Figure 6.17 shows the modelled coercivity, using equation 6.2, versus the measured coercivity. Using equation 3.14 the following value for γ_D has been determined:

$$\gamma_D = 4.6 \pm 1.4\text{x}10^{-6}\ \text{A}$$

with the difference in $\mathbf{H}_c$ between the average values for the undeformed and deformed state and the dislocation density as determined in subsection 5.2.2. The starting value for $\mathbf{H}_c$ is the average value for the deformed state. The values for all other parameters are the same as for the recovery model and listed in table 5.2. None of the parameters have been fitted to the coercivity data of the annealed samples. Considering no fitting parameters have been used, the model fits rather well to the data.

The small step size programme has also been applied to the IF steel. Figure 6.18 shows the coercivity obtained by a minimum step size of 0.1 mT of the IF steel as a function of annealing time at 400°C. Figure 6.19 shows the modelled coercivity versus the measured coercivity, using equation 6.2. Similarly as with the large step size programme, using equation 3.14 the following value for γ_D has been determined:

$$\gamma_D = 5.1 \pm 1.4\text{x}10^{-6}\ \text{A}$$

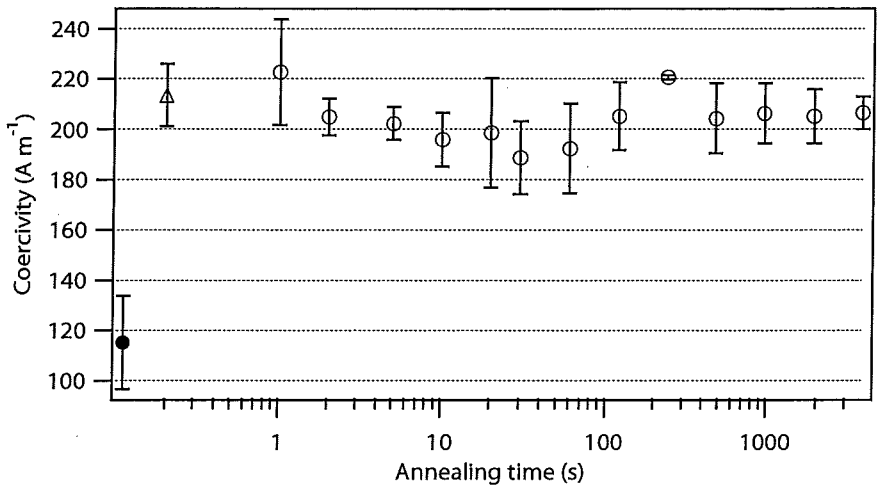

Figure 6.18: The coercivity obtained using a minimum step size of 0.1 mT of IF steel as a function of the annealing time. The closed circle at 0.11 s represents the undeformed state. The open triangle at 0.2 s represents the deformed state. The open circles show the coercivity after annealing at 400°C for the time indicated.

with the difference in $\mathbf{H}_c$ between the average values for the undeformed and deformed state and the dislocation density as determined in subsection 5.2.2. The starting value for $\mathbf{H}_c$ is the average value for the deformed state. The values for all other parameters are the same as for the recovery model and listed in table 5.2. None of the parameters have been fitted to the coercivity data of the annealed samples.

Again, considering no fitting parameters have been used, the model fits rather well to the data. For both series of experiments, the possible forming of niobium-based precipitates during annealing does not seem to affect the coercivity significantly. On the other hand, the coercivity of the sample with the longest annealing time (64 min = 3840 s) also fits well to the model. The optical micrographs and EBSD results showed that the microstructure for this sample is significantly different from the expected microstructure, based on the undeformed sample and the samples with shorter annealing times. Possibly, the finer grain structure and lower dislocation density have opposite effects of similar magnitude.

The relation between the coercivity and dislocation density in IF steel has been determined using two different VSM programmes. From this, the following results are obtained:

$$\gamma_D = 4.9 \pm 1.4\text{x}10^{-6}\ \text{A}$$

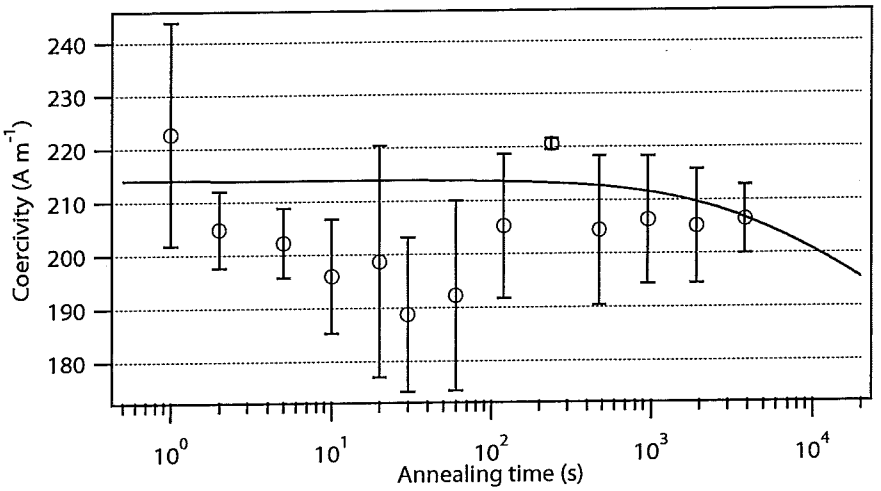

Figure 6.19: The coercivity obtained using a minimum step size of 0.1 mT of IF steel as a function of the annealing time. The solid line shows the modelled coercivity from equation 6.2.

$$\gamma_0 = 120 \pm 15 \text{ A m}^{-1}$$

6.2.3 Remanence

Figure 6.20 shows the remanence of the IF steel as a function of the annealing time. The shown data points are from the same samples as in figure 6.16. The remanence values shown are normalised to the saturation magnetisation, which causes them to be dimensionless.

The remanence does not show a relation to the dislocation density. Figure 6.20 mainly shows a large variation between samples. This variation is larger than would be expected from the variation in one sample. This variation could be due to sample preparation. The samples are not perfect cylinders and the imperfections can be different for different samples. This may lead to effects that are similar as seen for the samples of different diameter, resulting in different demagnetising effects at the remanent magnetisation.

6.3 C-Mn steel

For the C-Mn steel, all samples were quenched directly after deformation, step 2 in section 4.1. VSM samples were made from these deformed samples. For each sample, the magnetisation curve was determined before any

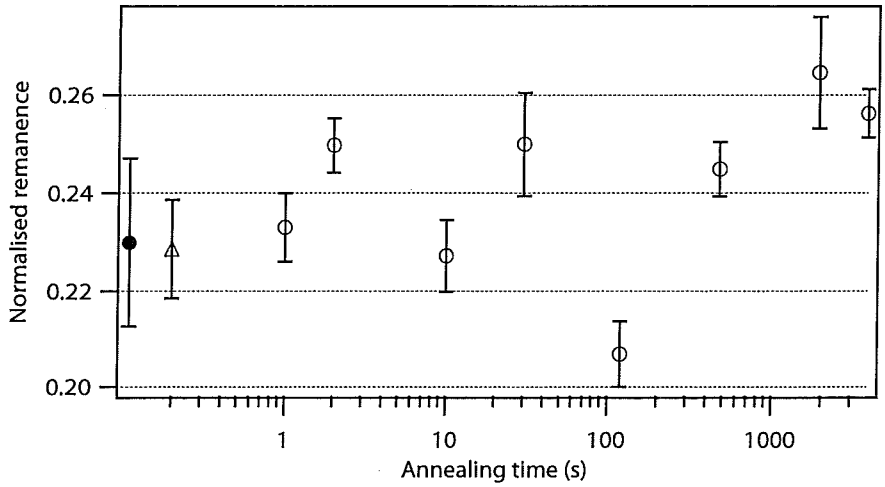

Figure 6.20: The normalised remanence of IF steel as a function of the annealing time. The closed circle at 0.11 s represents the undeformed state. The open triangle at 0.2 s represents the deformed state. The open circles show the normalised remanence after annealing at 400°C for the time indicated.

annealing treatment was applied. Then, each sample received a set of annealing treatments at 400°C and the magnetisation curve was determined after each treatment. The treatments per sample are listed in table 6.3. Also, VSM samples have been taken from undeformed samples and magnetisation curves have been determined. The results presented are obtained by using a minimum step size of 0.1 mT.

6.3.1 Magnetisation curve

Figure 6.21 shows typical magnetisation curves for undeformed and deformed C-Mn steel samples without demagnetisation correction. Figure 6.22 shows the same curves, zoomed in on the low field region. As explained in subsection 6.1.1, a consistent correction for demagnetisation could not be applied to the data obtained by using the small step size programme. The same samples were used for the different annealing stages. Because the large step size programme was developed later, it has not been applied to these samples.

Figure 6.23 shows the spread of the various magnetisation curves obtained from the same sample. Clearly, this spread will cause significant scatter in the obtained coercivity.

The microstructure of the C-Mn steel is affected by the hot-rolling process. This caused formation of pearlite bands, which also return after the

Table 6.3: Annealing times for C-Mn steel at 400°C after deformation in minutes, unless otherwise specified.

Sample	30 s	1	2	4	8	16	32	64	128	2 h at 600°C
1		X		X		X		X		X
2		X			X			X		X
3				X				X		
4	X	X			X	X			X	
5			X				X			
6	X		X		X					
7			X			X			X	
8										X
9	X	X	X	X	X	X	X	X	X	
10	X			X			X			
11										X

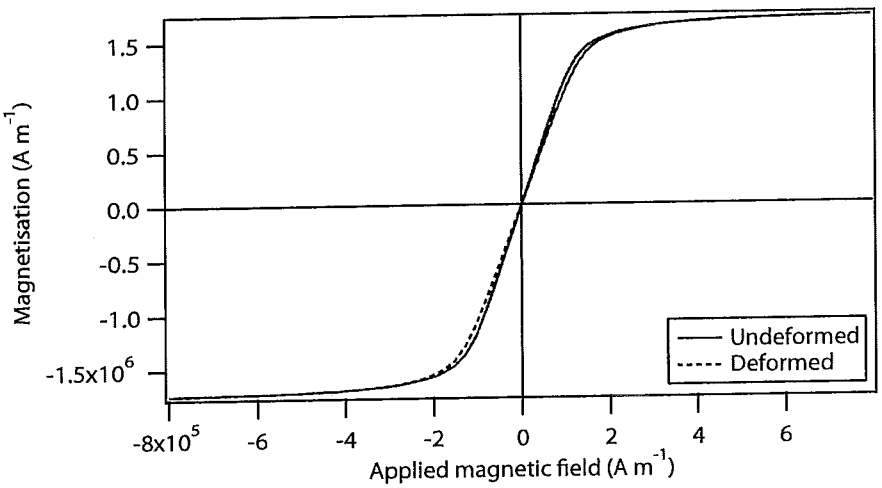

Figure 6.21: Typical magnetisation curves for undeformed and deformed C-Mn steel, not corrected for demagnetisation.

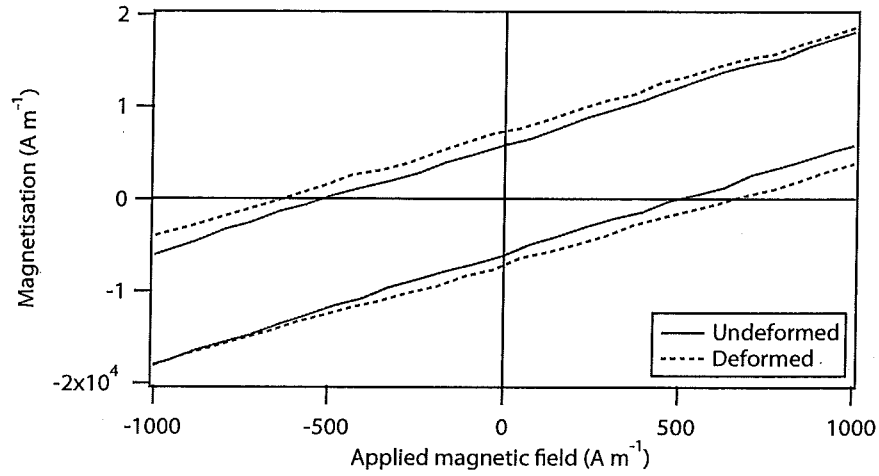

Figure 6.22: The low field part of the typical magnetisation curves for undeformed and deformed C-Mn steel, not corrected for demagnetisation.

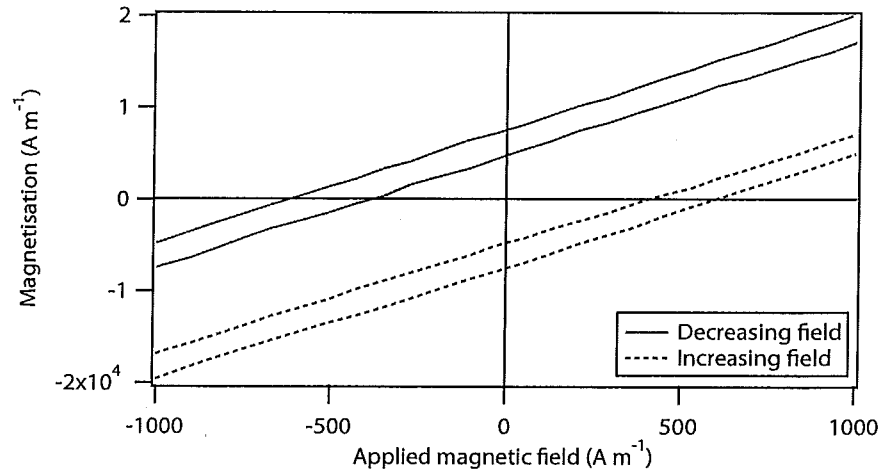

Figure 6.23: The low field part of the magnetisation curve for undeformed C-Mn steel. The two lines shown for each part of the curve are one standard deviation from the average.

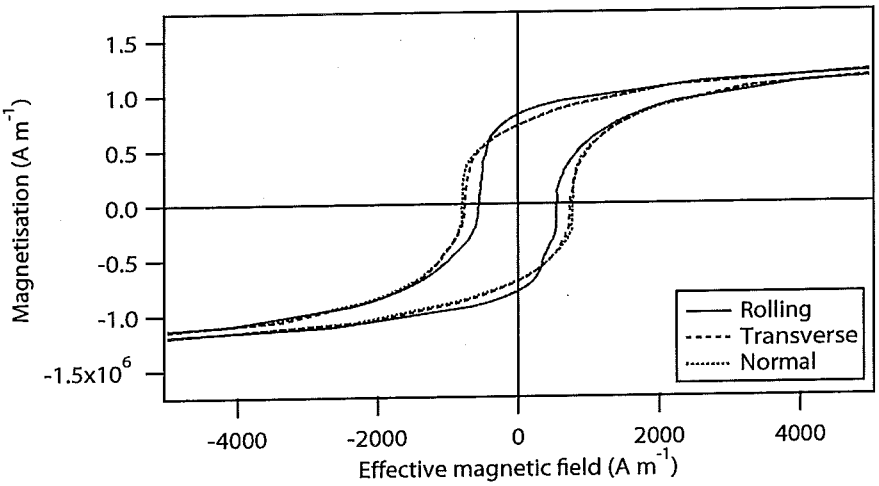

Figure 6.24: The low field part of the magnetisation curves for undeformed C-Mn steel in the three main orientations with respect to the hot-rolling direction, as indicated in the legend. The magnetisation curves have been corrected for demagnetisation. For these samples, $N_d \approx 0.17$.

annealing step, as shown in figure 5.1. These pearlite bands will cause the magnetisation curves to be different in different directions with respect to this hot rolling procedure. Figure 6.24 shows the low field part of the magnetisation curves for the C-Mn steel in the three main orientations. These curves have been corrected for demagnetisation. The magnetisation curve in the rolling direction is significantly different. It has a lower coercivity and a higher remanence. For all other experiments, the magnetisation curves have been applied in the rolling direction.

6.3.2 Coercivity

Figure 6.25 shows the coercivity of the C-Mn steel as a function of annealing time at 400°C. Three extra data points are shown:

1.1 s	Undeformed state
2 s	Deformed state
10^4 s	Recrystallised for 2 hrs at 600°C

Figure 6.26 shows the modelled coercivity versus the measured coercivity, using equation 6.2. Similarly as with the IF steel, using equation 3.14, the following value for γ_D has been determined:

$$\gamma_D = 3.6 \pm 0.6\text{x}10^{-6}\ \text{A}$$

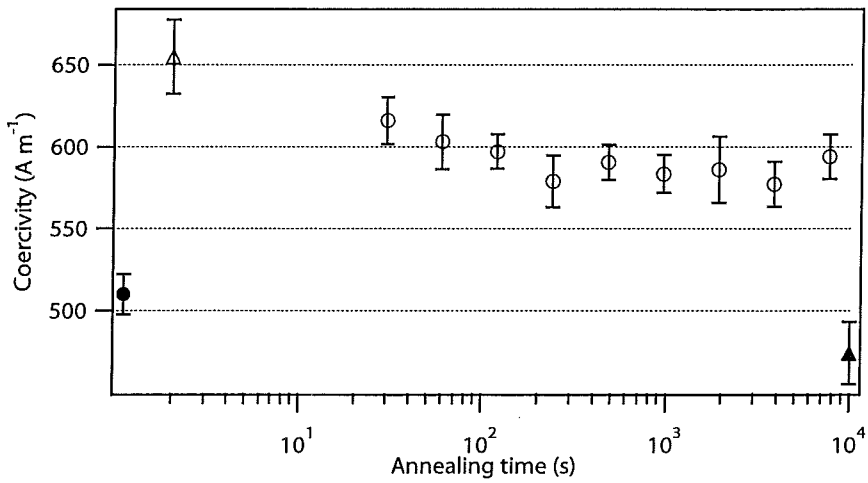

Figure 6.25: The coercivity of C-Mn steel as a function of the annealing time. The closed circle at 1.1 s represents the undeformed state. The open triangle at 2 s represents the deformed state. The closed triangle at 10^4 s shows the coercivity after 2 h annealing at 600°C. The open circles show the coercivity after annealing at 400°C for the time indicated.

with the difference in $\mathbf{H}_c$ between the average values for the undeformed and deformed state and the dislocation density as determined in subsection 5.1.2. The starting value for $\mathbf{H}_c$ is the average value for the deformed state. The values for all other parameters are listed in table 5.2. None of the parameters have been fitted to the coercivity data of the annealed samples. This model fits well to the coercivity data.

It is to be noted that the increase in measured coercivity is not the same as the increase in coercivity due to the contribution of the increased dislocation density in the ferrite phase. From the assumption that the coercivity is the sum of the contribution from each lattice defect, the assumption that a simple rule of mixtures is applicable to the coercivity can be made. Results from Goodenough [36], showing a linear increase of coercivity with pearlite content, suggest that this is indeed the case. This rule of mixtures is similar to the rule of mixtures used in subsection 5.1.2. From this rule of mixtures, the true value of γ_D is $\frac{4}{3}$ times the obtained value, since the C-Mn steel consists of 75% ferrite. This leads to:

$$\gamma_D = 4.8 \pm 0.9\text{x}10^{-6} \text{ A}$$

For the C-Mn steel,

$$\gamma_0 = 510 \pm 12 \text{ A m}^{-1}$$

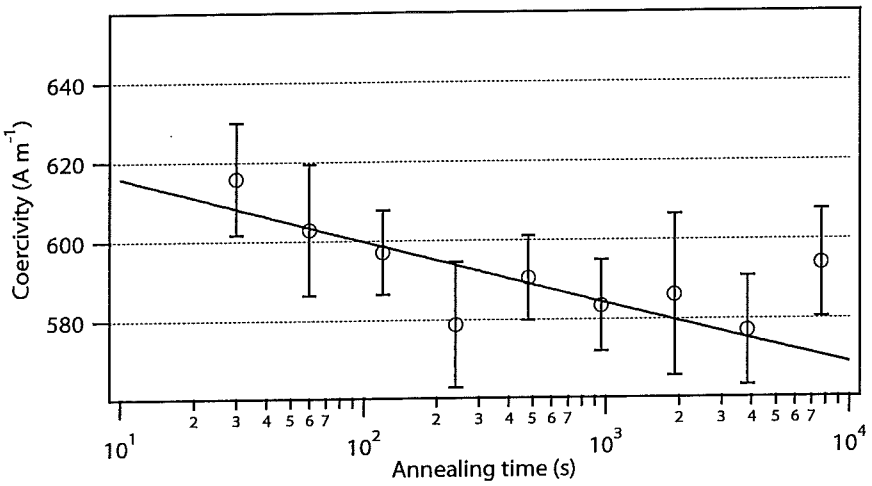

Figure 6.26: The coercivity of C-Mn steel as a function of the annealing time. The solid line shows the modelled coercivity from equation 6.2.

6.4 Discussion

With reference to subsection 2.5.1, the decision is made to use magnetisation instead of induction as parameter to describe the magnetic state of the material. The magnetic induction originates from an impression that magnetism is a current-like phenomenon and is still widely known as it is convenient to explain basic magnetism in this way. However, it does not describe the actual state of the material involved. Magnetisation, on the other hand, describes the material magnetic state as it is the sum of the atom magnetic moments, more specifically the component in the direction of the applied field, per unit of volume.

In obtaining the relation between the magnetisation curves and the dislocation density, three issues arose, which hindered a clear sight at this relation:

1. The determination of the dislocation density was indirect, especially for the C-Mn steel. Two methods were used, both based on hardness measurements. The two methods used yielded similar, although not identical, dislocation densities. The obtained dislocation densities did not seem to be unreasonable.

2. Applying a valid correction for demagnetisation appeared not to be possible for magnetisation curves that were obtained using VSM programme 1. For magnetisation curves that were obtained using VSM programme 2, a demagnetisation correction could be applied with lim-

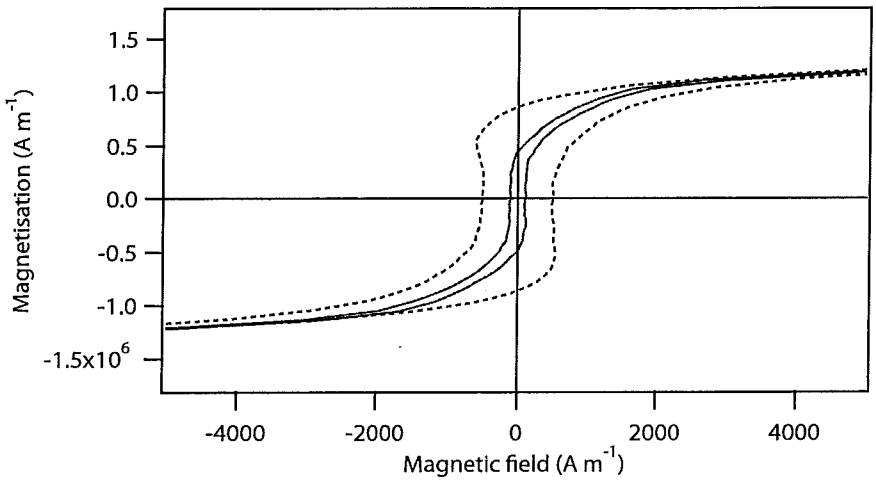

Figure 6.27: The magnetisation curves after demagnetisation correction for undeformed IF and C-Mn steel samples with $N_d \approx 0.082$. The solid red line shows the magnetisation curve for the IF steel and the dashed black line shows the magnetisation curve for the C-Mn steel.

ited accuracy. For the coercivity value, demagnetisation has no effect. The VSM programme used does not affect the obtained coercivity.

3. When applying several magnetisation cycles to the same sample, a significant scatter was revealed. This scatter leads to an extra uncertainty in the obtained relation. It also causes a reverse method, in which the dislocation density is determined using coercivity, to be less accurate.

Two materials have been used to investigate the effect of dislocations on the coercivity. For both materials, this effect appeared to be similar, as will be discussed in subsection 6.4.1. Figure 6.27 shows the magnetisation curves for undeformed samples of both materials. These curves have been corrected for demagnetisation. It can be seen that the magnetisation curves for the two materials are very different. This makes the observed effect of the dislocation density on the coercivity very interesting, since it appears to be valid for materials with different magnetic properties.

6.4.1 Coercivity

Since the coercivity is independent of demagnetisation, the determination of this parameter is also valid if no demagnetisation correction is applied. In relation to the dislocation density, for both materials used, a value for γ_D has

been determined:

$$\gamma_{D,C-Mn} = 4.8 \pm 0.9x10^{-6} \text{ A}$$

$$\gamma_{D,IF} = 4.9 \pm 1.4x10^{-6} \text{ A}$$

The similarity between the two values for γ_D indicate that this value is not accidental, but might well be valid for ferrite as part of various microstructures. A general value for γ_D would then be:

$$\gamma_D = 4.9 \pm 0.8x10^{-6} \text{ A}$$

There is a reasonable agreement between the coercivity and the stress-relaxation model, as shown in figures 6.17, 6.19 and 6.26. For this relation, no fitting parameters have been used. Both the coercivity and the stress-relaxation are theoretically related to the dislocation density assuming a random distribution of dislocations, in which the stress fields of the dislocations do not interact. Although the dislocation distribution has not been determined, it has been shown that the coercivity during recovery annealing can be modelled this way.

The derivation used to determine the relation between the dislocation density and the coercivity treats the dislocations as randomly distributed defects, which interact with the domain walls. However, it can be argued that the domain wall will not be affected significantly by a defect as small as a dislocation. The stress field generated by the dislocation is more likely to interact with the domain wall motion. From this, the correlation between the stress-relaxation and the coercivity is expected. Up to a certain limit, this may cause the correlation to be insensitive to changes in the dislocation distribution.

Principally, one fitting parameter has been used to fit the stress-relaxation model to the coercivity, being γ_D. However, this value has not been obtained from the data of the annealed samples, but from the undeformed and deformed samples. Using this γ_D, a good fit is obtained between the coercivity model and the data of the annealed samples. This shows that the obtained value for γ_D is valid. γ_D is determined using the assumption that the increase in coercivity is only caused by an increase in dislocation density. This shows that the increase in dislocation density is the only process in the material during deformation that significantly affects the coercivity.

γ_D has been shown to be the same for two different steel types. From this, the dislocation density can be determined from the coercivity if γ_0 is known. Since γ_0 is a complex consequence of all microstructure components other than dislocations, determining ρ_D using $\mathbf{H_c}$ needs to be done by comparing $\mathbf{H_c}$ to a sample with known ρ_D. $\Delta\rho_D$ can be determined with:

$$\Delta\rho_D = \gamma_D^{-2} \ (\Delta\mathbf{H_c})^2 \tag{6.3}$$

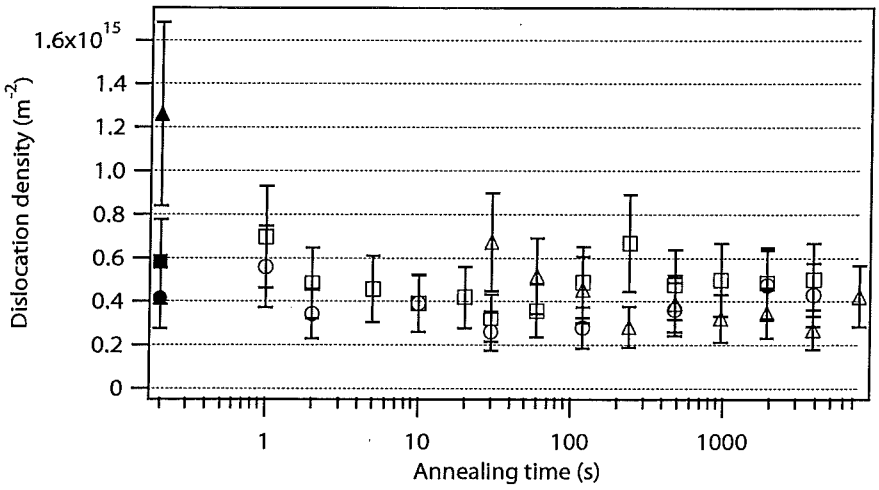

Figure 6.28: The dislocation density obtained from the coercivity using equation 6.3 as a function of annealing time. The circles represent the IF steel samples using a large step size, the squares represent the IF steel samples using a small step size and the triangles represent the C-Mn steel samples. The closed symbols represent the deformed state. The open symbols show the dislocation density after annealing at 400°C for the time indicated.

Figure 6.28 shows the dislocation density obtained from the coercivity using equation 6.3 as a function of annealing time for the two steel types used.

Information on γ_0 can be obtained from comparing samples in which other differences than the dislocation density are present. In this study, two materials were used, which gives rise to two different values for γ_0. From the assumption that $\rho_D = 0$ for the undeformed material, it follows that for these samples $\mathbf{H}_c = \gamma_0$:

$$\gamma_{0,C-Mn} = 510 \pm 12 \text{ A m}^{-1}$$

$$\gamma_{0,IF} = 120 \pm 15 \text{ A m}^{-1}$$

Here, $\gamma_{0,C-Mn}$ is determined in the rolling direction. Figure 6.24 shows that the magnetisation curves, and thus $\gamma_{0,C-Mn}$, depend on the direction of magnetisation.

The difference in γ_0 between the two steel types is caused by the difference in microstructure between the two materials. Two major differences are present in the microstructure. Firstly, the C-Mn steel has a finer grain structure than the IF steel. The coercivity is known to depend on the grain size d_g and most references use $\gamma_{d_g} \propto d_g^{-1}$ [36–40]. This mainly relates to the grain boundaries being domain nucleation sites. A higher grain boundary

density will lead to a higher domain wall density. Domain walls are considered to hinder each others motion, leading to a reduced domain wall motion and thus increased coercivity. Thus, the finer grain structure of the C-Mn steel will lead to a higher coercivity.

Secondly, pearlite is known to have a higher coercivity than ferrite, due to the presence of cementite [36] and the finer grain structure. Carbides such as cementite are considered to be very strong pinning points. As $\mathbf{M}_s$ in cementite is lower than in ferrite, free poles are present around the cementite. This causes small domains to exist around the cementite, which act as strong pinning points. As the coercivity can be approximated by a rule of mixtures [36], the presence of pearlite will increase the total coercivity of the C-Mn steel. These two differences contribute to the significant difference in γ_0 for the two materials.

Figure 6.28 shows that ρ_D, determined from $\mathbf{H}_c$, is not significantly different for the IF steel annealed for 64 min (3840 s) when compared to the other annealed IF steel samples. The EBSD results have shown that the dislocation density for this sample is significantly different than the sample annealed for 32 min (1920 s). It is likely that the finer grain structure of the 64 min annealed sample caused an increase in γ_0 of similar magnitude as the decrease in $\gamma_D\sqrt{\rho_D}$.

6.4.2 Remanence

For the magnetisation curves obtained with a small step size (VSM programme 1), no remanence values are shown. This relates to the issues that arose with applying a demagnetisation correction. The inaccuracy in this correction was such that the obtained remanence values did not relate to the material properties. Also, using remanence values without applying a demagnetisation correction does not give useful information, as these remanence values would be the direct consequence of the coercivity and the apparent demagnetising factor.

For the magnetisation curves obtained with a larger step size (VSM programme 2), a demagnetisation correction could be applied. However, it is important to note that despite this correction, the characteristics of the magnetisation curve still depend on the sample shape. This shows that the magnetisation curve and therefore also the remanence are still affected by demagnetisation. Also, some scatter is present in the determination of N_d, which causes an extra uncertainty in the results after correction.

From figure 6.20, a clear relation between the dislocation density and the remanence does not appear. The measured remanent magnetisation is 20 –

25% of the saturation magnetisation. For an undeformed C-Mn steel sample with the same shape, the measured normalised $\mathbf{M}_r$ in the rolling direction is 0.49. The remanence for the C-Mn steel is thus significantly higher than for the IF steel. In both cases, the true remanent magnetisation might be different, probably higher, due to demagnetisation effects that could not be corrected for.

One possible assumption would be that at zero field, all atom magnetic moments are directed in the easy axes, but no domains have formed. The normalised magnetisation that would be the consequence of this situation depends on the distribution of easy axes. It is most likely that for each part of the material, one orientation for the local magnetic moment is most favourable. So, there will be only one easy axis. However, it is possible that other orientations have only a slightly higher energy. In that case, the material can behave as having more than one easy axis. This could for instance be the situation when the anisotropy energy is mainly determined by contribution of the crystallographic anisotropy.

If the local easy axes are randomly distributed throughout the material, the normalised magnetisation would be 42% if there is one easy axis. With two, perpendicular, easy axes, this would be 83% and with three, perpendicular, easy axes, this would be 92%. Also, local minima in the anistropy energy can be present that have a significantly higher energy than the easy axes. These local minima may cause the magnetic moment to rotate towards this direction instead of the easy axis, if it passes such a local minimum when rotating from the forced direction to an easy axis. This is more likely to occur in materials with less easy axes.

The samples have been deformed using compression in the direction in which the magnetisation has been determined. It is likely that compressive residual stresses are present. For a low alloy steel, the magnetostriction is positive. Therefore, the easy axes will show a preference to directions in which tensile stresses are present. This will cause the easy axes not to be randomly distributed. For the situation described, the easy axes will show a preference to directions that have a small component in the measured direction. This will decrease the percentages mentioned. It will also be less likely that the material behaves as having more than one easy axis. This would cause an additional difference between the undeformed and deformed samples, which does not appear in figure 6.20.

From this, it can not be concluded if it is possible that rotation only causes the normalised magnetisation to decrease to the observed $\mathbf{M}_r$. From figure 6.14 it appears that a negative field is required to have domain wall motion, which is characterised by the high susceptibility. Therefore, the process of domain wall motion does not affect the remanence. Possibly, domain wall

nucleation does affect the remanence.

The relatively small grain size and pearlite presence in the C-Mn steel clearly affect the remanence, when compared to the IF steel. The remanence for the C-Mn steel is significantly higher than for the IF steel. From the coercivity and the microstructure, the C-Mn steel appears to have a higher pinning point density with stronger pinning points. These pinning points not only hinder domain wall motion, they also function as domain nucleation sites. From that, the C-Mn steel is expected to have a lower remanence if domain nucleation is the main process determining the remanence.

The high remanence for C-Mn steel shows that domain nucleation is not the main process determining the remanence. The insensitivity to dislocations, together with the high remanence values and the shape of the magnetisation curve show that domain wall motion is not the main process determining the remanence either. Therefore, domain rotation towards easy axes appears to be the main process determining the remanence.

For pearlite, the orientation of the plates will affect the anisotropy. Due to the shape anisotropy contribution, the easy axis will tend to be close to the rolling direction in the pearlite. Figure 6.24 shows that the remanence in the rolling direction is higher than in the other two main directions. This relates well to the conclusion that domain rotation is the main process in determining the remanence. In the rolling direction, this rotation will be less than in the other directions. Therefore, the decrease in magnetisation due to rotation will be less in this direction.

The magnetisation processes depend on the microstructure. It can therefore not be concluded that the relative contributions of domain rotation and domain nucleation to the remanence are the same for both IF and C-Mn steel.

The effects of dislocations on the magnetic properties are mainly due to the interaction of dislocations with domain wall motion. In principle, dislocations can act as domain nucleation sites, which is most likely for distributions in which regions of extremely high dislocation densities are present, such as cell structures. Since only a small deformation is applied, it is likely that the distribution will be more random. Therefore, it is not surprising that the dislocation density does not affect the remanence.

7. Magnetic Barkhausen Effect

The magnetisation process is discontinuous. This discontinuous magnetisation process is known as the magnetic Barkhausen Effect (MBE), see subsection 2.5.2, which is microstructure dependent. MBE experiments have been performed as described in section 4.6. This chapter discusses the results of these MBE experiments.

7.1 Barkhausen burst

Figure 7.1 shows the recording of a typical MBE burst and figure 7.2 shows the details of a small part of this burst. One burst represents a change in magnetisation from one endpoint of the magnetisation curve to the other. Ideally, this would be from magnetic saturation in one direction to magnetic saturation in the opposite direction. The actual magnetisation is not being recorded, therefore, it is not known whether saturation is achieved during the MBE experiments. However, the MBE activity in the centre of the burst is significantly higher than at the start and at the end, which indicates that the major change in magnetisation, accompanied with the process of domain wall motion, is covered in the experiment.

Figure 7.1 shows that an MBE burst recording consists of a large number of data points, which arise from the sampling of the voltage in the pick-up coil. These pulses can be both positive and negative. Both positive and negative MBE pulses can be related to a change in magnetisation in the same direction. This paradox is demonstrated by figure 7.3, showing that the important parameter of each MBE pulse is its absolute value. All analysis techniques use only the absolute values of the pulses.

The number of data points in one burst N depends on the set magnetising frequency f_M (number of magnetic hysteresis loops per second) and sampling frequency f_s:

$$N = \frac{f_s}{2f_M} \tag{7.1}$$

and is typically of the order of 10^4. This large number of data points potentially contains a huge amount of information.

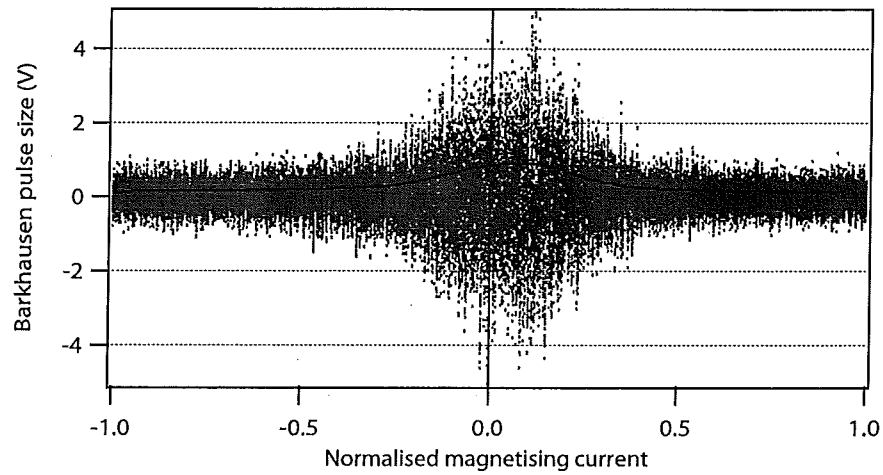

Figure 7.1: Recording of a typical MBE burst. The red dots show the data points sampled and the solid black line shows the running average of 4000 data points. The magnetising current on the x-axis is normalised to the maximum current.

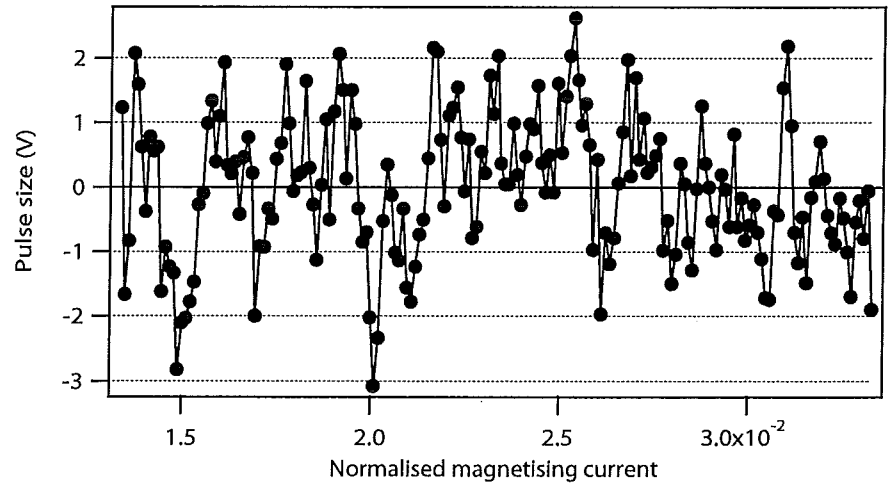

Figure 7.2: Small part of the same recording as shown in figure 7.1. The solid line is drawn from point to point. The magnetising current on the x-axis is normalised to the maximum current.

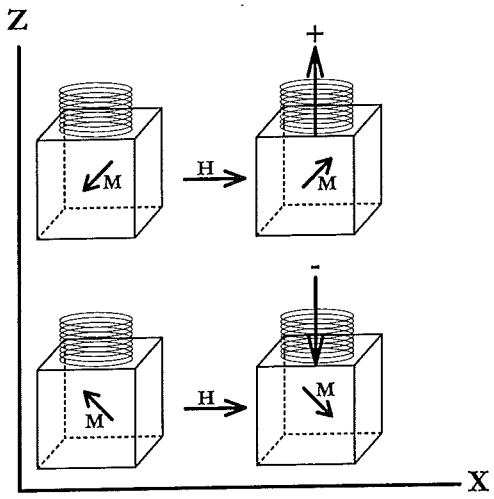

Figure 7.3: The observation of an MBE signal. The pick-up coil is placed on top of the sample and records a change in the Z-component of the magnetic induction. The sweeping applied field is directed in the X-direction. A hypothetical sample, consisting of one domain with one easy axis, is shown in the top left. After applying a magnetic field in positive X-direction, the magnetisation switches to the top right situation. This generates a positive MBE signal. Another sample, at the bottom left, will generate a negative signal when switching to the situation at the bottom right. In both cases, the change in magnetisation is positive with respect to the applied field.

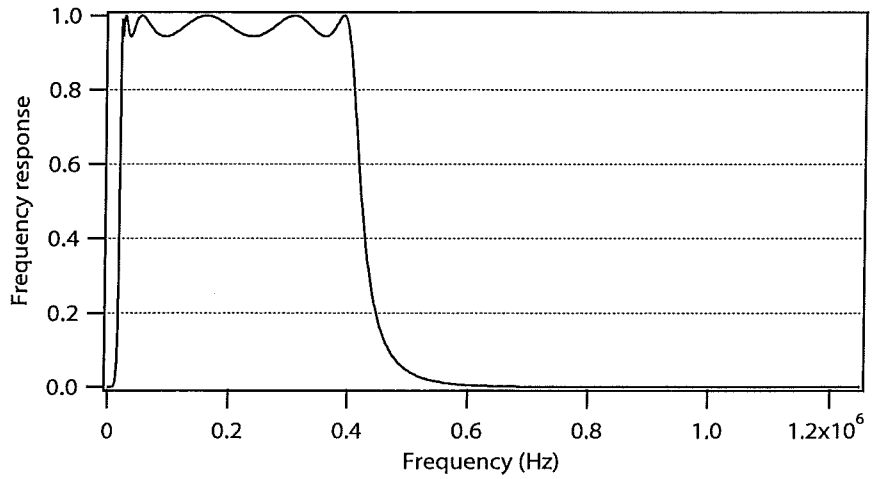

Figure 7.4: The frequency response of a digital Chebyshev type I filter, consisting of a 6^{th} order Chebyshev polynomial, a ripple factor of 0.5 and with a band pass of $20 - 400$ kHz.

The magnetic Barkhausen Effect is a chaotic phenomenon, causing natural scatter to occur. In order to obtain a signal that is less affected by coincidental effects, each experiment consists of eight bursts, created by applying four magnetisation cycles. Also, the positioning of the MBE sensor was not fixed. To obtain representative material properties, each experiment was repeated ten times.

The measured MBE burst is not free of noise, where noise can in this case be defined as magnetic signals that are not related to the discontinuous changes in magnetisation in the top layer of the material. This noise can for instance be caused by the magnetising coils or nearby electronic equipment. A large part of this noise can be filtered by use of a digital frequency filter. All the results shown have been filtered using a Chebyshev filter, consisting of a 6^{th} order Chebyshev polynomial, a ripple factor of 0.5 and with a band pass of $20 - 400$ kHz. Figure 7.4 shows the frequency response of this filter.

7.2 Magnetic Barkhausen analysis

The MBE experiments are performed to obtain a signal that represents the microstructure of the material, in this case related to the annealing time after deformation. To extract the relation between the annealing time and the MBE signal, changes in this signal with annealing time are to be observed. Such relations are most commonly being determined by plotting the obtained

results against the annealing time. As MBE bursts consist of a large number of data points, it is convenient to extract single parameters from each burst. Naturally, a single value can obtain less information than 10^4 data points, so information will be lost in this procedure.

Three means of MBE analysis that can be found regularly in the literature and produce one value per experiment will also be treated in this section:

1. Peak height
2. Peak position
3. Root-mean-square value (RMS)

Next to these, two analysis methods are investigated that try to compare the various MBE bursts in more detail. In the first one, the magnetisation process is split up into ten parts, which are analysed separately. In the second one, the changes in pulse size distributions are given. In section 7.4, an attempt is made to link the MBE data to the magnetisation curves obtained by VSM experiments.

7.2.1 Peak height

Figure 7.5 shows the peak height as a function of annealing time for IF steel. The MBE experiments are conducted on the same samples as have been used to create the VSM samples. Therefore, figure 7.5 is constructed similarly as the figures in section 6.2.

The peak height is determined from the running average as shown in figure 7.1 and is defined as the maximum value of this running average. Increasing the number of data points over which the running average is calculated reduced the scatter in the results. However, if this number is too high, the peak height does no longer represent the maximum MBE activity. As a compromise, the running average is taken over 4000 points.

The peak height increases significantly with deformation, which shows an increase of MBE activity in the region where MBE activity is at maximum. The peak height decreases slightly with annealing. The scatter and variation between samples is significant when compared to the effect of annealing time.

7.2.2 Peak position

Figure 7.6 shows the peak position as a function of annealing time. This peak position is defined as the magnetising current at which the peak value as used in figure 7.5 is achieved. A running average is taken from the 4000

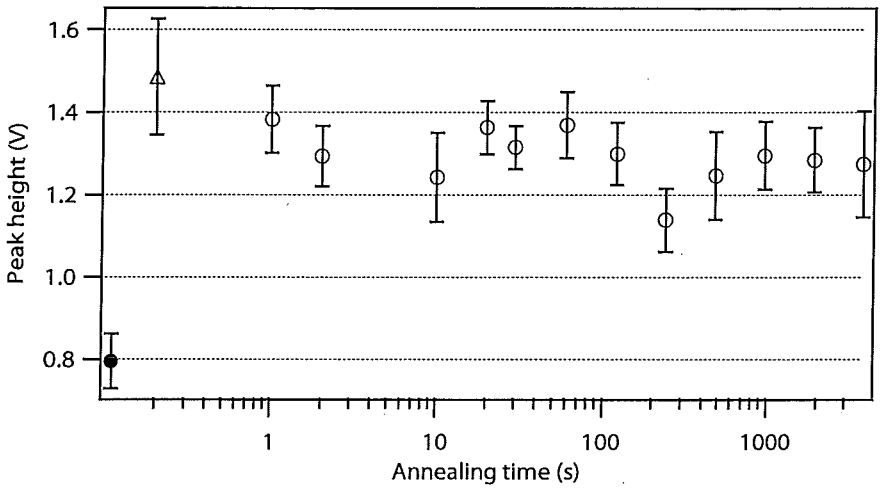

Figure 7.5: The peak height of IF steel as function of the annealing time. The closed circle at 0.11 s represents the undeformed state. The open triangle at 0.2 s represents the deformed state. The open circles show the peak height after annealing at 400°C for the time indicated.

data points preceding the point at which the average is given. To characterise the point with peak activity, this running average is shifted back 2000 data points on the time axis. In this way, the result shows the average for the 4000 data points surrounding the point at which the average is given. Thus, the peak position obtained is in the centre of the region with most MBE activity.

The number of data points used for the running average is such that the running average is very smooth, as seen in figure 7.1. In this way, the scatter is reduced. Figure 7.6 shows that the peak position is not affected by deformation and annealing.

7.2.3 Root-mean-square value

Figure 7.7 shows the RMS value as a function of annealing time. The RMS value is calculated using:

$$\mathrm{RMS} = \sqrt{\frac{1}{N}\sum_{i=1}^{N} S_i^2} \tag{7.2}$$

where N is the number MBE pulses i with pulse size S_i.

The RMS value increases with deformation and shows a slight decrease with annealing. This is a similar trend as the peak height. The peak height

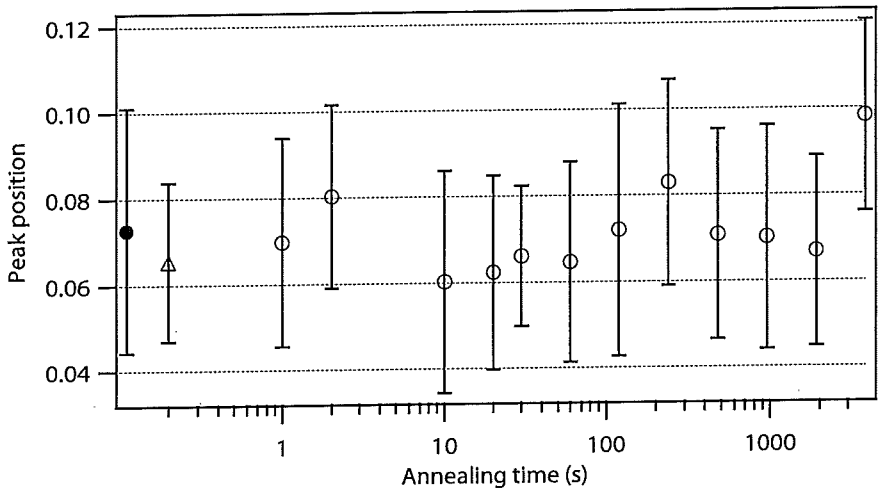

Figure 7.6: The peak position of IF steel as a function of the annealing time. The peak position is given as magnetising current, which is normalised to the maximum current as shown in figure 7.1. The closed circle at 0.11 s represents the undeformed state. The open triangle at 0.2 s represents the deformed state. The open circles show the peak position after annealing at 400°C for the time indicated.

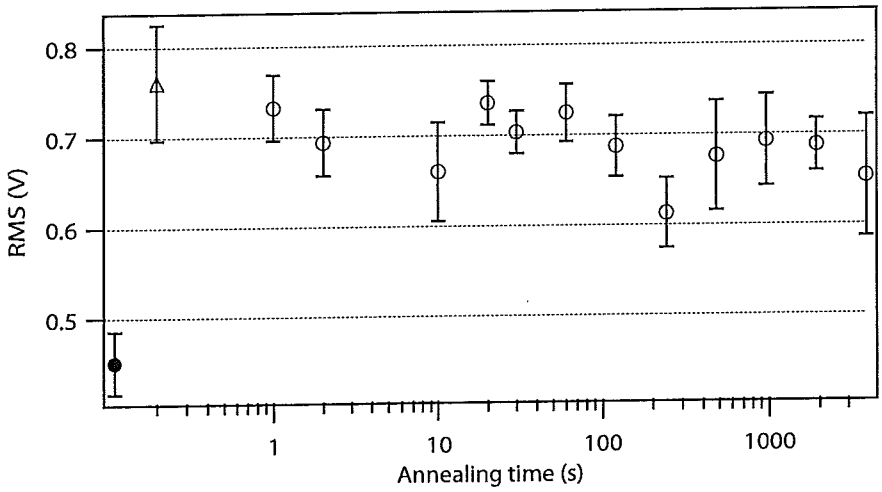

Figure 7.7: The RMS value of IF steel as a function of the annealing time. The closed circle at 0.11 s represents the undeformed state. The open triangle at 0.2 s represents the deformed state. The open circles show the RMS value after annealing at 400°C for the time indicated.

is determined by the MBE activity in only one part of the burst. The RMS is determined by the MBE activity in the whole burst. The part with maximum MBE activity has the largest effect on the RMS value. This part is the same part that determines the peak height. Therefore, the shown similarity is expected.

7.2.4 Splitting up the burst

Since the RMS value is mainly determined by the part of the MBE burst that has maximum activity, it does not give information on the MBE activity in the other parts of the burst. One way of obtaining more information on these parts is by determining RMS values for the various parts of the curve. For this, each burst is equally split up into ten parts, based on magnetising current, as shown in figure 7.8. For each part, the RMS values are determined and plotted as a function of annealing time in figure 7.9.

These figures show some interesting effects. In the central parts, where MBE activity is highest, deformation affects the RMS value significantly. This is similar to the total RMS value as presented in figure 7.7. This effect is not present at the start and end parts of the burst, parts I–II and VIII–X.

For the parts I–IV and VIII–X, the RMS value for the sample with annealing time 64 min is significantly lower than the other samples. This difference is not present in the central parts of the burst. This sample has been shown to have a different grain structure, with smaller grains than the other samples. Also, the EBSD results show a significantly lower dislocation density in this sample. Apparently, these differences in grain structure and dislocation density yield opposite contributions to the RMS value in the centre part of the burst, such a change in the RMS value is not observed. In the parts with lower MBE activity, a change in the RMS value is observed. This shows the value of splitting the burst into parts.

7.2.5 Pulse size distribution

Figure 7.10 shows the pulse size distribution for undeformed IF steel sample. This figure shows this pulse size distribution in three ways. Figure (A) shows the pulse size distribution on a linear scale. Figure (B) shows the same distribution on a logarithmic scale, indicating an approximately exponential decay in pulse count with pulse size. Figure (C) shows the contribution of this pulse size distribution to the RMS value ζ_j. ζ_j is defined as:

$$\zeta_j = \frac{1}{N} \sum_{i \in j} S_i^2 \tag{7.3}$$

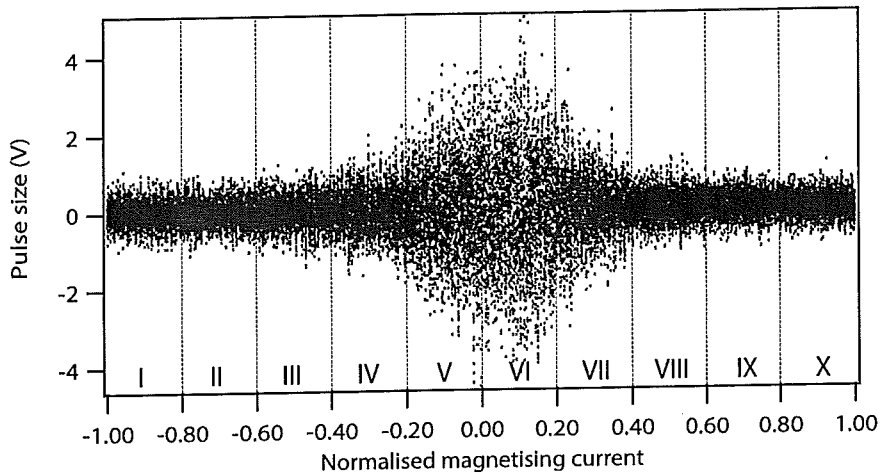

Figure 7.8: The same MBE burst as shown in figure 7.1, indicating the ten parts in which the burst is split up.

with N the total number of MBE pulses. S_i is the pulse size for the pulses i that are in range j as defined in the distribution figures. It appears that for the RMS value, a widely used parameter, the pulses in the range $0.2 - 2.0$ V have a much larger influence than the large pulses.

Figure 7.11 shows the difference in pulse size distribution between undeformed (a) and deformed (b) steel in three ways. Figure 7.11A shows the absolute difference ($b - a$). Figure 7.11B shows the relative difference ($\frac{b-a}{a}$). Figure 7.11C shows $\Delta\zeta_j$. From these figures it appears that at deformation, a general increase in pulse sizes is present.

Figure 7.12 shows $\Delta\zeta_j$ between the deformed and annealed IF steel for three annealing times:

(A) 10 s
(B) 32 min
(C) 64 min

Figures 7.12A and 7.12B look very similar. For both annealing times, a general small decrease in pulse sizes is present. Figure 7.12C is similar to figures 7.12A and 7.12B, apart from the pulses of size $0.5 - 1.5$ V. In this range, a significantly different change in the distribution is present.

Note the large error bars. These indicate that the scatter between individual bursts is significant. This is a consequence of MBE being a chaotic phenomenon. After averaging the bursts, the variation becomes much smaller than the scatter.

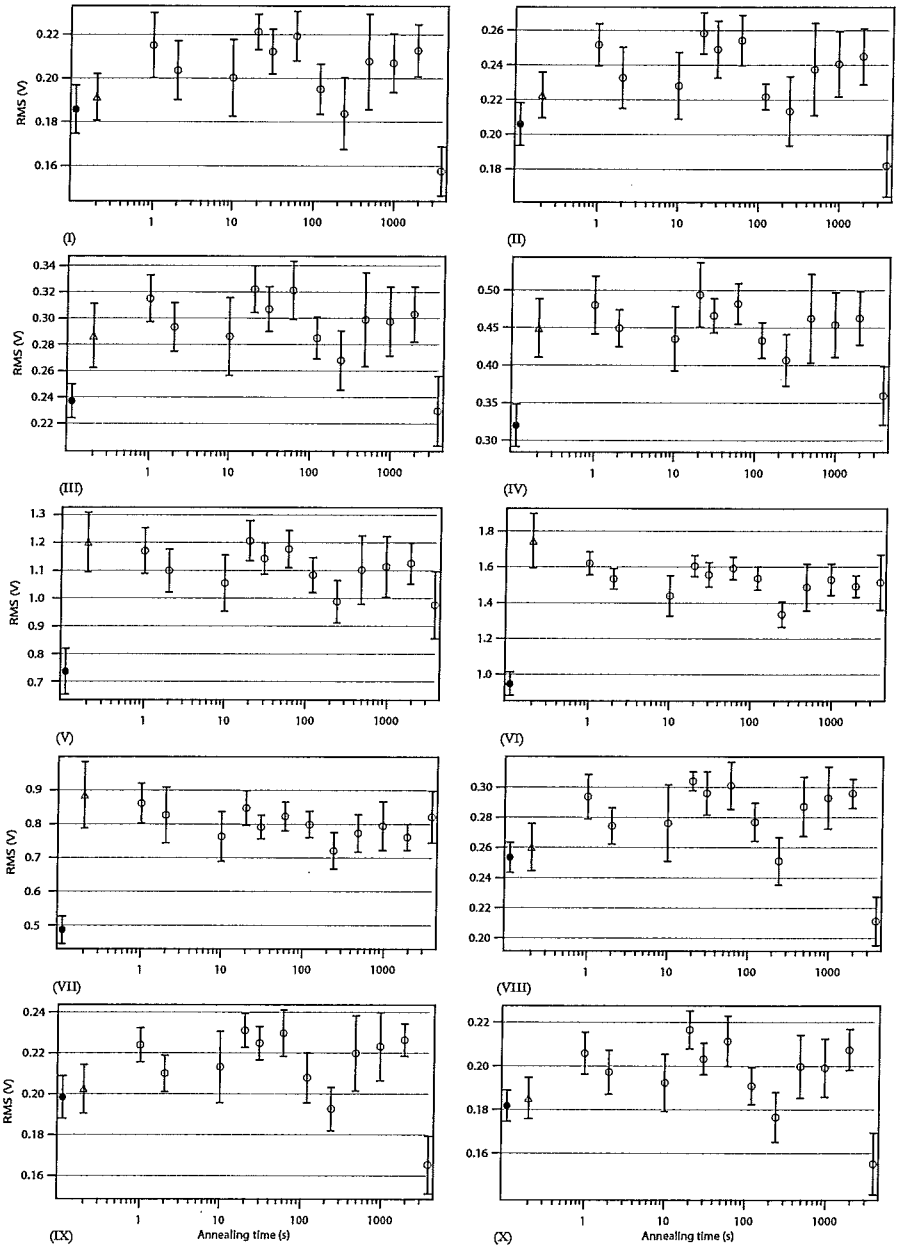

Figure 7.9: The RMS value of each part of the MBE burst of IF steel as a function of the annealing time. The closed circle at 0.11 s represents the undeformed state. The open triangle at 0.2 s represents the deformed state. The open circles show the RMS value after annealing at 400°C for the time indicated. The Roman number at the bottom left of each figure indicates the part of the burst.

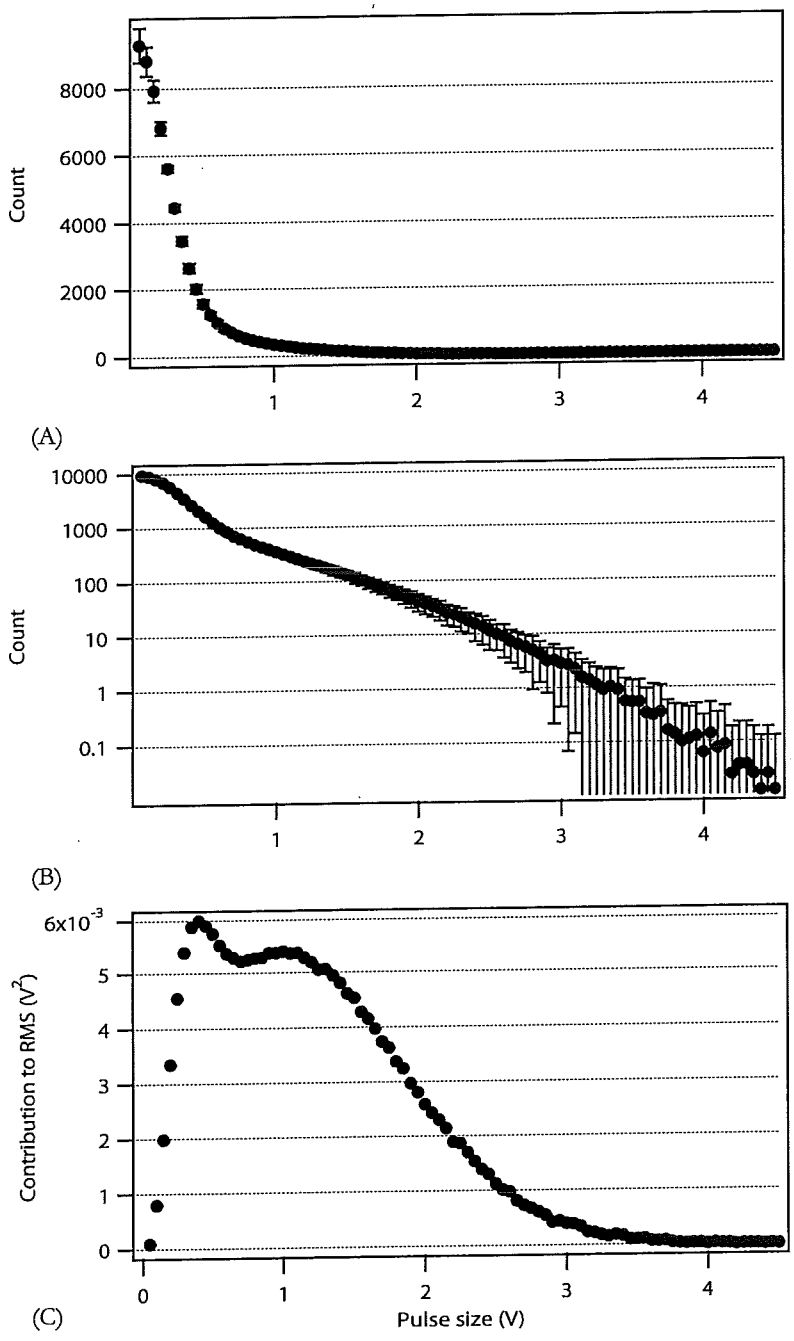

Figure 7.10: The pulse size distribution of undeformed IF steel on a linear scale (A), on a logarithmic scale (B) and its contribution to the RMS value ζ_j (C).

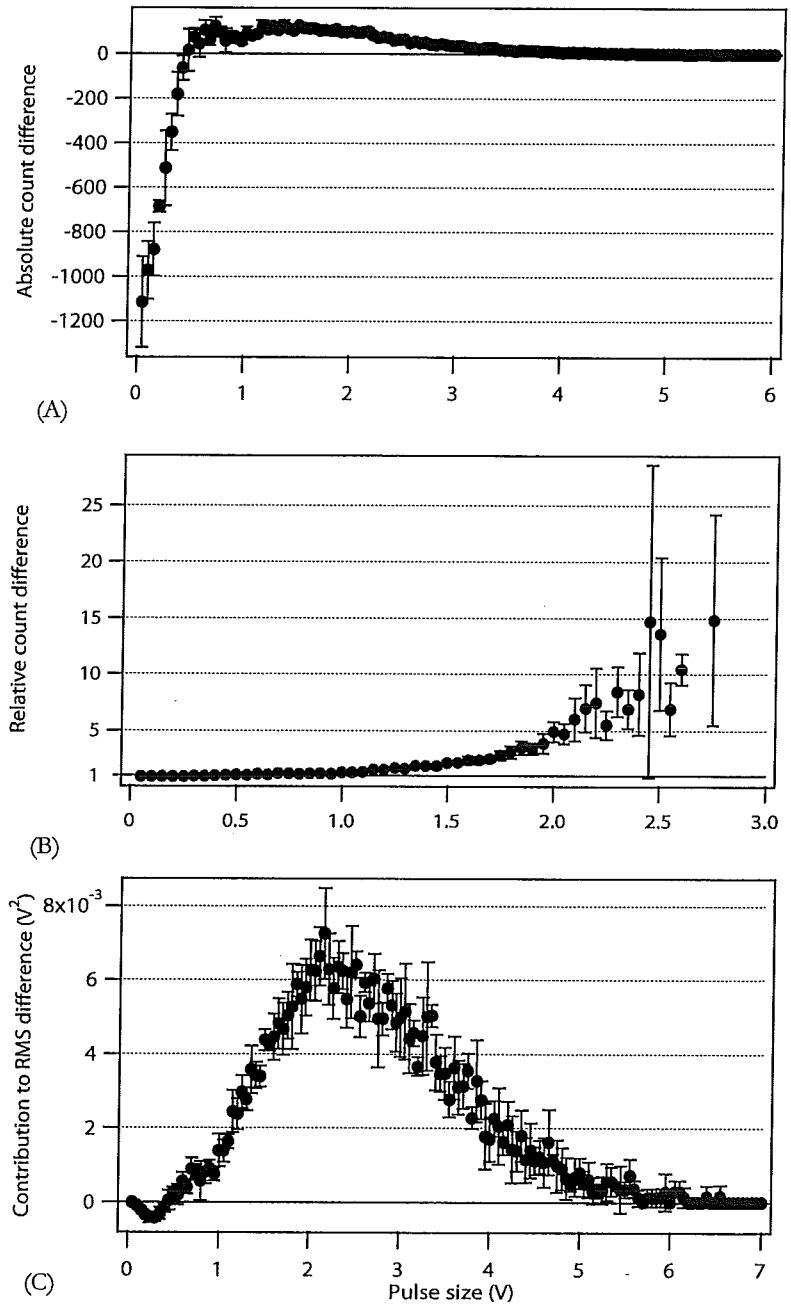

Figure 7.11: The difference between the pulse size distributions of undeformed and deformed IF steel. Figure (A) shows the absolute difference. Figure (B) shows the relative difference. Figure (C) shows $\Delta\zeta_j$.

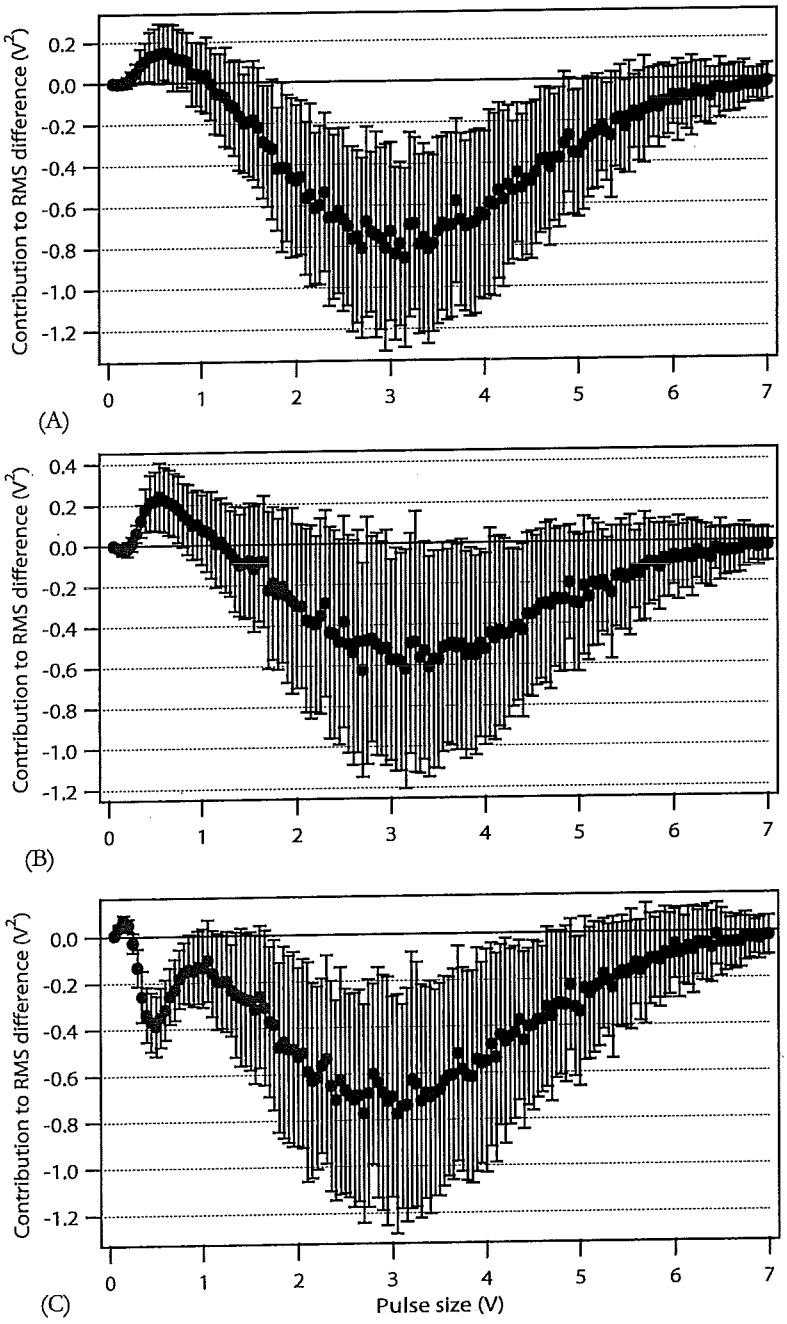

Figure 7.12: $\Delta\zeta_j$ between the deformed and annealed IF steel samples. The annealing times are 10 s (A), 32 min (B), and 64 min (C).

The notable fluctuation in figure 7.12C appears to be the consequence of an additional change in pulse size distribution. Apart from the primary change to smaller pulse sizes, an additional change is present, decreasing pulses from the $0.5 - 1.5$ V range to smaller pulse sizes. This additional change relates to a change in the MBE signal in the parts I–IV and VIII–X, which are the parts with lower MBE activity. This additional change affects the RMS value, causing the lower RMS value at 64 min in figures 7.9 I–IV and VIII–X. It appears therefore useful to compare the pulse size distributions in such a region with lower MBE activity.

Figure 7.13 shows $\Delta\zeta_j$ between deformed and annealed IF steel samples for parts. The annealing times and parts are:

(A) 32 min, part IV
(B) 64 min, part IV
(C) 64 min, part VI

Figure 7.13A does not show a significant change in distribution. In figure 7.13B a decrease in pulse sizes is clearly present. This decrease could be related to the combination of smaller grains and lower dislocation density as found for this sample. Figure 7.13C shows $\Delta\zeta$ for the same sample as figure 7.13B for part VI, where the MBE activity is much higher than for part IV. This shows that the additional change is indeed an effect occurring in the parts with lower MBE activity.

7.3 Comparison of IF and C-Mn steel

Figure 7.14 shows $\Delta\zeta_j$ for undeformed IF steel and C-Mn steel. The C-Mn steel shows a significant increase in pulse sizes compared to the IF steel. This shows that the MBE activity in the C-Mn steel is significantly higher than in the IF steel. As discussed in chapter 6, the pinning point density in the C-Mn steel is higher than in the IF steel, leading to a magnetically harder material. This effect is similar, but stronger, than for the increased dislocation density due to deformation. In both cases, a magnetically harder material has a higher MBE activity.

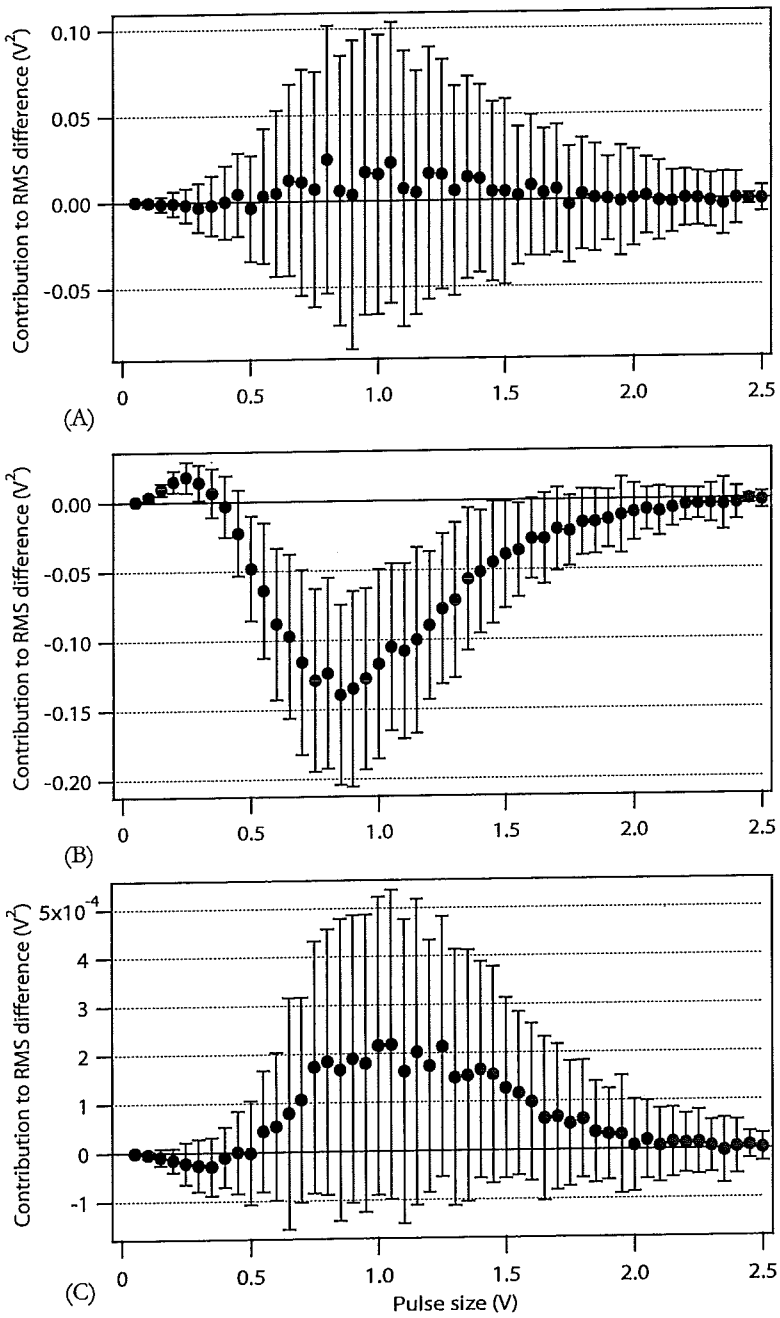

Figure 7.13: $\Delta\zeta_j$ for parts of the MBE burst between the deformed and annealed IF steel samples. The annealing times and parts are 32 min, part IV (A); 64 min, part IV (B); and 64 min, part VI (C).

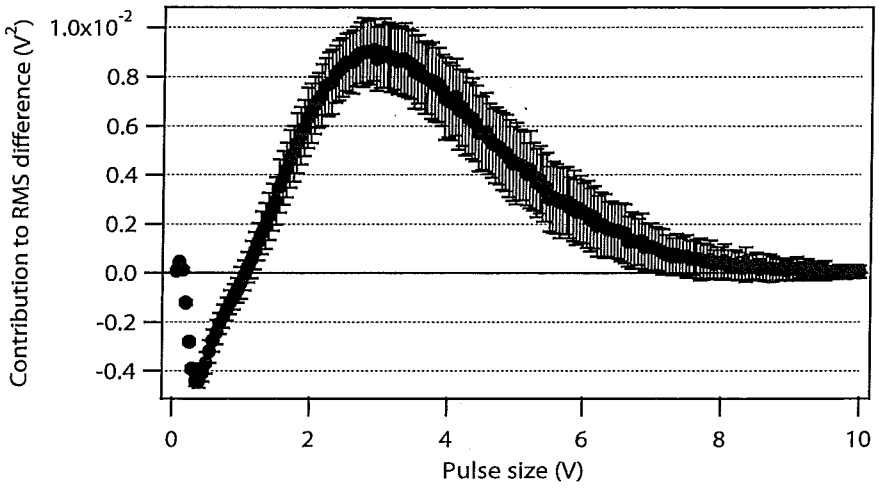

Figure 7.14: $\Delta\zeta_j$ for undeformed IF steel and C-Mn steel.

7.4 Comparison of magnetisation curve and MBE

7.4.1 Direct translation

When comparing the results from magnetisation curve (VSM) and MBE experiments, it appears that an increasing coercivity corresponds to a general increase in pulse sizes.

For a direct comparison between the VSM and MBE experiments, it would be optimal to translate the results of one experiment to the other. MBE pulses are generated by sudden changes in magnetisation and the pulse size is proportional to the change in magnetisation. So, each pulse can be considered as $S \propto \frac{dM}{dt} \propto \frac{dM}{dH}$, and thus the integral would be proportional the total change in $\mathbf{M}$. However, since changes in the microstructure tend to either increase or decrease the pulse sizes, the total sum of the pulses changes significantly. Since $\mathbf{M_s}$ is expected to be constant, it is clear that this translation from MBE to VSM does not work. The way in which the MBE pulses are generated and recorded creates several potential causes for this failure in translation:

- As described in section 7.1, the applied magnetic field changes in the X-direction, while the MBE pulses recorded are created by changes in the Z-component of the magnetisation change. So, the $d\mathbf{M}$ assumed from the pulse size is actually $d\mathbf{M_z}$. This has two important consequences:
  - The relation between $d\mathbf{M_x}$ and $d\mathbf{M_z}$ depends on the orientations of the easy axes. Therefore, the relation between the observed

MBE pulse and the change in magnetisation due to the applied field depends on the orientations of the easy axes as well. Both changes in texture and stresses can change the orientations of the easy axes.

- Each observed pulse is the consequence of all the magnetic activity at that particular moment. If magnetic activity is present at different places at the same moment, they will contribute to the same observed pulse. Also, pulses can partly overlap. Since the Z-component of the magnetisation change is being recorded, the $\frac{dM}{dt}$ assumed from the pulse size is actually

$$\frac{d\mathbf{M}_z}{dt} = \sum_i \frac{d\mathbf{M}_{i,z}}{dt} \tag{7.4}$$

where $d\mathbf{M}_{i,z}$ is the Z-component of $d\mathbf{M}_i$. Since the Z-component of $d\mathbf{M}_i$ can be either negative or positive with respect to voltage generated in the pick-up coil, the various $d\mathbf{M}_{i,z}$ contributions in equation 7.4 can be either positive or negative. This means that $d\mathbf{M}_i$, and thus $d\mathbf{M}$ can not be constructed from the observed $d\mathbf{M}_z$. This effect is likely to have consequences of similar magnitude for all samples. Note that the extra effect of both positive and negative contributions only apply if they contribute to the same pulse, as for each pulse the absolute value is used.

- From figure 7.2 it appears that the sampling rate is such that the MBE pulses are not fully characterised. To do so, several sampled data points per pulse are necessary. If the sampling rate is insufficient, the pulses may not be correctly characterised, causing the obtained data to be different from the $\frac{dM}{dt}$ assumed. According to McClure and Schroder [41], the typical MBE pulse length is 10 μs, which would make the used sampling frequency of 2.5 MHz sufficient. Possibly, the observation is primarily due to partly overlapping pulses.

- The applied field during the MBE experiment is unknown. This causes uncertainty in whether or not saturation is achieved. Therefore, it is possible that the lower total pulse sum is caused by not achieving saturation, which would disable use of the assumption that saturation is achieved. The consequence would be that the samples with higher MBE activity reach saturation easier, since they would have a larger change in magnetisation with the same field change. This is contrary to what is expected from domain wall pinning theory.

- The applied field during the MBE experiment is not uniform. It is therefore necessarily different from the applied field during VSM experiments. This will generate an extra error in comparing magnetisation data from both experiments.

Apart from these causes created by the experiment, an important potential cause can be found in the material. Previously, it has been suggested that the whole magnetisation process is stepwise, causing MBE. However, this is not a proven fact. It might well be that part of the magnetisation process is in a more smooth way. For this part of the magnetisation $\frac{dM}{dt}$ is low and constant.

The MBE equipment is claimed to require a threshold value for $\frac{dM}{dt}$ to record the pulse size. Also, if $\frac{dM}{dt}$ is constant, it will be screened more effectively by eddy currents. This would cause the MBE sensor not to record the smooth part of the magnetisation. Therefore, a sample with lower MBE activity would point at a smoother magnetisation process, which would indicate a lower pinning point density. A lower pinning point density would cause a material to be magnetically softer, which would explain the observation that increased MBE activity corresponds to increased coercivity and remanence. Also, smooth changes in magnetisation due to rotation to an easy axis may not be recorded.

7.4.2 Comparing results

Although a direct translation from the MBE data to a magnetisation loop has not been successful, the obtained results can still be compared. If the running average is still considered as a derivative of the magnetisation curve, despite the issues discussed in subsection 7.4.1, this would lead to a potential similarity between the peak position and the coercivity. The peak position is the field at which the susceptibility is maximum, which is generally the coercive field. Figure 7.15 combines the results from figure 6.16 (coercivity) and figure 7.6 (peak position). The supposed similarity is not present.

At first sight, it seems that the peak height and RMS value behave similarly as the coercivity. This relates to the observation that the pulses sizes are larger for magnetically harder materials. Figure 7.16 combines figures 7.7 (RMS) and 6.16 (coercivity), showing that an increased RMS value indeed relates to an increased coercivity. The small variations during recovery are not similar for both techniques. This shows that these variations are a consequence of scatter and not of subtle effects in the recovery process.

Additional data analysis, in which the MBE burst was split up into ten equal parts, showed that extra information can be obtained from these parts of the

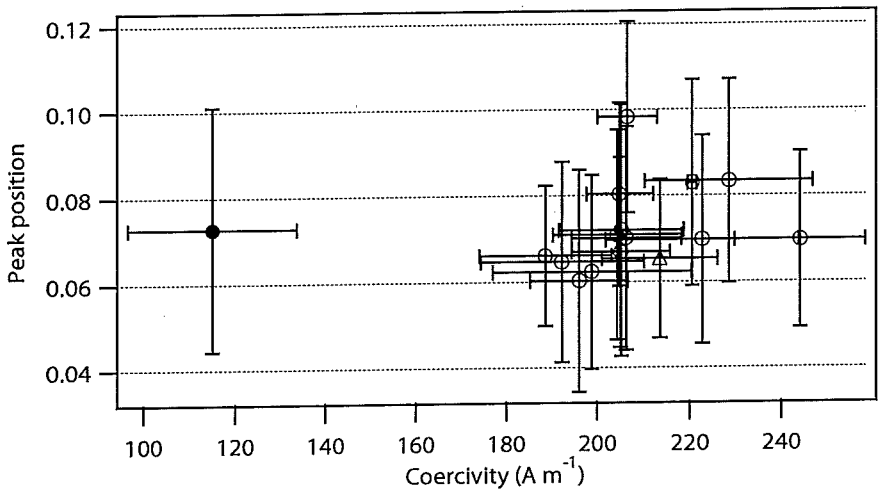

Figure 7.15: MBE peak position as a function of coercivity, obtained from VSM experiments, for various IF steel samples. The closed circle represents the undeformed state. The open triangle represents the deformed state. The open circles represent the samples that have been annealed at 400°C for various times. All these samples are the same as have been discussed in chapters 6 and 7.

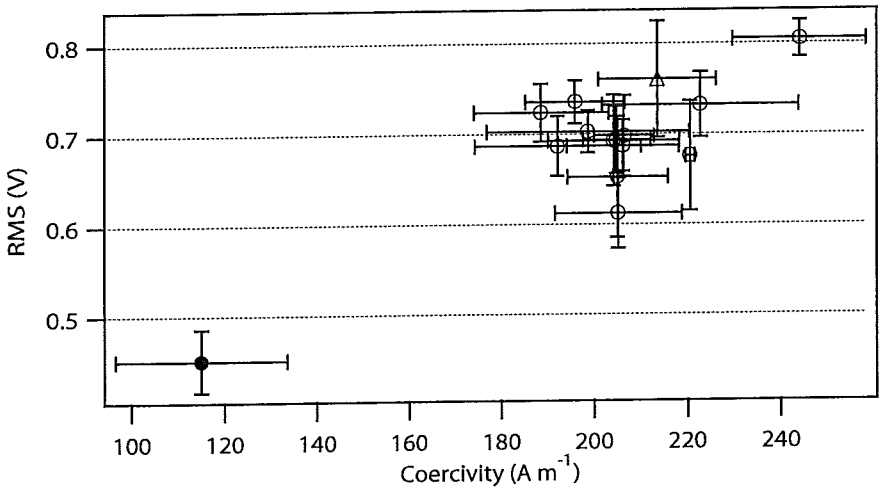

Figure 7.16: MBE RMS value as a function of coercivity, obtained from VSM experiments, for various IF steel samples. The closed circle represents the undeformed state. The open triangle represents the deformed state. The open circles represent the samples that have been annealed at 400°C for various times. All these samples are the same as have been discussed in chapters 6 and 7.

bursts. When changes occur in the parts of the burst that have relatively low MBE activity, they will not cause parameters that reflect the overall MBE activity to change significantly.

Parts I–IV and VIII–X showed a significant difference for the 64 min annealed sample, when compared to the other annealed samples. This difference did not appear in the parts V–VII or in the parameters describing the overall burst characteristics. The EBSD results showed a significant difference in grain structure and dislocation density between the 32 min and 64 min annealed samples. The observed differences in the MBE signal might relate to these microstructure differences. This difference has not been observed in the magnetisation curve experiments. The time frame of this study did not allow for successive experiments to characterise these effects in more detail.

8. Conclusions

8.1 Magnetisation curve

The obtained magnetisation curves from VSM experiments are affected significantly by a demagnetising field. To obtain the true magnetisation curves, these experimentally obtained curves have been corrected for demagnetisation. To apply this correction, knowledge on the demagnetising factor is required. It appeared that the sensitivity of the correction to the value of this demagnetising factor is very high. This high sensitivity is a consequence of $\mathbf{M} >> \mathbf{H}$.

Several options are available to determine the demagnetising factor N_d. The best results have been obtained by applying

$$N_d = \left(\frac{d\mathbf{H}_a}{d\mathbf{M}}\right)_{H_a \to 0} \tag{8.1}$$

to the magnetisation data for $|\mathbf{H}_a| < 8$ kA m^{-1}. A systematic error is introduced by using $|\mathbf{H}_a| > 0$ A m^{-1}, so it is best to have $|\mathbf{H}_a|$ as small as possible for this purpose.

With any experimental technique, the obtained data is subject to scatter, which is more significant for low values of measured quantity. For the determination of N_d, data points at low fields, with low material magnetisation, are used. The scatter present is significant and causes an extra error in the demagnetisation correction. Therefore, a large number of data points is preferred to enable a good estimation of N_d, such that scatter in individual data points do not significantly affect the outcome. However, the VSM equipment shows some instability when operating in low field regions for longer times. Therefore, a small number of data points is better. The compromise is found in this work.

From the magnetic properties, the coercivity has the advantage that it is insensitive to demagnetisation. The observed coercivity is also independent of the step size used. The change in coercivity during recovery can be modelled using the stress-relaxation model. Without using any fitting parameter, this model shows a good fit to the measured coercivity. This shows that the

increase in coercivity at deformation can be fully attributed to the increase in dislocation density.

It appears that the contribution of dislocations to the increased yield stress is similar to the contribution of the dislocations to the coercivity. Assuming a random dislocation distribution, the following relation has been found for the coercivity and the dislocation density:

$$\mathbf{H}_c = \gamma_0 + \gamma_D \sqrt{\rho_D} \tag{8.2}$$

with

$$\gamma_D = 4.9 \pm 0.8\text{x}10^{-6} \text{ A}$$

γ_0 depends on contributions from all other microstructure components. This value for γ_D has been shown to be valid for ferrite as part of various microstructures at room temperature. Using equation 8.2, it is possible to correct coercivity data for the dislocation contribution. This is a first step in determining the various microstructure contributions to $\mathbf{H}_c$.

The obtained results can also be used to determine the dislocation density from the coercivity. Due to the presence of the unknown γ_0, only the difference in ρ_D can be obtained from $\Delta\mathbf{H}_c$. $\Delta\rho_D$ can be determined from $\Delta\mathbf{H}_c$ using:

$$\Delta\rho_D = \gamma_D^{-2} \ (\Delta\mathbf{H}_c)^2 \tag{8.3}$$

For γ_0, two different values have been obtained for the two materials. From the assumption that $\rho_D = 0$ for the undeformed material, it follows that for these samples $\mathbf{H}_c = \gamma_0$:

$$\gamma_{0,\text{C-Mn}} = 510 \pm 12 \text{ A m}^{-1}$$

$$\gamma_{0,\text{IF}} = 120 \pm 15 \text{ A m}^{-1}$$

This difference is caused by the difference in microstructure between the two materials. The C-Mn steel has a finer grain structure than the IF steel, which will lead to a higher coercivity for the C-Mn steel. Also, pearlite is present in the C-Mn steel. Pearlite is known to have a higher coercivity than ferrite, due to the presence of carbides and the finer grain structure. These two differences contribute to the significant difference in γ_0 for the two materials. Since the coercivity is only one parameter, it does not distinguish between the different contributions. This may lead to erroneous estimations of ρ_D if γ_0 is not constant, as has been found with the IF steel experiments.

While the coercivity is largely determined by the domain wall motion process, this is not necessarily the case for the remanence. Depending on the material, the remanence can be determined by domain rotation, domain nucleation and domain wall motion. For the materials used, it appeared that

domain rotation is the main process determining the remanence. Since the effect of dislocations on the magnetic properties is mainly due to the interaction of dislocations with domain wall motion, changes in dislocation density do not have a significant effect on the remanence. This has also been shown in the experimental results.

8.2 Magnetic Barkhausen effect

The magnetic Barkhausen effect is a very complex phenomenon. It is closely related to the microstructure since it directly reflects the discontinuous magnetisation process. Therefore, it has great potential in providing understanding on the magnetisation process. However, it tends to cover its potential with its complexity. This nature of this complexity can be divided into three parts:

1. Generating the magnetic Barkhausen effect
2. Recording the magnetic Barkhausen effect
3. Translating the magnetic Barkhausen effect to the magnetisation process

Item three is the difficult and necessary step in unleashing the potential of the magnetic Barkhausen effect. Imperfections in items one and two make this translation even more difficult.

For this study, the main purpose was to gain initial understanding about this complexity. Therefore, MBE equipment has been used that is available at SKF in Nieuwegein. This equipment consists of a sensor that both generates and records the MBE signal. The focus of this study was aimed at translating the magnetic Barkhausen effect to the magnetisation process.

Various analysis methods have been applied to the obtained MBE data. The peak height and RMS value showed an increase with deformation and slight decrease with recovery annealing. Both parameters were affected similarly as the coercivity. The variation between the samples was not the same, showing that this variation is the effect of experimental scatter. The peak position is commonly related to the coercivity, but this relation did not appear from the results.

By focussing on specific parts of the MBE burst, additional information can be obtained that is not revealed by standard analysis methods. The obtained MBE results indicate that the data in parts with low MBE activity is affected by the microstructure in a different way then the parts with high MBE

activity, which dominate the standard analysis methods. Combining information obtained in both ways can enable distinguishing between contributions of different microstructure elements.

It is interesting to have a more detailed look at the pulse size distribution and at different parts of the burst. These form a step in between the standard analysis and the full-detail plot of the burst and can provide additional understanding on the magnetisation process. A translation from the magnetic Barkhausen effect to the magnetisation process was not successful.

The MBE equipment used was mainly designed for non-destructive evaluation (NDE) purpose. Therefore, it is not well suitable for a more scientific approach. The recording part was not optimal, especially recording the Z-component of the magnetisation changes, although it was probably sufficient to gain an improved understanding. The generating part was insufficient to enable the translation step. The applied field was different from the applied field used in the VSM equipment. It was also not uniform and the field strength was unknown. It was applied with a frequency that is several orders of magnitude higher than in the VSM. This high frequency leads to overlapping pulses. In combination with the recording technique, in which a perpendicular component of the magnetisation changes was observed, this disables the translation from observed pulses to the magnetisation process. Despite of these issues, MBE still has a high potential. Section 9.2 discusses ways to improve the generating and recording parts, in order to improve the translation part.

Although a direct translation from MBE to the magnetisation process is not possible, it appears that an increased coercivity, and thus a magnetically harder material, correlates with a higher MBE activity. This change is mainly facilitated by the change in dislocation structure. Apparently, the dislocation structure is such that it facilitates domain wall pinning, such that a larger part of the magnetisation process is discontinuous. This may lead to two distinct conclusions:

1. In a structure with randomly distributed dislocations, these dislocations form pinning points of sufficient strength to facilitate a discontinuous magnetisation process.

2. The dislocation structure after deformation is not a randomly distributed one. As the increased yield stress and the increased coercivity are both caused by the stress fields generated by the dislocations, the relation between these two measured parameters can be considered independent of the dislocation structure up to some extent.

Apart from a scientific approach to improve understanding of the magnetisation process, MBE experiments can also be conducted as non-destructive microstructure evaluation technique. The design of the MBE equipment used mainly aimed at this purpose. It has the advantage that sample preparation is less destructive than for the VSM experiments. Destructive elements in sample preparation make the difference between true NDE and limited NDE techniques, such as specifically the VSM experiments. Also, MBE experiments are less time consuming than magnetisation curve experiments with the VSM. Performing one MBE experiment is a matter of seconds, while a VSM experiment takes in the order of one hour. On the other hand, the magnetisation curves probe the bulk of the sample, while the MBE technique is limited to probing the surface.

Both experimental techniques suffer from a significant amount of scatter. This scatter was such that it troubles the sight on a subtle process as dislocation recovery. The effect of deformation can be clearly seen. The pulse size distribution figures show that averaging a number of MBE experiments significantly improves the obtained image. The MBE experiments gain more detailed information than the magnetisation curve experiments, which can be revealed by using various analysis techniques. This enables a better distinction between effects of different microstructure elements, which is clearly indicated for two annealed IF steel samples. EBSD experiments showed clear differences between the two samples, while the magnetisation curve experiments did not reveal these differences. MBE experiments indicated different behaviour for the two samples in different parts of the burst.

9. Recommendations

9.1 Magnetisation curve

When determining the magnetisation curve for a sample, the demagnetising field is the main issue to deal with. For a good correction, the demagnetising factor needs to be known very accurately. Determining the demagnetising factor this accurately is not easy. The correction that can be made using the best estimate of the demagnetising factor available does not make the magnetisation curves shape independent. This shows that a simple correction using one demagnetising factor for the whole magnetisation curve does not correct for all demagnetising effects present.

The coercivity is insensitive to demagnetisation and can therefore be determined despite these issues. It has been shown that using the coercivity, information on the dislocation density can be obtained. Similarly, the coercivity can give information on other microstructure parameters. However, the coercivity is only one parameter and using coercivity only therefore limits the possibility of microstructure evaluation. Therefore, it is worthwhile focussing on the demagnetisation effect.

Obtaining the demagnetising factor from the magnetisation data appears the best determination available. For this, it is important to have magnetisation data that shows little scatter. The VSM equipment used in this study requires a compromise between gaining sufficient data points and the limited stability at low fields for longer times in order to minimise scatter.

Another way to minimise scatter is by using larger samples. Larger samples will have a larger magnetic moment at the same magnetisation. The relative accuracy of determining a larger magnetic moment is generally better. The current VSM set-up does not allow for samples longer than 3 mm, which means that a larger diameter is the only way to have larger samples. A larger diameter with the same length gives a smaller aspect ratio, resulting in a larger demagnetising factor. Also the part of the shape dependency that is not corrected for with a standard demagnetisation correction is larger for smaller aspect ratios. Lake Shore VSM equipment is available that allows for samples up to a length of 25 mm.

For the coercivity, a proportional relation with the square root of the dis-

location density has been determined. This is a very useful relation and it is particularly interesting to see if this relation is valid also for other circumstances. Obtaining more complex dislocation structures and using steel alloys with different magnetostriction can give extra understanding in this matter. It is also useful to determine whether this relation is valid at higher strains, for steels with different microstructures and with different deformation mode.

From the relation between magnetic properties and the dislocation structure, both the contribution of dislocations to the coercivity and improved understanding of the magnetisation process are obtained. From this, the next step can be taken in the development of a microstructure characterisation technique based on magnetic properties. One can think of grain structure in single phase ferrite steel or phase distribution in dual phase steel. A very interesting application would be for TRIP steels. For these steels, the saturation magnetisation is already being used to determine the amount of austenite in the material. Eventually, it should be possible to use the same magnetic experiment to determine austenite distribution.

This further development of the magnetisation curve as microstructure evaluation technique will be more successful if more parameters from the magnetisation curve can be used. To be able to do this successfully, the demagnetisation correction needs to be excellent. This shows the importance of studying the demagnetising effects that occur, such that the demagnetisation correction can be improved.

9.2 MBE

Using the magnetic Barkhausen effect for microstructure evaluation has a high potential, provided that the results can be related to the magnetisation process, such that they can improve understanding about this process. Therefore, the experimental set-up needs to be adapted to cope with the issues as described in sections 7.4 and 8.2.

The issue that is noted in section 8.2 as most important to work on is generating MBE. Improving this is to be done by changing the way the magnetic field is applied to the sample. It is optimal to apply a uniform magnetic field and required to know the strength and direction of the applied field. To determine the effective magnetic field, the demagnetising field as a function of the applied field needs to be known. For this, the demagnetising factor and magnetisation curve need to be accurately known. To obtain this knowledge, VSM experiments should be executed on the same samples.

To have the MBE signal reflecting the magnetisation process, it is important to enable separate recording of different discontinuous magnetisation

changes. In that way, each observed MBE pulse represents one step in the magnetisation process. In the used set-up, this was disabled by the quickly changing applied field. Improvement is possible using a slowly changing magnetic field, such that the time between the steps is increased. A detailed investigation of the pulse generation as a function of magnetising frequency would be a useful study.

Apart from MBE generation, improving MBE recording will also enable a better understanding of the magnetisation process. A major improvement in MBE recording can be obtained by using a sensor that records the magnetisation changes in the same direction as the applied field. This way, the pulse size and direction directly relate to the magnetisation curve. Since the sensor is a pick-up coil that records the discontinuous field changes in the direction of the coil axis, this axis should be in the direction of the applied field. Therefore, a pick-up coil wound around the sample is to be used instead of a pick-up coil that is vertically pressed onto the surface. Also, the electronics used should be capable of sampling in a sufficient frequency to fully characterise the pulses.

Considering the above, a possible solution appears to be a combination of VSM and MBE experiments, in which the MBE pick-up coil is integrated in the VSM sample holder. This way, the magnetic field is undoubtedly the same for both experiments and also known and uniform. Also, the VSM is capable of producing a low-frequency full magnetisation loop. Performing the two experiments simultaneously is not recommended, as the vibration needed for the VSM experiment can affect the MBE signal recording. Also, the VSM experiment is best executed in a step-wise mode, while for the MBE experiment a constantly sweeping field is probably preferred. Although it can be interesting to investigate the MBE generation in a step-wise mode versus a constant sweep mode.

Some major improvements can be made in generating and recording MBE, resulting in a better translation the magnetisation process and thus understanding of this process. It is important to realise that perfection in MBE generation and recording is not easily achieved and translation will remain challenging. McClure and Schroder [41] discussed a number of issues, which are important to consider in designing MBE equipment and analysing the MBE signal.

The pulse signal as observed with the pick-up coil mainly depends on three parameters: the flux change at the pick-up coil ($\Delta\Phi_c$), the time constant of the flux change (τ_Φ) and the time constant of the pick-up coil (τ_c). Ideally, one would like to determine $\Delta\Phi_c$ and τ_Φ as they relate to the magnetisation process. To enable this, the pick-up coil needs to be designed such that

$\tau_c << \tau_\Phi$. In this case, the obtained voltage signal S would become:

$$S(t) = \frac{N_c \, \Delta\Phi_c}{\tau_\Phi} \left(\exp\left(-\frac{t}{\tau_\Phi}\right) - \exp\left(-\frac{t}{\tau_c \, (1-k^2)}\right)\right) \qquad (9.1)$$

where k varies between 0 and 1, for a pick-up coil that is respectively loosely and tightly wound around the sample.

Since $\tau_c \propto L$, where L is the inductance of the pick-up coil, L should be as small as possible. Since $L \propto \frac{N_c^2}{l_c}$, where N_c is the number of turns and l_c the length of the pick-up coil, N_c should be as small as possible. However, the obtained voltage signal $S \propto \frac{N_c}{l_c}$, such that a short pick-up coil is needed. A short pick-up coil means that either the pick-up coil will be shorter than the sample or a short sample is to be used. In the first case, pulses may be generated by magnetisation changes in the parts of the sample where the coil is not placed. In the second case, the sample will have a large N_d. Both are to be avoided. Alternatively, an option is to use a high inductance pick-up coil, such that $\tau_c >> \tau_\Phi$. In this case, $S_{max} \propto \Delta\Phi_c$, but no information is gained on τ_Φ.

For interpretation of the MBE data, it would be ideal if $\Delta\Phi_c \propto \Delta\mathbf{M}$. However, the relation between $\Delta\Phi_c$ and $\Delta\mathbf{M}$ is more complex and depends on several factors, of which the most important are:

- Coil geometry. If the same coil is used and the sample shape is taken constant, this should not disable a good interpretation.
- Sample N_d. The effect of N_d is unclear, but it seems best to have a small N_d.
- Sample χ. As χ varies during the magnetisation process, this might cause misinterpretation. Also, χ is not well defined on the level of magnetic domains, where MBE pulses arise from. The effect of χ is a combined effect with N_d, such that a small N_d lowers the effect of χ.
- Distance from location of magnetisation change to pick-up coil. Due to eddy currents, sudden changes in the material are screened from the surface. However, this is not a hard cut-off, which means that $\frac{\Delta\Phi_c}{\Delta M}$ decreases for changes that are further away from the surface. In case of a pick-up coil that is shorter than the sample length, the same effect accounts for magnetisation changes in the material that is not covered by the pick-up coil. Puppin *et al.* [42] have investigated this effect by using two pick-up coils with varying distance.

Apart from designing new and improved MBE equipment for a scientific approach, the MBE equipment used in this study can very well be used

as a non-destructive evaluation technique. By using various analysis techniques, the effects of different microstructure elements can be distinguished. MBE experiments need to be conducted on samples with known different microstructures to reveal these effects. A systematic approach is recommended, in which only one microstructure parameter is changed at a time. A good start would be to evaluate the observed indication that grain boundaries and dislocations affect various parts of the MBE burst differently.

9.3 Magneto-optical Kerr effect

The magnetic experimental techniques discussed in this study make use of induction of electric currents in coils due to changing magnetic fields. This method calls back on the basic understanding of magnetic fields as way of interaction between electric currents. However, not only electric currents are affected by magnetic fields. Electromagnetic radiation is affected by magnetism as well.

When light is reflected on a surface with a net magnetic moment, the polarity of the reflected light and the reflectivity depend on the angle between the light beam and magnetic moment and the magnitude of the magnetic moment. This effect is known as the magneto-optical Kerr effect (MOKE). A changing magnetisation will thus lead to changes in the polarisation and intensity of reflected light.

Puppin *et al.* [43, 44] have developed this MOKE into a magnetisation sensor. The used light is a polarised laser beam that can be focussed on the sample surface. Polarising and focussing of the laser beam is a matter of regular optics, which principally allow a large variation in spot sizes. This potential variation in spot size makes MOKE a technique with good potential. Unlike MBE, the MOKE sensor only records the magnetisation and magnetisation changes at the surface covered with the laser beam spot. A large spot size, in the order of $1 - 3$ mm will give the average magnetisation of the surface of the whole sample. A small spot size, in the order of $10 - 30$ μm will give the magnetisation of one or a few domains. It remains questionable if MOKE has the same potential as MBE or magnetisation curve experiments for microstructure evaluation, but it seems a useful addition in providing understanding about the magnetisation process.

9.4 Magnetic force microscope

In this study, an impression of the domain structure is obtained using a magnetic force microscope (MFM). More extensive use of an MFM can improve understanding on the domain wall pinning phenomenon. An MFM is not suitable for observing processes that occur during domain wall motion, since the time required to obtain an MFM image is much larger than the time scale of domain wall motion. However, detailed MFM images can reveal the most important pinning points and possibly domain wall characteristics.

In the MFM used, no magnetic field was applied. However, at the University of Twente, an MFM is developed that can be placed between two electromagnets. In this way, the domain structure can be viewed at different parts of the magnetisation process. This equipment can reveal which processes are active in the various parts of the magnetisation curve. In this way, it can be determined better which process mainly determines the remanence.

On the other hand, it can be determined which parts of the microstructure are most favourable for domain nucleation. It can also be determined which parts of the microstructure serve as main pinning points when the magnetic microstructure is settled in a certain state. It has been shown that dislocations interact with domain wall motion. It would be interesting to see if this interaction can be determined from the domain structure at different magnetic states.

Bibliography

[1] Cullity, B. *Introduction to magnetic materials.* Addison-Wesley, (1972).

[2] Jiles, D. *Introduction to magnetism and magnetic materials.* Chapman & Hall, (1991).

[3] Buttle, D. J., Scruby, C. B., Jakubovics, J. P., and Briggs, G. A. D. *Philosophical Magazine A-Physics Of Condensed Matter Structure Defects And Mechanical Properties* **55**(6), 717–734 June (1987).

[4] Kobayashi, M. and Ishikawa, Y. *Ieee Transactions On Magnetics* **28**(3), 1810–1814 May (1992).

[5] Kittel, C. *Reviews Of Modern Physics* **21**(4), 541–583 (1949).

[6] Träuble, H. *Zeitschrift Fur Metallkunde* **53**(4), 211–231 (1962).

[7] Barkhausen, H. *Physikalische Zeitschrift* **20**, 401 (1919).

[8] Jiles, D. C. *Acta Materialia* **51**(19), 5907–5939 November (2003).

[9] Buttle, D. J., Jakubovics, J. P., Briggs, G. A. D., and Scruby, C. B. *Philosophical Magazine A-Physics Of Condensed Matter Structure Defects And Mechanical Properties* **55**(6), 735–756 June (1987).

[10] Staudhammer, K. P., Murr, L. E., and Hecker, S. S. *Acta Metallurgica* **31**(2), 267–274 (1983).

[11] Vaidyanathan, S., Moorthy, V., Jayakumar, T., and Raj, B. *Materials Science And Technology* **16**(2), 202–208 February (2000).

[12] Hull, D. and Bacon, D. *Introduction to dislocations.* Butterworth-Heinemann, (2001).

[13] Smith, A. *Recovery and recrystallisation in C-Mn steels following hot deformation.* PhD thesis, Delft University of Technology, (2006).

[14] Verdier, M., Brechet, Y., and Guyot, P. *Acta Materialia* **47**(1), 127–134 December (1998).

[15] Bodin, A. *Intercritical deformation of low-alloy steels.* PhD thesis, Delft University of Technology, (2002).

[16] Frost, J. and Ashby, M. *Deformation-mechanism maps.* Pergamon, (1982).

[17] Nes, E. *Progress In Materials Science* **41**(3), 129–193 (1997).

[18] Träuble, H. *Magnetism and metallurgy 2*, 622. Academic Press (1969).

[19] Martinez-de Guerenu, A., Arizti, F., Diaz-Fuentes, M., and Gutierrez, I. *Acta Materialia* **52**(12), 3657–3664 July (2004).

[20] O'Sullivan, D., Cotterell, M., Tanner, D. A., and Meszaros, I. *Ndt & E International* **37**(6), 489–496 September (2004).

[21] Martinez-de Guerenu, A., Arizti, F., and Gutierrez, I. *Recrystallization And Grain Growth, Pts 1 And 2* **467-470**, 141–146 (2004).

[22] Stupakov, O. and Tomas, I. *Ndt & E International* **39**(7), 554–561 October (2006).

[23] Iordache, V. E., Hug, E., and Buiron, N. *Materials Science And Engineering A-Structural Materials Properties Microstructure And Processing* **359**(1-2), 62–74 October (2003).

[24] Sagar, S. P., Parida, N., Das, S., Dobmann, G., and Bhattacharya, D. K. *International Journal Of Fatigue* **27**(3), 317–322 March (2005).

[25] Pal'a, J., Stupakov, O., Bydzovsky, J., Tomas, I., and Novak, V. *Journal Of Magnetism And Magnetic Materials* **310**(1), 57–62 March (2007).

[26] Hug-Almaric, A., Kleber, X., Merlin, J., Petitgrand, H., and Meilland, P. *Materials Science Forum* **539-543**, 4283–4288 (2007).

[27] Kleber, X. and Vincent, A. *Ndt & E International* **37**(6), 439–445 September (2004).

[28] Dhar, A., Clapham, L., and Atherton, D. L. *Ndt & E International* **34**(8), 507–514 December (2001).

[29] *Stresstech MicroScan 600 Operating Instructions V.4.3.*

[30] Bailey, J. E. and Hirsch, P. B. *Philosophical Magazine* **5**(53), 485–& (1960).

[31] Nakashima, K., Suzuki, M., Futamura, Y., Tsuchiyama, T., and Takaki, S. *Nanomaterials By Severe Plastic Deformation* **503-504**, 627–632 (2006).

[32] Kim, H. S. *Materials Science and Engineering A* **289**(1-2), 30–33 September (2000).

[33] Mikami, Y., Mochizuki, M., Nakamura, T., Hiraoka, K., and Toyoda, M. *Advanced Structural And Functional Materials Design, Proceedings* **512**, 379–382 (2006).

[34] Toyoda, M., Mochizuki, M., and Mikami, Y. *Advanced Structural And Functional Materials Design, Proceedings* **512**, 19–24 (2006).

[35] Bhadeshia, H. In *Proceedings of the 6th International Conference on Trends in Welding Research*, (2002).

[36] Goodenough, J. B. *Physical Review* **95**(4), 917–932 (1954).

[37] Raj, B., Moorthy, V., Jayakumar, T., and Rao, K. B. S. *International Materials Reviews* **48**(5), 273–325 October (2003).

[38] Sablik, M. J. *Journal Of Applied Physics* **89**(10), 5610–5613 May (2001).

[39] Mikheev, M. N. and Gorkunov, E. S. *Soviet Journal Of Nondestructive Testing-Ussr* **17**(8), 579–592 (1981).

[40] Degauque, J., Astie, B., Porteseil, J. L., and Vergne, R. *Journal Of Magnetism And Magnetic Materials* **26**(1-3), 261–263 (1982).

[41] McClure, J. C. and Schroder, K. *Critical Reviews in Solid State and Materials Sciences* **6**(1), 45–83 (1976).

[42] Puppin, E., Zani, M., Vallaro, D., and Venturi, A. *Review of Scientific Instruments* **72**(4), 2058–2061 (2001).

[43] Puppin, E., Vavassori, P., and Callegaro, L. *Review of Scientific Instruments* **71**(4), 1752–1755 (2000).

[44] Pinotti, E., Zani, M., and Puppin, E. *Review of Scientific Instruments* **76**(11), 113906 (2005).

List of symbols

a	Lattice parameter	m
A	Area	m^2
b	Burgers vector	m
$\mathbf{B}$	Magnetic induction	Tesla (T) = kg s^2 A^{-1}
$\mathbf{B}_r$	Remanent induction	T
C	Constant	various
d	Diameter	m
d_g	Grain size	m
E	Young's modulus	Pa = N m^{-2} = kg m^{-1} s^{-2}
f	Volume fraction	-
$\mathbf{f}_j$	Interaction force lattice defect on domain wall	Newton (N) = kg m s^{-2}
f_M	Magnetising frequency	Hertz (Hz) = s^{-1}
f_s	Sampling frequency	s^{-1}
$\mathbf{F}$	Force	N
F_T	Taylor factor	-
G	Shear modulus	Pa
$\mathbf{H}$	Magnetic field strength	A m^{-1}
$\mathbf{H}_a$	Applied magnetic field	A m^{-1}
$\mathbf{H}_c$	Coercivity	A m^{-1}
$\mathbf{H}_d$	Demagnetising field	A m^{-1}
H_V	Hardness Vickers	HV
$\mathbf{i}$	Direction of magnetic field	-
$\mathbf{I}$	Intensity of magnetisation	T
k_B	Boltzmann's constant	$1.38x10^{-23}$ m^2 kg s^{-2} K^{-1}
K_i	Anisotropy constant	J m^{-3}
l_a	Activation length	m
l_c	Length of pick-up coil	m
L	Inductance of pick-up coil	Henry (H) = kg m^2 s^{-2} A^{-2}
m_j	number of defects of type j	-
$\mathbf{m}$	Atom magnetic moment	A m^2
M	Mean value	-
$\mathbf{M}$	Magnetisation	A m^{-1}
$\mathbf{M}_r$	Remanent magnetisation	A m^{-1}

$\mathbf{M}_s$	Saturation magnetisation	A m^{-1}
$\mathbf{M}_z$	Z-component of magnetisation	A m^{-1}
N	Number of MBE pulses	-
N_c	Number of turns in pick-up coil	-
N_d	Demagnetisation factor	-
Q_0	Activation energy	J mol^{-1}
Q_A	Energy per unit of area	J m^{-2}
Q_{An}	Anisotropy energy	J m^{-3}
Q_{Co}	Coupling energy	J
Q_{DW}	Domain wall energy	J m^{-2}
Q_{mag}	Magnetic energy	Joule (J) = kg m^2 s^{-2}
Q_V	Energy per unit of volume	J m^{-3}
r	Radius of curvature	m
s	Domain wall displacement	m
S	Barkhausen jump size	Wb s^{-1} = V = kg m^2 s^{-3} A^{-1}
t	Time	s
T	Temperature	K
T_C	Curie temperature	K
$\mathbf{v}_{DW}$	Domain wall velocity	m s^{-1}
V	Volume	m^3
V_a	Activation volume	m^3
W_{hys}	Hysteresis loss	J
z	Location of lattice defect	m
z_0	Location of domain wall centre	m
α	Angle (magnetic moment and crystal axis)	-
γ	Contribution to coercivity	various
γ_D	Contribution due to dislocations	A
δ	Domain wall thickness	m
δ_f	Range of $\mathbf{f}_j$	m
ϵ	Strain	-
ζ	Contribution to RMS value	V^2
θ	Angle (magnetisation and applied field)	-
μ	Permeability	(H m^{-1})
μ_0	Permeability of vacuum	$4\pi x10^{-7}$ H m^{-1}
μ_{in}	Initial permeability	H m^{-1}
μ_{max}	Maximum permeability	H m^{-1}
μ_r	Relative permeability	-
ν	Number of statistically independent events	-
ν_D	Debye frequency	s^{-1}

ξ	Magnetic coupling parameter	m^{-3}
ρ_D	Dislocation density	m^{-2}
ρ_j	Density of defects of type j	m^{-3}
σd	Standard deviation	-
$\boldsymbol{\sigma}$	Stress	Pascal (Pa) = kg s^{-2} m^{-1}
σ_D	Stress due to dislocations (abs value)	Pa
σ_{def}	Stress at end point of deformation	Pa
τ_c	Time constant of pick-up coil	s
τ_Φ	Time constant of flux change	s
ϕ	Angle between magnetisations of domains	-
$\boldsymbol{\Phi}$	Magnetic flux	Weber (Wb) = kg m^2 s^{-2} A^-
$\boldsymbol{\Phi}_c$	Flux at pick-up coil	Wb
χ	Susceptibility	-
χ_{max}	Maximum susceptibility	-